HIGH-ENERGY, HIGH-DOSE O IMPLANTATION IN Si

By

Susan Leigh Ellingboe

A Thesis Submitted for the Degree of

DOCTOR OF PHILOSOPHY

of the

AUSTRALIAN NATIONAL UNIVERSITY
Research School of Physical Sciences and Engineering

December 1995

I certify that this thesis does not incorporate without acknowledgment, any material previously submitted for a degree or diploma in any university; and that to the best of my knowledge and belief it does not contain any material previously published or written by another person except where due reference is made in text.

Susan Ellingbve

ACKNOWLEDGMENTS

I would like to extend my sincere thanks to my supervisor, Dr. Mark Ridgway for providing a role model of the kind of scientist I want to be. He was a continual source of support and guidance throughout my PhD. work. Appreciation is also given to my co-advisors, Dr. Jim Williams and Dr. Robert Elliman, and to Dr. C. Jagadish for providing an atmosphere conducive to doing "good" science and for teaching me good scientific practices.

The Australian Defence Force Academy is gratefully acknowledged for the use of their TEM. All of the TEM work in Chapter 3 was performed on their equipment. Dr. Van Watenaar and John Malunec are thanked for sharing their knowledge of electron microscopy as well as providing technical support. The TEM work in Chapters 4 and 5 was performed at the Electron Microscopy Unit in the Research School of Biological Sciences at the ANU. David Llewelyn, Alan Lee and Dr. Sally Stowe are acknowledged for technical support. For help in TEM micrograph interpretation, I extend my thanks to Dr. John Fitz Gerald. Dr. Peter Schultz and Dr. P. Simpson of the University of Western Ontario are acknowledged for providing VEP measurements on SIMOX samples.

Bernie King, Tom Halstead, Marco Maldoni, Tony Watt and Alan Hayes provided technical support and guidance that is much appreciated. They are all thanked for inadvertently giving me lessons on the Australian male.

Thanks for proof reading go to Dr. Renate Egan, John Glasko, and Dr. Mark Ridgway. The small favours by John Glasko after the author left Australia are especially appreciated. Andrew Clark deserves a special acknowledgment for being a best friend at and outside of work. Jennifer Wong-Leung, Dr. Renate Egan and Franca Placidi provided a support network of female colleagues and are thanked for many enjoyable conversations. My fellow students at EME made my work more enjoyable and were constant sources of information and help. They include W.C. Wong, Kidane Belay, Andrew Clark, Jennifer Wong-Leung, Hoe Tan, John Glasko and Paul Gortmaker.

Special thanks to Mark Jarnyk and Judy Kay for having more faith in me than I had in myself at times. Thanks to my family (mom, dad, Kathy and Megan) for their continual support. For inspiring me to be all that I can be I thank my grandfather, Sylvester Thomas.

Finally, I thank my husband for inspiring me to keep plugging away through the difficult times. This much.

High-energy, High-dose O Implantation in Si

ABSTRACT

The formation of Separation by Implantation of Oxygen (SIMOX) material by MeV O-ion implantation was investigated at doses between 0.3-2.18x10^{18} O/cm^2. It was demonstrated that implant temperatures as low as 150°C can be used for SIMOX fabrication without total amorphisation of the Si overlayer. The microstructure of the material after annealing was found to be highly implant-temperature dependent, with lower implant temperatures (~150°C) suppressing SiO_2 and Si precipitate formation within the Si overlayer and buried SiO_2 layer, respectively. MeV self-ion implantation in Si was performed to elucidate the contribution of a high O impurity concentration to damage formation in high-dose O-implanted Si. It was shown that a high O concentration contributes to amorphous layer formation at the ion end-of-range. Conversely, a comparison of O and Si implantation at doses which produced a similar athermal vacancy concentration at depths less than the ion end-of-range indicated that damage within the Si overlayer was independent of the implanted specie.

Tensile strain at depths less than the ion end-of-range in high-dose Si- and O-implantation was shown to be the result of an implantation-induced vacancy excess. The magnitude of the strain was related to implanted ion dose, implant temperature, and post-implantation annealing time. It was shown that when the strain maximum exceeds the yield strain of Si, dislocation formation results at the depth of the strain maximum. MeV O implantation was utilised to characterise, for the first time, the yield strength of Si between 150 and 450°C.

A reduction or increase in strain in O-implanted Si through a secondary Si-ion implant was demonstrated. Depending on the energy and therefore range of the secondary Si implant, the vacancy excess resulting from the O implant can be either (1) compensated by interstitials generated by the Si implant and/or implanted-Si ions or (2) increased by additional excess vacancies resulting from the secondary Si implant. Finally, the microstructure in strain-relaxed, high-dose O-implanted Si can be altered by a secondary Si implant. Improvements in the crystallinity at the front Si/SiO_2 interface are observed in O-implanted Si after subsequent high-energy Si irradiation and post-implantation annealing. These microstructural changes were shown to be the result of Ion Beam Annealing.

This is dedicated to my favourite plasma physicist, Bert Ellingboe

Table of Contents

Chapter 1

Introduction to the Silicon-on-Insulator Process and Technology

1.0 Introduction

Semiconducting crystalline films on an insulating substrate are attractive for device fabrication (for reasons detailed below) and as a consequence there is extensive interest in the development of a silicon-on-insulator (SOI) technology. A typical device fabricated on an SOI substrate is pictured in Figure 1.1. The complete dielectric isolation of individual devices is readily apparent. Since the p-n junction area is reduced, the junction capacitance is decreased and faster device operating speeds are possible. Higher operating voltages and increased packing densities of such devices are also achievable. The smaller active Si volume reduces thermally- and radiation-generated currents resulting in increased radiation hardness and higher permissible operating temperatures. All of these advantages mean SOI technology has found application in military and space electronics and in the automotive, aircraft and computer industries. The major disadvantage of SOI-based devices is the higher substrate cost. However, the cost is becoming increasingly competitive as the demand for SOI substrates rises.

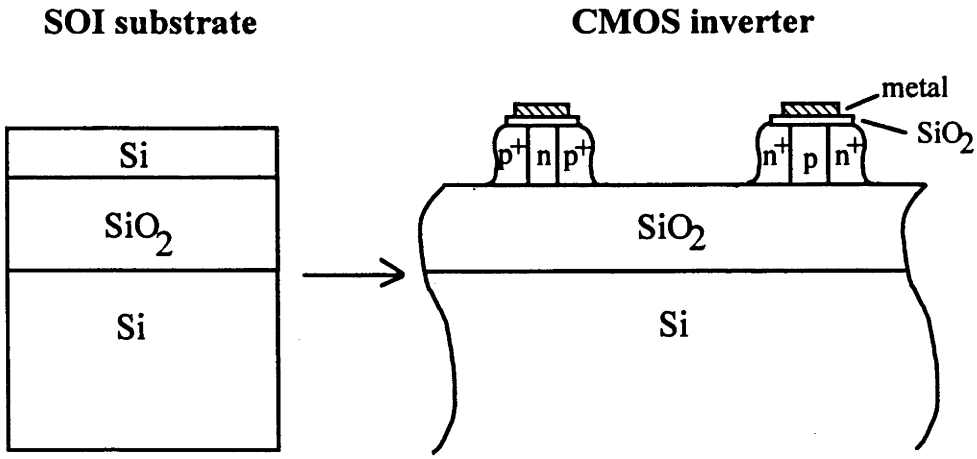

Figure 1.1: Schematic of a typical device (CMOS inverter) fabricated on an SOI substrate.[1]

There are several methods of SOI substrate fabrication. A brief introduction to several of these technologies follows in section 1.1. Section 1.2 describes in more detail the method used for SOI substrate fabrication in this work, Separation by IMplantation of OXygen (SIMOX). At present, this is the leading and most commercially advanced technique. Finally, section 1.3 reviews the various processing methods used to improve SIMOX material quality.

1.1 Methods of Forming Si-on-Insulator Materials

1.1.1 Epitaxial growth of Si on an insulator

1.1.1a Heteroepitaxial techniques

The application of heteroepitaxy to the fabrication of SOI material involves the growth of a Si film on a single crystal insulator. Substrates can be either bulk single crystal material, such as sapphire (Al_2O_3) or spinel, or thin insulating films grown on a

Si substrate. Some examples of the latter include CaF_2 and cubic zirconia. The choice of the insulator is governed by differences in lattice constant and thermal expansion coefficient (α) relative to Si. The Si epitaxial growth is typically performed at ~1000°C and, upon cooling, differences in α can increase lattice mismatch yielding strain and/or defect generation in the Si film. Unfortunately, $\alpha_{insulator}$ is typically 2-3 times greater than α_{Si}. Thus, thermal mismatch is generally the most important factor determining the physical and electrical properties of heteroepitaxial Si films grown on insulators.

Si-on-sapphire (SOS) is the most common heteroepitaxial SOI materials system and the only one to reach production. (Wafers have been commercially available since 1971.) To produce SOS substrates, a Si film is deposited using the pyrolysis of silane at temperatures between 900-1000°C. The difference in thermal expansion coefficients ($\alpha_{Al_2O_3} \approx 2.5\alpha_{Si}$) results in high defect concentrations. Typical defect densities are 10^6 planar defects/cm^2 and 10^9 line defects/cm^2.[2] Although devices are fabricated on SOS material at present, this technology has several disadvantages. These not only include large defect densities but high production costs, mechanical fragility and the need for a dedicated Al_2O_3 processing line. For a comprehensive review of SOS technology, see Gupta, et al.[3,4]

1.1.1b Homoepitaxial techniques

A method similar to SOS technology involves the growth of epitaxial Si on a Si substrate coated with an insulating layer. Openings in the insulator (usually SiO_2) provide a seed for single-crystal epitaxial Si growth. There are two different methods of homoepitaxial growth. For Epitaxial Lateral Overgrowth (ELO), epitaxial Si is seeded through openings in the insulator extending to the crystalline substrate. From these openings, the deposited Si grows laterally over the SiO_2 surface as shown schematically in Figure 1.2. As with heteroepitaxy, Si growth is performed using silane, H_2 and HCl gases at ~1050-1200°C. By varying the HCl gas concentration and/or the growth temperature, and by using a series of growth/etch steps and different substrate orientations, the growth procedure has been optimised, eliminating the nucleation of polycrystalline Si (polySi). As a result low defect density (10^2-10^3 cm^{-2}) single-crystal Si films have been produced.[2] The substrate orientation is retained laterally for ~100 μm, so seeding windows separated by $\leq$ 200 μm are necessary. The major limitation of this technique is that to completely fill the seeding windows and obtain a sufficiently planar surface, thick Si films are necessary. Hence, thin ($\leq$ 5 μm) Si films of good crystalline quality are virtually impossible to produce using this technique.

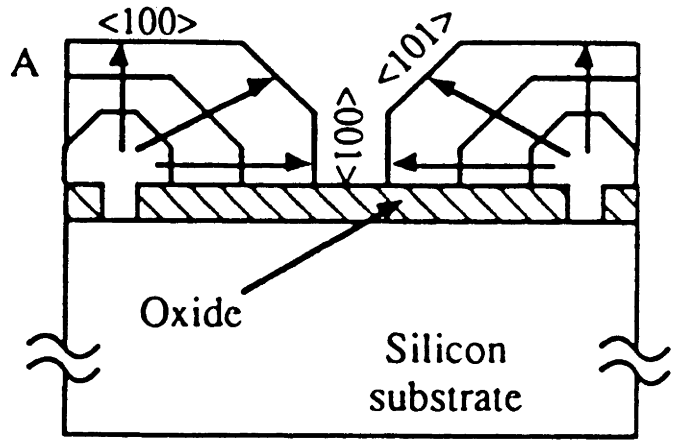

Figure 1.2: Schematic of Epitaxial Lateral Overgrowth (ELO) using a seeding window.[2]

A second technique is Lateral Solid Phase Epitaxy (LSPE) where lateral epitaxial growth of crystalline Si (c-Si) is accomplished through the controlled crystallisation of amorphous Si (a-Si). Amorphous Si is either deposited directly or polySi is amorphised using Si self-implantation. Seeding windows are again used to provide the template necessary for single-crystal growth. To suppress random nucleation in the a-Si, low recrystallisation temperatures (~600°C) are necessary. The major advantage of this technique is low-temperature processing. Disadvantages include residual defects in regions where two recrystallisation fronts intersect.

1.1.2 Full Isolation by Porous Oxidised Si (FIPOS)

This technique, which dates back to 1981[5], entails the production and subsequent oxidation of porous Si. Selective conversion of c-Si to porous Si can be accomplished using a variety of techniques that preferentially convert either p- or n^+- Si to porous material. Si_3N_4 is patterned onto the Si wafer and then implantation is used to form, for example, n^- regions under the mask and p^+ regions in the unmasked area as shown in Figure 1.3. Thereafter, the p-type Si is preferentially converted to porous Si via anodic

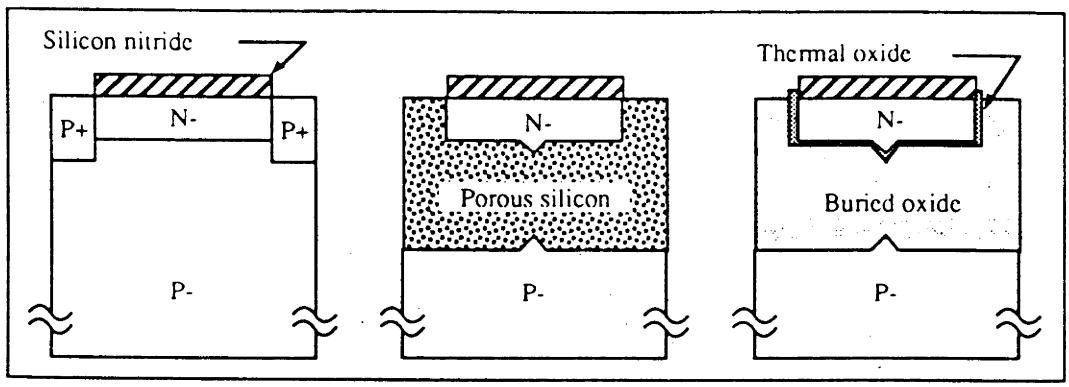

Figure 1.3: The FIPOS process, from left to right: formation of n^- islands and p^+ current paths, formation of porous Si and oxidation of the porous Si.[5]

oxidation since the oxidation rate of porous Si is orders of magnitude higher than c-Si. Upon oxidation, a thick buried oxide is formed while only a thin thermal oxide grows at the edges of the n^--Si islands. The thermal oxide provides an interface of good structural and electrical quality between the Si and buried SiO_2.

Thin film applications are limited by non-uniformities introduced by the cusp where the anodisation fronts meet below the Si islands. As well, the requirement of a masking step to form Si islands hinders the commercialisation of the FIPOS process.

1.1.3 Recrystallisation techniques

The melting and subsequent recrystallisation of a Si film vertically bounded by two insulating layers is another method of producing SOI material. The top insulator is an encapsulating layer which prevents Si delamination (due to surface tension) from the

underlying SiO_2. The recrystallisation of a Si film on an insulator can be accomplished by irradiation with a laser and/or electron beam.

With the former, a continuous-wave Ar^+ laser is typically utilised given the extent of absorption in Si at this wavelength. The beam is generally raster scanned over the entire wafer to induce local melting of the Si. The scanned laser beam is ~50-150 μm in diameter and scan times are the order of seconds. Recrystallisation of the quenched Si proceeds along the thermal gradient produced by the laser. The beam shape (Gaussian) leads to undesirable thermal gradients along the recrystallisation path and small random crystallites due to thermal variations over the extent of the irradiated area can result. These variations, which lead to thermal stress across the wafer during recrystallisation, are minimised by substrate preheating (~300-600°C). The recrystallisation proceeds laterally, beginning at a seeding window as shown in Figure 1.4. Upon melting, the reflectivity of Si abruptly increases reducing the risk of overheating. The use of an encapsulating layer (usually Si oxynitride) not only prevents delamination but is essential to minimise surface non-planarity. However, the production of thin Si films is difficult since a surface roughness of >200 Å is unavoidable.[6]

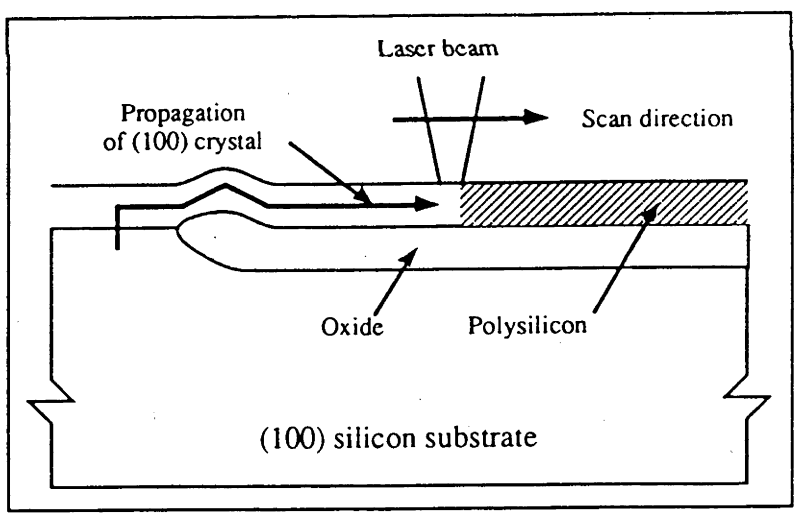

Figure 1.4: Laser Recrystallisation using the lateral seeding process.[2]

Recrystallisation of polySi films using an electron beam (e-beam) is similar to recrystallisation using a laser beam. Common seeding techniques are utilised and an encapsulation layer is again necessary to prevent delamination of the molten Si.[7] However, e-beams have the advantage that they can be scanned using electrostatic deflection which is far more flexible than scanning techniques used with laser beams.

1.1.4 Zone-Melt Recrystallisation (ZMR)

One of the disadvantages of laser and e-beam recrystallisation is the small molten zone produced by the beam that results in long processing times. Incoherent light is an alternative heat source which is used for ZMR. As schematically shown in Figure 1.5, a graphite strip or line-focused lamp can be passed over a Si wafer creating a molten zone along the length of the wafer.[8] As a result, recrystallisation of an entire wafer can be accomplished in a single scan. The Si wafer (usually capped successively with SiO_2/polySi/Si oxynitride, the latter at the surface) is situated on a graphite susceptor. The susceptor is heated to within ~200°C of the Si melting temperature during the zone melting process and additional heating of the Si is produced locally at the surface of the wafer. Consequently, the thermal gradient across the wafer is much smaller than for the laser or e-beam technique. As with the aforementioned techniques, ZMR results in a recrystallised-Si surface non-planarity of ~200 Å.

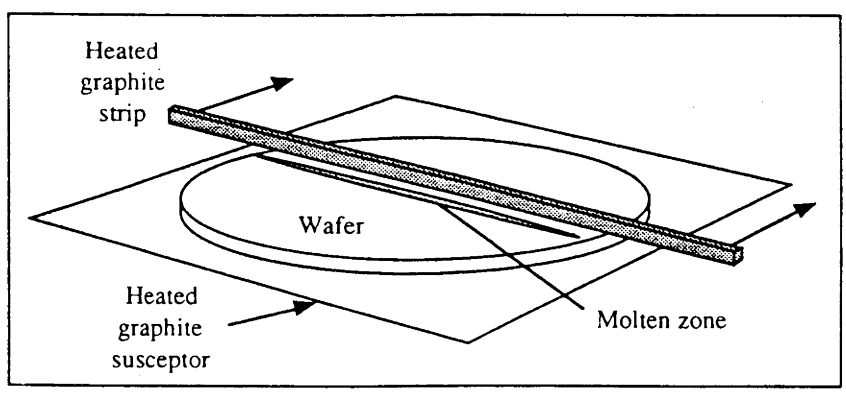

Figure 1.5: Zone-melt recrystallisation of an SOI wafer using a graphite strip heater.

1.1.5 Wafer Bonding and Etch back

Theoretically, wafer bonding should yield a superior Si overlayer (i.e. a lower defect density) in comparison with the techniques previously described. As a consequence, there is great interest in this technique and wafers have recently become commercially available. There are four basic steps in this process as depicted in Figure 1.6. First, an etch stop (formed by implantation or epitaxy) or a polish stop (consisting of an embedded layer of slow polishing materials such as SiO_2) is produced. Then, two oxidised wafers - the device wafer (seed) and the handle wafer (handle) - are bonded together by placing the two hydrophilic SiO_2 surfaces against one another. Once initiated, the bonding process can spread in the form of a contacting wave with the speed of several cm/sec.[9] Contacting forces are believed to be caused by the attraction of hydroxyl groups (OH^-) adsorbed on the two surfaces. The bond between the two wafers is then strengthened by annealing at temperatures $\geq$800°C. Finally, the device wafer is thinned to the required overlayer thickness by one of two methods.

Precision lapping and polishing of the device wafer results in a uniformity of the Si overlayer, at best, of $\pm$ 0.3 μm and thus is more appropriate for SOI applications which require a thick Si overlayer. The preferred thinning method utilises coarse grinding followed by etch-back to the etch stop. For a more detailed description see Maszara[10] or Maszara, et al.[11] Dislocation densities within the Si overlayer of $< 10^3$ cm^{-2} are typical in SOI material fabricated using the bond and etch-back technique.[10] However, the major limitation to this technique is its lack of precise control over the thickness of the Si overlayer.

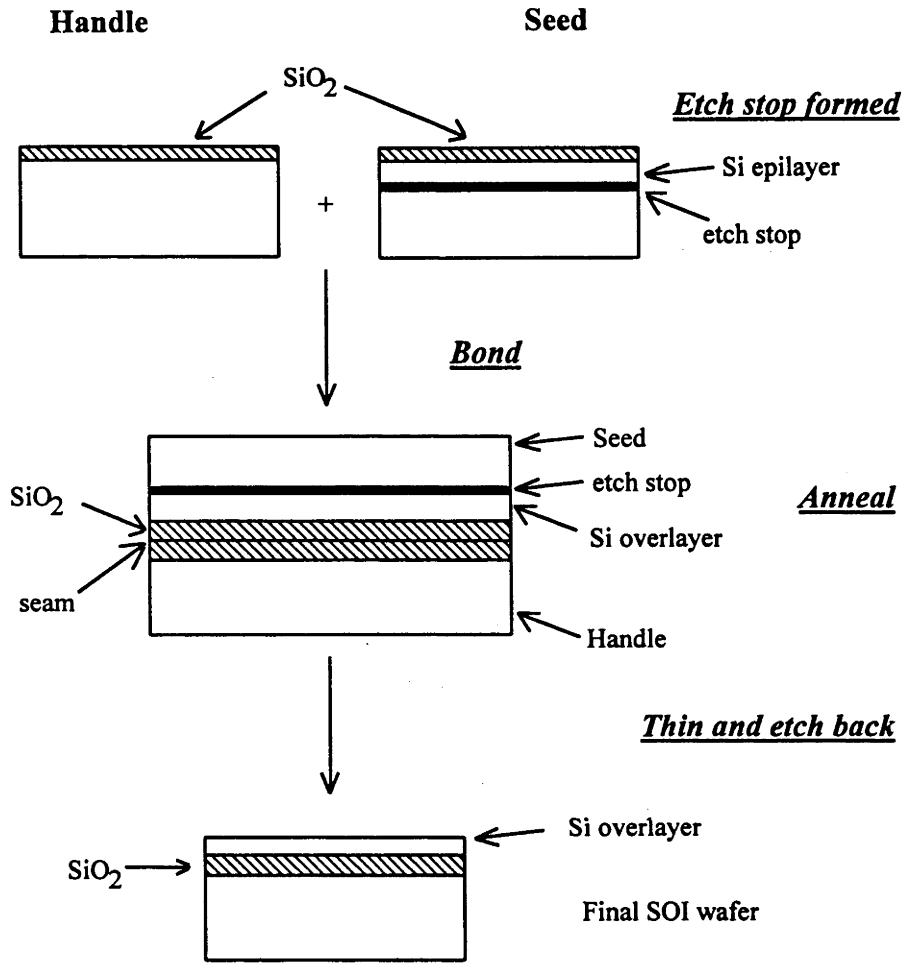

Figure 1.6: Schematic illustration of the wafer bonding and etch-back process.[12]

1.2 SIMOX to form SOI Material

Although each of the previously discussed techniques of producing SOI material has certain advantages, SIMOX fabrication is the leading technology at present as a result of the inherent control of the Si overlayer thickness and compatibility with existing Si manufacturing processes. The electrical and mechanical properties of the Si overlayer are inferior to bulk Si, but satisfy the majority of microelectronic quality specifications. SIMOX substrates are commonly available up to 8" diameter with dislocation densities of $< 10^5$ cm^{-2}. The following sections give a brief history of SIMOX fabrication and discuss the parameters which determine the quality of SOI material fabricated with this technique.

1.2.1 History of SIMOX Material Fabrication

In 1963, the first paper on SiO_2 formation by O implantation in Si was published by Watanabe and Tooi[13] and in 1978, Izumi et al[14] reported the first circuits fabricated on a SIMOX substrate. Four years later, a SIMOX-based 1K static random access memory (SRAM) was fabricated, demonstrating the maturation of SIMOX technology which had previously been considered unviable.[15] 1985 marked the appearance of a high-current implanter which produced an O ion current of 100 mA at an energy of 200 keV, reducing implant times considerably. It was a first and important step towards the commercial viability of the SIMOX technique. That same year, an improvement in the quality of the Si/SiO_2 interfaces was achieved with high-temperature annealing ($> 1300°C$)[16,17] and by 1987, SIMOX wafers (3 to 6") were commercially available. Thereafter, the quality of SIMOX material was further improved by the use of multiple implant and annealing steps,[18,19] which reduced dislocation densities to $< 10^3$ cm^{-2}. Issues such as metallic impurity contamination and cleanliness of the manufacturing environment were also addressed and many types of circuits have since been produced using SIMOX material. For a comprehensive historical review of SIMOX technology, see Colinge.[2]

1.2.2 Dependence of Damage on Oxygen Dose

SIMOX is a high-dose process. While most implantation processes for the microelectronics industry require doses of $\leq 10^{16}\,cm^{-2}$, SIMOX fabrication can necessitate doses of ~$2x10^{18}$ O/cm^2. To form stoichiometric SiO_2 during implantation, two O atoms are required for every Si atom. Thus, to form 4000Å of SiO_2, a dose of

$$(\rho_{SiO_2})(t_{SiO_2})\frac{2\text{ O atoms}}{\text{molecule}} = (2.27x10^{22}\ \frac{\text{molecules}}{cm^3})(4x10^{-5}\text{ cm})(2) = 1.82x10^{18}\ \frac{O}{cm^2}$$

is required (assuming complete encorporation of O into the SiO_2 layer). Figure 1.7 shows the O depth distribution as a function of O dose as simulated using PROFILE code.[20] Below the stoichiometric dose, the profile is approximately Gaussian. When the O concentration reaches 67 atomic %, SiO_2 forms and further implantation of O does not increase the peak O concentration but rather broadens the O profile (i.e. the buried oxide layer increases in width due to the rapid O diffusion in SiO_2).[21]

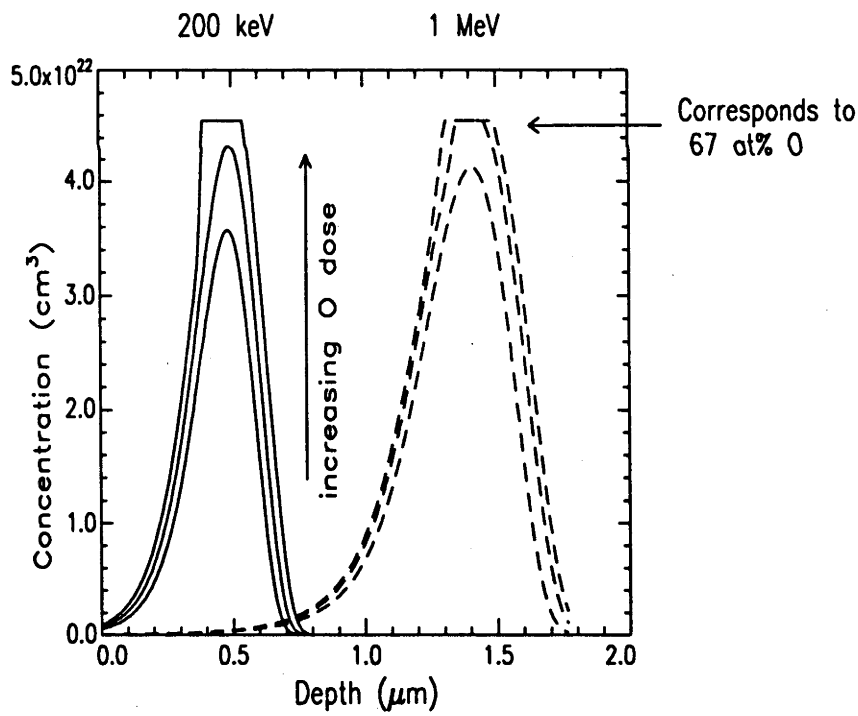

Figure 1.7: O concentration as a function of depth and dose at 200 and 1000 keV implant energies as calculated with PROFILE code.

Figure 1.8 schematically depicts the evolution of damage with increasing dose during implantation.[22] The swelling at the surface occurs because (1) an SiO_2 molecule occupies 2.2 times the volume of a Si atom, (2) the density of amorphous material is less than that of crystalline Si and (3) due to the addition of a high concentration of O atoms. The damage in the Si overlayer results from ion-induced atomic displacements, where at such doses each substrate atom is displaced from a lattice site hundreds or thousands of times. Such displacements (excluding replacement events) result in Frenkel pair generation:

$$Si \Leftrightarrow Si_I + V \qquad (1.1)$$

(where I denotes an interstitial atom and V denotes a vacancy) when the post-collision energy of both atoms exceeds the displacement energy. The athermal depth distribution of implantation-induced disorder typically has a maximum at ~0.8 R_p where R_p is the projected range of the implanted ion.

Since O is in a lower free-energy state in the form of SiO_2 than as an interstitial in a Si lattice (assuming the O concentration is in excess of the solid solubility), SiO_2 precipitates form during implantation. This internal oxidation process is another source of point defects. The reaction yielding SiO_2 precipitation can be written as:[23]

$$2O_I + xSi = SiO_2 + (x\text{-}1)Si_I \qquad (1.2)$$

where x is any number of Si atoms. Oxidation thus results in the emission of Si interstitials and such point defects play a major role in the evolution of the disorder microstructure during both implantation and annealing. The annihilation of Si interstitials and vacancies can result from recombination or annihilation at the sample surface. Furthermore, large excesses of point defects can generate stacking faults, clusters or dislocations. These defects can pin O atoms and SiO_2 precipitates subsequently nucleate.

1.2.3 Dependence of Damage on Implant Temperature

The defect microstructure in as-implanted and annealed SIMOX material is very sensitive to the implant temperature; at a given O dose, the dynamic annealing which occurs during implantation determines the final defect microstructure. Figure 1.9 shows

the effect of implant temperature on the defect depth distribution of 200 keV O-implanted Si. At very low temperatures (<300°C), the entire Si overlayer is amorphised yielding polySi upon annealing. Between 300 and 500°C, crystallinity in the Si overlayer is maintained but amorphisation has occurred near the front Si/SiO_2 interface. Since O impedes solid phase epitaxy,[24] upon annealing the recrystallised Si at such depths is often twinned. In addition, point defects tend to cluster and form dislocation networks which are stable to very high annealing temperatures. At higher implant temperatures (≥500°C), O-rich amorphous platelets embedded in highly damaged Si result near the ion end-of-range. Crystallinity in the Si overlayer is maintained at implant temperatures in excess of 500°C due to dynamic annealing. Higher implant temperatures result in a lower O concentration in the Si overlayer due to a greater redistribution of O atoms towards the peak of the O concentration.[25] At very high implant temperatures (>800°C), SiO_2 precipitates begin to nucleate within the Si overlayer. Due to the extremely low diffusivity of Si in SiO_2 ($\sim 10^{-20}$ cm^2/sec at 1000° C)[26] these SiO_2 precipitates impede the flow of Si interstitials to the Si surface and consequently, the defect concentration increases.

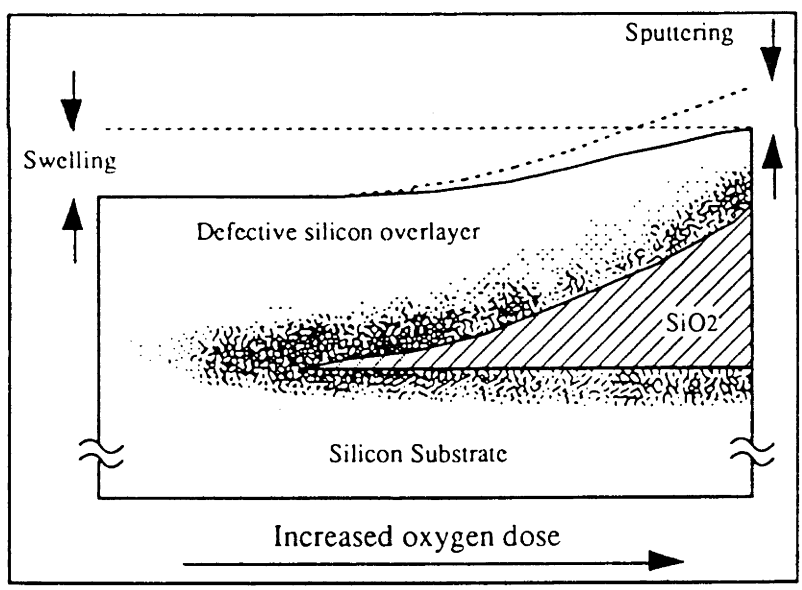

Figure 1.8: Evolution of damage in SIMOX material with increasing O dose.[22]

The implantation temperature also affects the uniformity of the buried oxide. Si trapped within the amorphous zones of SiO_2 results in the formation of Si precipitates within the buried SiO_2 layer upon annealing. At low implant temperatures (150°C), the size of the Si precipitates is decreased.[27] These Si precipitates degrade electrical performance since they provide conductive paths between the Si overlayer and substrate.

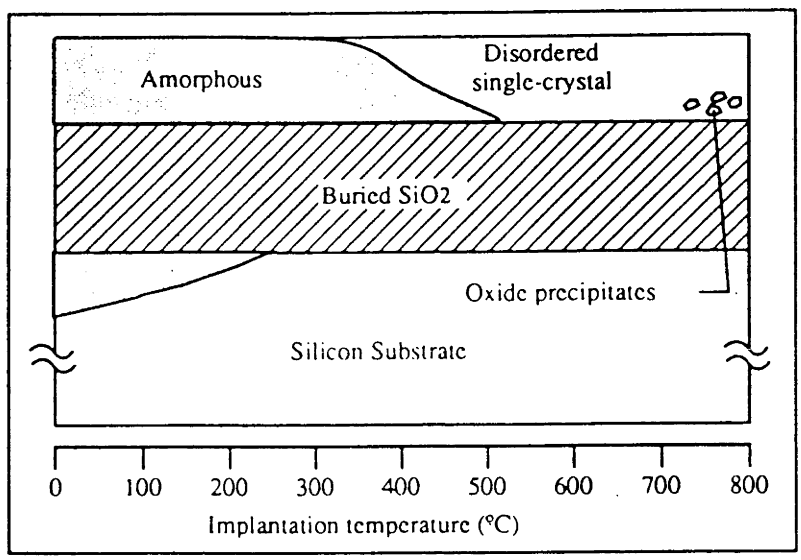

Figure 1.9: Evolution of damage in SIMOX material as a function of implant temperature at a dose of $1.8x10^{18}$ cm^{-2} and an energy of 200 keV.[21]

1.2.4 High-Temperature Annealing

Post-implantation annealing is essential to form low-defect-density, device-grade SIMOX material. Figure 1.10 shows the evolution of the defect microstructure of SIMOX material with increasing anneal temperature and time. High anneal temperatures are required to induce O segregation from depths with an O concentration below 67 atomic % and to dissolve SiO_2 precipitates which have formed at such depths. The growth and dissolution of the precipitates is the result of Ostwald ripening which

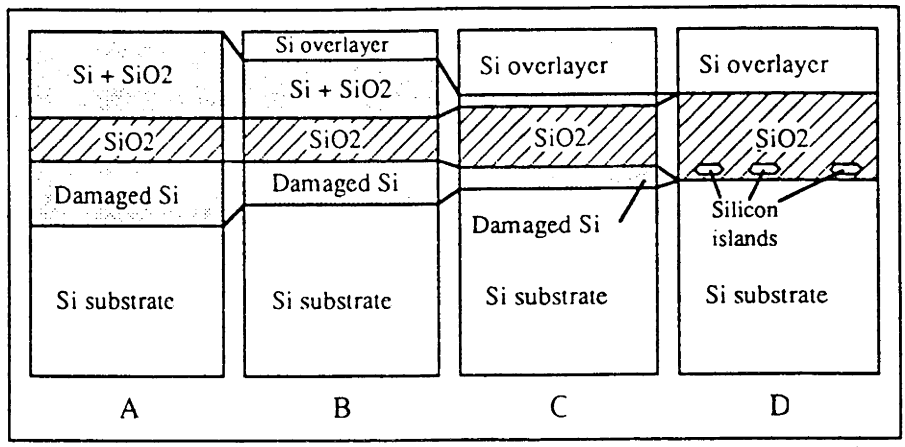

Figure 1.10: Evolution of SIMOX microstructure during high temperature annealing (A) as-implanted (B) 2 hr. at 1150°C (C) 6 hr. at 1185°C (D) 6 hr. at 1300°C.[28]

can be explained by the thermodynamics of the Si-O system.[28] Smaller precipitates are dissolved in favour of larger ones and the entire process is driven by free-energy considerations. A critical precipitate radius (r_c), below which SiO_2 precipitates will dissolve, can be defined as:

$$r_C = \frac{2\sigma}{\Delta H_V}\frac{T_E}{(T_E - T)} \qquad (1.3)$$

where ΔH_v is the enthalpy of formation of the SiO_2 phase per unit volume, σ is the Si/SiO_2 interfacial energy, T is the anneal temperature and T_E is the equilibrium temperature. The equilibrium temperature is the temperature at which the implanted O concentration *would be* in equilibrium with the surrounding lattice. Because ion implantation is a non-equilibrium process, the O concentration is typically in supersaturation with the surrounding lattice and hence, $T_E > T$. The critical radius depends on both T and (T_E-T), the latter of which is an expression of the interstitial O supersaturation. If $r < r_c$, the precipitate is unstable and dissolves. If $r > r_c$, the

precipitate is stable and grows. At high temperatures the critical radius approaches infinity and a buried oxide layer (essentially a precipitate of infinite radius) is the only stable precipitate. While high-temperature annealing is essential to produce device-grade SIMOX material, defects which have formed within the Si overlayer before post-implantation annealing, such as threading dislocations and stacking faults, can not be totally eliminated by such annealing.

1.3 Refinements of the SIMOX Process to form Low-Defect-Density SOI Material

In 1985 Jassaud, et al[29] reported that post-implantation annealing at high temperatures (>1300°C) would rid the Si overlayer of SiO_2 precipitates. This high temperature annealing led to vast improvements in the Si/SiO_2 interface, but still left an unacceptably high density of dislocations (~10^9 cm^{-2}) in the Si overlayer. Consequently, new methods of defect reduction which inhibited defect formation during implantation were sought. Because the exact mechanisms of defect formation are still under investigation, many methods of defect reduction have been explored. Various techniques which reduce the defect density to as low as 10^3 cm^{-2} are discussed below.

1.3.1 Channeled Implants

The importance of point defect generation and annihilation in relation to the secondary defect concentration in SIMOX material has already been highlighted. One source of dislocation generation is the excessive amount of point defects that are created by impinging O ions and recoiled Si atoms. The use of channeled implants to reduce the collision probability and hence, reduce point defect generation in the near-surface region was thus investigated.[30] Not surprisingly, it was shown that the number of point defects created is reduced when the Si substrate is crystographically aligned with the incoming O ions. However, implanters with a high throughput are not designed to perform channeled implants and consequently this technique has limited practical applications.

1.3.2 Si Epitaxial Growth on SIMOX Substrates

An alternative method of fabricating a Si overlayer with a reduced defect density utilises the growth of a Si epitaxial layer on annealed SIMOX material. Figure 1.11 shows the reduction in dislocation density obtained as a function of Si epitaxial layer thickness.[31] Though it is apparent that an order of magnitude reduction in dislocation density was achieved after epitaxial Si growth, this technique adds an extra processing step without significantly reducing the defect density. As well, the additional Si overlayer thickness is not compatible with the requirements for fully-depleted circuits. Still, in the mid-1980s it was a commonly utilised technique.[32,33] Today, Si epitaxial layers are grown on SIMOX wafers when a thicker Si overlayer is required for specific applications such as three-dimensional circuits or high-power applications.[34]

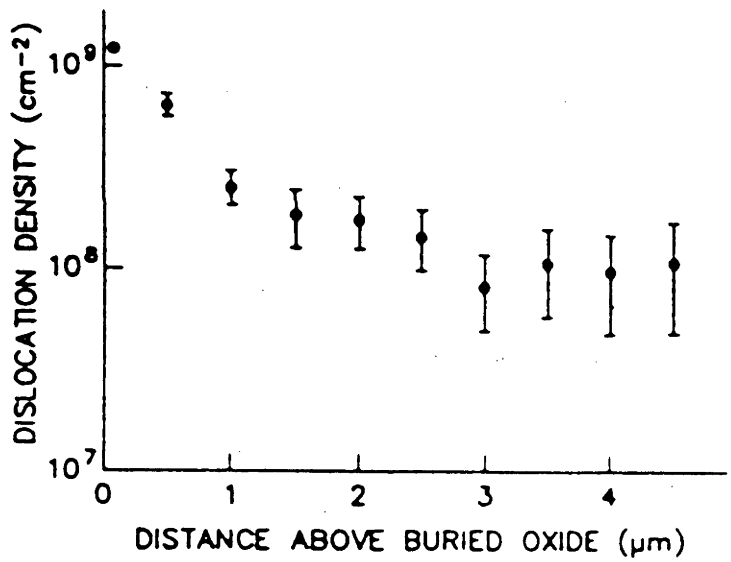

Figure 1.11: Dislocation density depth profile after 4.5 μm of Si epitaxy on a SIMOX substrate.[31]

1.3.3 Cavity Nucleation in the Si Overlayer

Under certain implantation conditions, high densities of cavities (vacancy clusters) within the Si overlayer can result. During subsequent annealing these cavities act as stress-free sinks for O and Si interstitials, limiting the generation of dislocation loops and confining such loops to regions near the buried oxide.[35] These cavities are believed to be stabilised by O which forms a thin SiO_2 layer on the cavity walls and consequently, these cavities are stable up to temperatures of ~1100°C. Annealing above this temperature dissolves the cavities leaving a Si overlayer with a reduced defect density. (A defect density of $<10^4$ cm^{-2} was reported using this method.)[35] Unfortunately, cavities can only be produced with implant temperatures of >600°C and high current densities.[36,37] Such implant conditions result in surface roughness and a poor quality buried oxide.[38] Consequently, this technique is not used in production.

A similar method involving cavity nucleation through a 900°C, 0.5 hour has been reported.[39-41] This technique combines sequential implantation and annealing (section 1.3.4) whereby the total dose (Φ) is reached through incremental implants of ~ $\Phi/3$, for example. By annealing between implants at the low temperature of 900°C (as compared to the final 1300°C anneal), strain within the Si overlayer is relieved and consequently dislocation nucleation occurs at higher total doses than without the intermediate annealing steps.

1.3.4 Multiple Implantation and Annealing

A significant advance in dislocation density reduction was made in 1988 when a threshold for dislocation formation in O-implanted Si was reported.[42] At an implant energy of 150 keV, the critical dose (ϕ_c) for dislocation formation was ~$5x10^{17}$ O/cm^2. (The implant temperature for this work was not reported.) The three possible suggestions for the existence of a threshold dose offered were:[18] (1) the existence of a critical O precipitate size above which dislocation loop formation resulted, (2) damage accumulation with increasing dose and (3) the accumulation of tensile strain with increasing dose.

It was subsequently demonstrated that sequential implants below ϕ_c in combination with high temperature annealing produced a continuous, thick oxide with a dislocation free ($<10^3$ cm^{-2}) Si overlayer.[18] In other words, SIMOX material implanted at an energy and temperature of 150 keV and 475°C, respectively, with three intermediate doses of

$4x10^{17}$ O/cm^2 and an intermediate annealing step at 1250°C for 17 hours had a final dislocation density of ~10^5 cm^{-2}.[19,43] Presently, dislocation densities acceptable for device fabrication (~10^3 cm^{-2}) are routinely achieved in SIMOX material produced using multiple implantation and annealing. The disadvantages of this technique include long anneals at high temperature which can result in wafer contamination and a higher cost per wafer due to the extra processing step(s).

1.3.5 Low-dose, Low-energy SIMOX

In 1991, the first report of low-energy, low-dose SIMOX material was published.[44] The advantages of this technique include lower implant times (reduced fabrication costs), high quality Si device layers (the lower dose yields less damage during implantation), and an abrupt Si/SiO_2 interface due to the decreased straggling of the implanted ions. Various authors demonstrated SIMOX formation between 30-90 keV and doses of 1.5-3x10^{17} O/cm^2, with very low defect densities.[45-47] In general, these SOI films are used only for fully-depleted devices. Given the advantages of this technique, extensive process optimisation is currently being pursued.

1.4 Scope of the present work

A variety of methods for producing SOI material have been reviewed. Presently, the most mature of these technologies is the SIMOX technique. Several methods of SIMOX material production resulting in a low-defect-density Si overlayer were presented. However, a complete understanding of the formation of dislocations within the Si overlayer has not been achieved. Further refinements to the SIMOX process as well as a more economical production of SIMOX material require a better understanding of the mechanisms of dislocation formation.

The high-current, high-energy ion implanter at the ANU was used to form SIMOX material with MeV ions. The advantages of utilising such high implant energies to study defect formation in SIMOX material are twofold. First, the lower average rate of nuclear energy deposition within the Si overlayer inherent in high-energy irradiation makes it an ideal candidate for the production of low-defect-density, single implant and anneal SIMOX material. This process would result in a lower

substrate cost. It also makes the exploration of low-temperature SIMOX material production possible. Such investigations are presented in Chapter 3.

Secondly, by virtue of the extended ion range, the damage at the ion end-of-range and within the Si overlayer are spatially separated, making it easier to study dislocation formation mechanisms in these two regions. The measurement of strain was used to indirectly study point defect types and interactions within high-energy O-implanted Si. Samples fabricated at various doses and implant temperatures were examined in order to gain a greater understanding of dislocation formation on an atomic scale in this material. The primary experimental tools utilised were double crystal x-ray diffraction (a very sensitive technique for studying strain in ion-implanted layers) and transmission electron microscopy to study defect microstructures. A discussion of strain accumulation and relief in relation to dislocation formation is presented in Chapter 4.

This more detailed understanding of dislocation formation in SIMOX material led to the exploration of "defect engineering" as detailed in Chapter 5. The implantation process was utilised to introduce specific types of defects at critical depths with the aim of reducing dislocation formation through the engineering of defects. Finally, the major findings presented in this work are summarised in Chapter 6 along with suggestions of future study.

Chapter 2

Experimental Techniques

2.0 Introduction

This chapter is divided into two parts, sample preparation and sample characterisation. Samples were fabricated using a high-current, high-energy ion implanter in conjunction with high-temperature annealing. Characterisation was performed with a variety of analytical techniques including Rutherford backscattering/channeling (RBS/C), transmission electron microscopy (TEM), double crystal x-ray diffraction (DCXRD) and variable-energy positron annihilation spectroscopy (VEP). The descriptions in the following sections are necessarily brief and a basic familiarity with some of these techniques is assumed.

2.1 Sample preparation

2.1.1 Ion Implanter

All implantation reported in this work was performed on a National Electrostatics Corporation ion implanter (model 5SDH-4) which is pictured in Figure 2.1. The ion source is a SNICS (Source of Negative Ions by Cesium Sputtering)

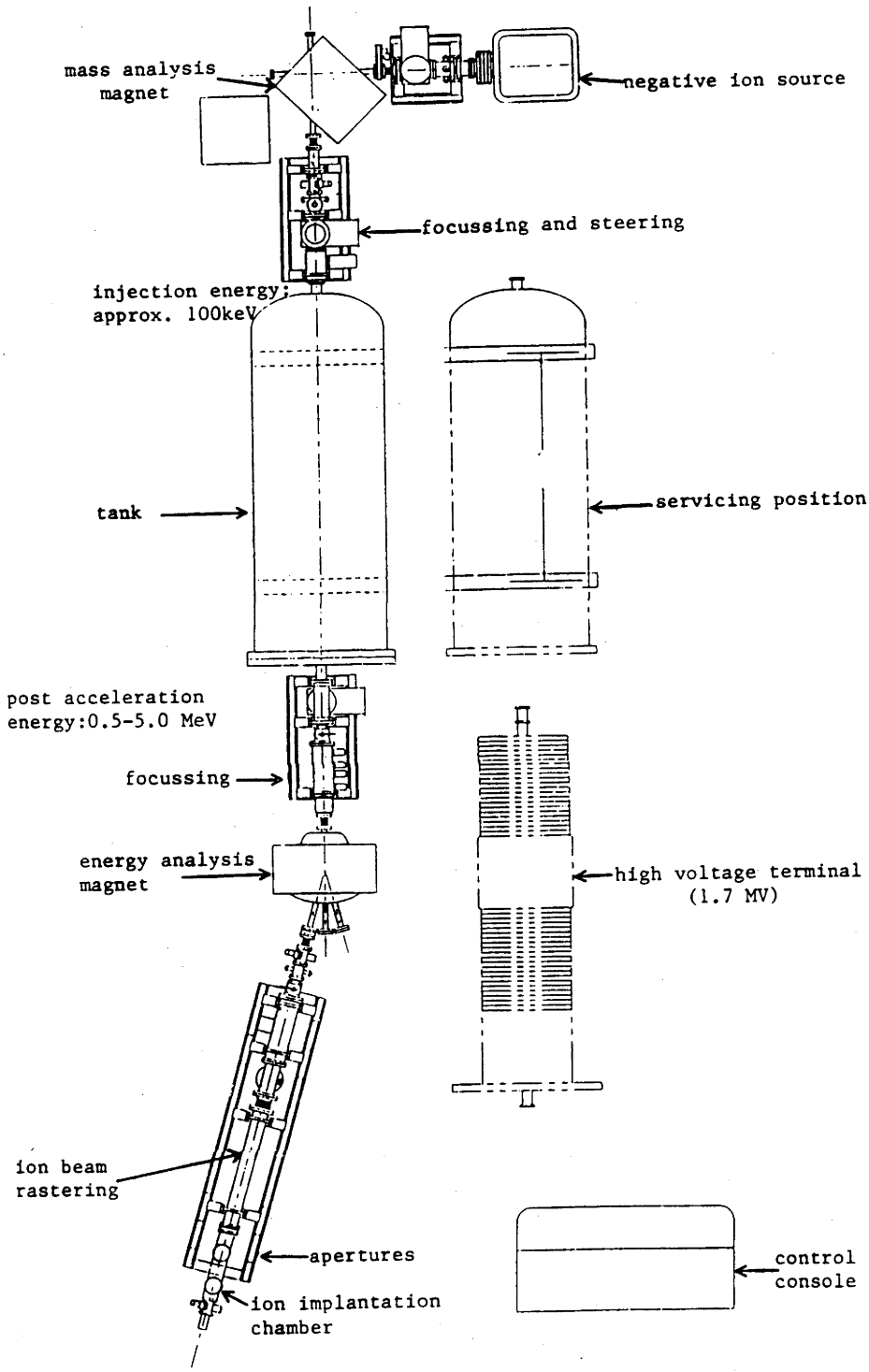

Figure 2.1: Schematic of the NEC 1.7 MV Tandem ion implanter.

type wherein positive Cs ions are attracted toward a negatively-biased Cu cathode filled with a powdered source of the element to be implanted. For instance, powdered Al_2O_3/Ag (1:1 by volume) and Si are the source materials for O and Si ions, respectively. Sputtered negative ions are accelerated through a potential difference (V_o) of magnitude $\leq$ 100 kV and thereafter exit the ion source.

A 90° magnet is then utilised for mass-filtering. If the Lorentz force on a charged particle ($\underline{F} = nq\underline{v} \times \underline{B}$) is set equal to the centrifugal force on the ion as it is deflected through a radius (R), the strength of the magnetic field (B) required for the desired mass (m) is:

$$B = \frac{1}{R}\sqrt{\frac{2mV}{qn}} \qquad (2.1)$$

where V = accelerating potential, n = ion charge state and q = electron charge. Typical O and Si ion beam currents achievable after mass filtering were ~150 μA.

The tank depicted in Fig. 2.1 contains a 1.7 MV tandem accelerator. The high voltage terminal gains a high potential by the accumulation of positive charge; a moving chain of metal pellets connected by insulating links transports positive charge drawn from ground to the high voltage terminal. The voltage is sustained through a series of equipotential rings. The desired voltage is maintained by a series of corona points which leak off any additional charge.

The negative ions are injected into the accelerator and accelerated towards the positive terminal. There they are partially stripped of electrons in a gaseous charge exchange cell to become positively charged and are subsequently further accelerated away from the terminal as positive ions. The final ion energy is:

$$q\,(V_o + (1+n)*\text{terminal voltage}) \qquad (2.2)$$

(assuming the ions are monatomic, i.e. not molecular) where n = the charge state of the ion. Ion can be accelerated to ~0.2 to 10 MeV, where the maximum achievable energy is limited by the maximum attainable charge state of a given ion. If no stripping gas is used, negative ions are accelerated then decelerated through the terminal potential, emerging with the initial injection energy. The reader is referred to Rosenblatt[48] for a more complete description of the operation of a tandem accelerator. Finally, a second electromagnet is utilised for energy filtering and then the ion beam is electrostatically scanned over an area-defining aperture situated ~30 cm from the sample.

The target holder consists of a four-sided block of Cu or Ni with vertical translation and rotation capabilities. The sample is clamped to the block in as many

places as possible and, unless otherwise noted, conductive Ag paint is used to establish better thermal contact between the sample and target holder. A cartridge lodged inside the target holder provides heating. Alternatively, the target holder can be cooled with liquid nitrogen. An embedded k-type thermocouple measures the block temperature. Implant temperatures quoted in this thesis are the temperature of the target holder. Estimates of the error in sample temperature are discussed below.

Accurate dosimetry is determined with a capacitative-based charge integrator. Secondary electron emission is suppressed by a Cu cage maintained at -300 V that surrounds the target holder. In addition, the cage is cooled by liquid nitrogen to improve the local vacuum. The sample holder is electrically isolated from the suppression shield and ground. To minimise contamination due to the cracking of residual hydrocarbons on the sample surface, the pressure in the sample chamber was maintained at $\leq 5 \times 10^{-7}$ Torr during implantation. The aperture defining the implantation area is made of Si to minimise contamination resulting from sputtering.

High-energy implants are susceptible to temperature rises due to the high power of the incident ion beam. The sample temperature is determined by the input power of the ion beam, the radiative heat losses at the sample surface and conductive heat transfer to the target holder. It has been shown[49] that in the absence of conductive heat losses and with a beam power of 1.6 Watts/cm^2, the equilibrium wafer temperature is reached within 45 seconds, i.e. instantaneously as compared to the duration of a high-dose implant. In the present work, good thermal contact was made between the sample and target holder by utilising Ag paint on the backside of the wafer in addition to clamping. After the equilibrium temperature has been reached, the wafer temperature can be calculated by setting the ion beam power equal to the radiative heat losses plus the conductive heat transfer. If good thermal contact between the sample and the target holder is achieved, conductive heat losses will be limited by the thermal conductivity of Si. Thus, the wafer temperature can be calculated:

$$\frac{P_b}{A} = 2\sigma\varepsilon(T_W^4 - T_{Surr}^4) + \frac{k(T_W - T_{tar})}{x} \qquad (2.3)$$

where P_b = power of the incident ion beam, A = area of implantation, σ = Stefan-Boltzman constant (5.67×10^{-12} W/cm^2-K^4), ε = emissivity of the target (0.35), T_W = wafer temperature, T_{surr} = temperature of the surroundings, k = thermal conductivity of the wafer (~1 W/cm-K for Si), T_{tar} = target holder temperature and x = wafer thickness (0.035 cm). T_{surr} was taken to be -150°C due to the temperature of the cold shield that surrounds the target holder. T_{tar} is the temperature measured by the thermocouple embedded into the target holder.

At the implant temperatures ($\leq$ 450°C) and ion beam powers ($\leq$20 W/cm^2)

utilised in this work, the conductive heat transfer to the target holder dominates. Equation 2.3 predicts that heat conduction through the wafer is such that the sample temperature does not exceed 1°C more than the target holder temperature even with a 20 W/cm^2 ion beam. In the absence of conductive heat transfer, equation 2.3 predicts that an input power of 10 W/cm^2 would result in an equilibrium sample temperature of ~973°C. However, clamping of the sample to the target holder even without Ag paint results in conductive heat transfer so the actual sample temperature will be much less than 973°C. The use of Ag paint will increase heat transfer and result in better temperature control and hence, a lower sample temperature.

An in-situ optical pyrometer could have yielded a more accurate measurement of the Si wafer temperature during implantation. That technique was unavailable so estimates of the implant temperature error were attained by studying the damage and strain within the Si overlayer with changes in the implant temperature. As shown in subsequent chapters, damage and strain within the Si overlayer of unannealed SIMOX material are strongly dependent on implant temperature. Consequently, RBS/C and strain measurements were used as an indicator of Si overlayer damage and hence implant temperature. Variations in the ion beam power for a given O dose did not affect the amount of damage and strain at implant temperatures of 300 or 450°C. Temperature control is consequently assumed to be good at implant temperatures of 300 and 450°C. At 150°C, the damage significantly increased with ion beam power, as expected, but never reached the same level as observed after 300°C implantation. Either the increased ion beam power resulted in an increased wafer temperature, or dose rate effects were observed. Because the ion beam power is so high, we are probably observing the effect of increased sample temperature. Based on strain measurements and the accurate temperature control that was observed with 300°C implantation, the actual temperature for 150°C implantation is assumed to be much less than 300°C.

2.1.2 Furnace Annealing

A Lindberg single-zone furnace equipped with an Al_2O_3 tube was used for annealing. Annealing of O-implanted Si in an non-oxidizing ambient or in vacuum has been shown to produce severe pitting of the Si due to the formation of volatile SiO at the surface.[50] The formation of SiO is favoured over SiO_2 at O partial pressures below 1 Torr at 1350°C.[51] Thus, annealing is generally performed in an oxidizing ambient with or without a SiO_2 capping layer. The use of a SiO_2 capping layer minimises the consumption of Si during the annealing/oxidation process.

In this work, a SiO_2 capping layer was deposited either by Plasma Enhanced

Chemical Vapour Deposition (PECVD) or via Spin-on-Glass (SOG). With a sufficiently thick capping layer (5000 Å), Si consumption from the overlayer was minimised. Samples were annealed in 1-3% O in Ar. These concentrations of O are sufficiently high to prevent pitting of the surface and, in the absence of a capping layer, resulted in an SiO_2 layer thickness of 2000 Å - 4000 Å thick (consuming ~950-1800 Å of the Si overlayer).

2.2 Sample Characterisation

2.2.1 Rutherford Backscattering

With the RBS technique, a beam of monoenergetic light ions impinges on the target to be analysed. The energy distribution of backscattered ions is subsequently measured and the depth distribution of the target constituents can be determined. The target can be oriented such that incident beam is aligned with a low index crystallographic direction such that a large portion of the incident beam is effectively "channeled" into the crystal by collisions with the regularly spaced lattice atoms. If the beam is oriented so that it is not aligned with any particular crystallographic direction (i.e. in a random orientation), channeling is inhibited. Channeled ions penetrate further into a crystal with less energy loss and fewer major interactions than occur for ions of random incidence. When channeled incident ions encounter damage in the target, the rate of dechanneling is increased and consequently the contribution of the random component to the backscattered ion yield is increased. The yield will be increased according to the structure and the magnitude of the disorder. Hence, channeling measurements can provide information on the depth distribution of disorder. The channeling minimum yield (χ_{min}) is the ratio of the yields in a channeled orientation to a random orientation and can be used as a qualitative measure of crystal quality.

The van de Graaff accelerator utilised for RBS is pictured in Figure 2.2. The ion source is situated at one end of the terminal. He ions are created when He gas is introduced between two RF electrodes. These ions are then anodically repelled out of the ion source into the accelerator. High voltage is generated when a charging screen draws positive charge from ground and transfers it to an insulated belt which carries the charge to the terminal. Once the terminal is sufficiently charged, it is maintained at the desired voltage by removing charge at the same rate it is applied. Removal of charge occurs through the accelerated ions, the column current and the corona current. Within the column, a series of equipotential rings separated by resistors provide a gradual

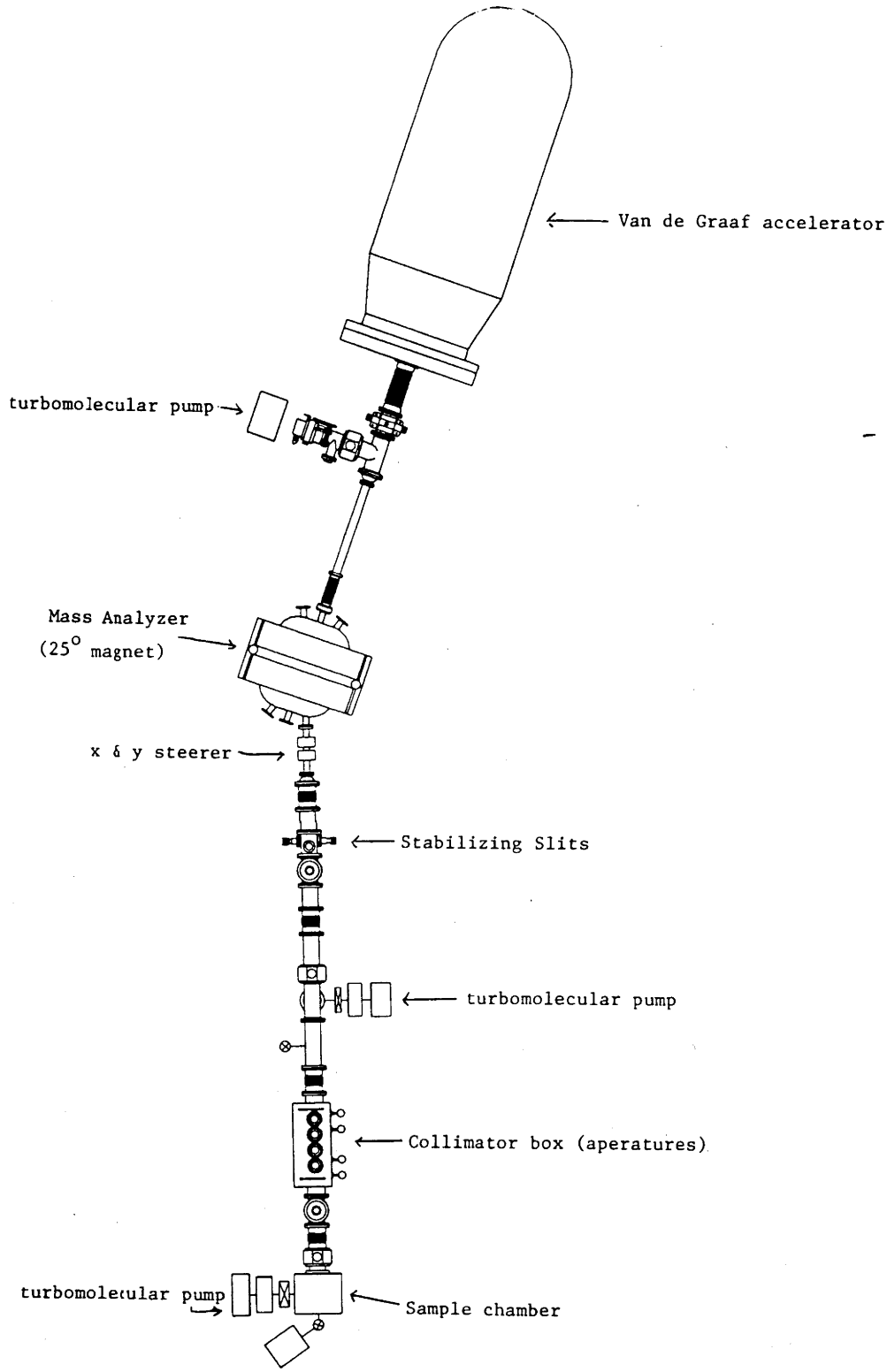

Figure 2.2: Schematic of the 2 MV van de Graaff accelerator used to perform RBS measurements.

voltage drop to ground. The tank housing the terminal and column contains an insulting gas, in this case a N_2/CO_2 mixture, to prevent discharge of the high voltage terminal.

A Au-surface barrier (Schottky barrier) detector at a scattering angle of 168° (unless otherwise noted) detects backscattered particles. When particles impinge on the detector, electrons and holes are created and swept out of a depleted region. The resulting current pulse is proportional to the energy of the backscattered particle. The current/voltage pulse is routed through a pre-amplifier (amplification and pulse shaping) and amplifier (amplification and pulse shape analysis) to a multi-channel analyser (MCA). The MCA has 512 channels with a calibration of ~4 keV/channel.

2.2.2 Transmission Electron Microscopy

2.2.2a Operation

Another method of identifying damage in ion-implanted samples is Transmission Electron Microscopy (TEM). If the kinetic energy gained by an electron accelerated through a potential difference V, is set equal to the de Broglie equation relating wavelength and momentum, the electron wavelength (λ) is:

$$\lambda = \frac{h}{\sqrt{2m_0qV\left(1+\frac{qV}{2m_0c^2}\right)}} \qquad (2.4)$$

where m_0 is the mass of an electron and c is the speed of light. With an accelerating voltage of 200 kV, the electron wavelength is 0.025 Å. Since interatomic spacings are of the order of Å, electrons make an ideal "probe" for imaging atoms.

The TEM studies in Chapter 3 were performed on a Hitachi 800 TEM and in Chapters 4 and 5 on a JOEL 2000CX TEM. An accelerating voltage of 200 kV was used throughout this work. A ray diagram of a TEM is pictured in Figure 2.3. The essential features are: a source of electrons, a series of condenser lenses to adjust the illumination of the specimen, the specimen (object), an objective lens which does most of the magnification and the projector lens which further enlarges the image formed by the objective lens and projects it onto a fluorescing screen. The electron source is either a W or LaB_6 filament heated to 2200 to 2400°C to liberate electrons. The electrons are

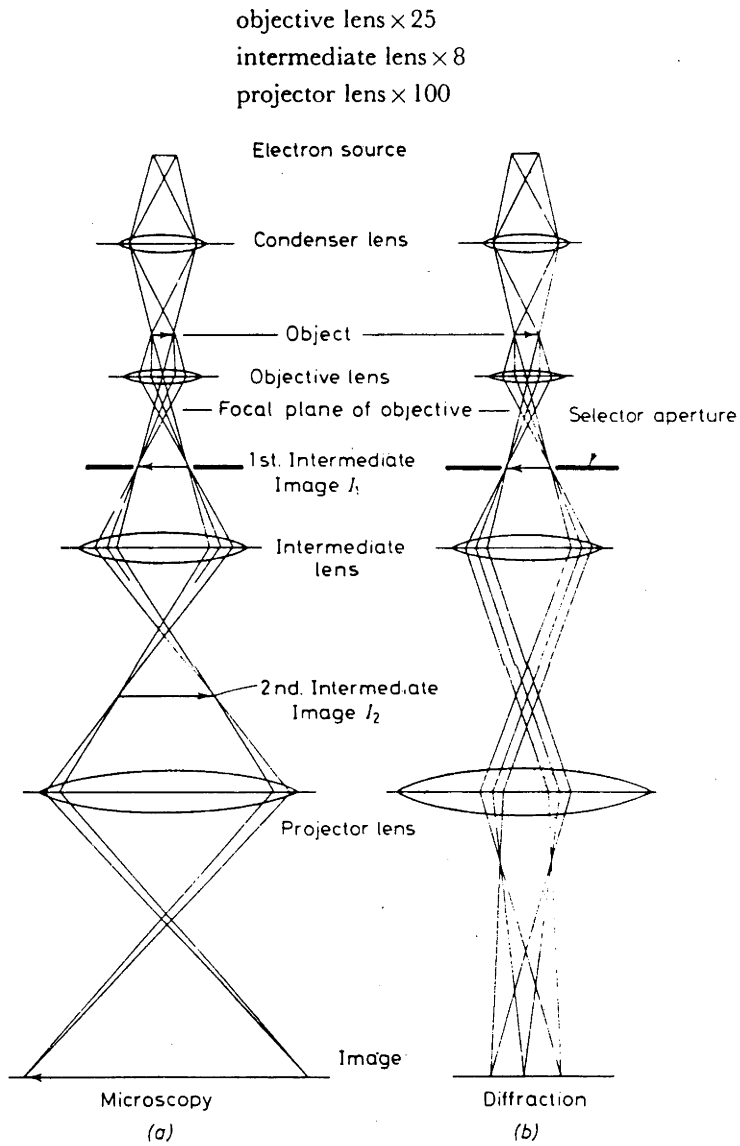

Figure 2.3: Ray paths in a transmission electron microscope (a) under microscopy conditions and (b) under diffraction conditions.[52]

accelerated through a potential difference towards ground. Contrast in a specimen arises from phase and diffraction contrast.

A TEM can be used in various modes. A bright field image results when only the transmitted beam is used to form the image, with the objective aperture prohibiting a diffracted electron contribution to the final image. Hence, only the direct beam (and any low-angle inelastically scattered electrons) forms the specimen image. If the objective aperture is aligned with a diffracted beam, a dark field image is produced. Bright areas on the dark field image result from features that satisfy the Bragg condition for the diffracted beam orientation. Finally, the sample can be tilted in both the x and y planes to orient the beam along a given crystallographic direction. For the majority of the microscopy presented in this work, the sample was oriented in the [110] direction, then tilted 2° off-axis for enhanced contrast. The reader is referred to Hirsch, et al[52] for a thorough description of TEM operation.

2.2.2b Sample Preparation for Cross-Sectional TEM (XTEM)

To view a specimen with TEM, the region of interest must be sufficiently thin for electron transmission. Electron transparency is dependent on a number of parameters such as the electron scattering factor (which increases with atomic number), the number of electrons scattered off the electron-optical axis, and the orientation of crystalline material. The minimum thickness for electron transparency at an accelerating voltage of 100 kV varies from several microns in Al to ~0.1 μm in U.

XTEM samples in this work were prepared by mechanical polishing, followed by dimpling and ion-beam thinning. Two samples, with the implanted sides facing each other, were glued together. Mechanical polishing of the surface perpendicular to the glue seam is accomplished using successively finer grades of SiC paper until ~60 μm of material is left. (See Figure 2.4(a). The sample is then dimpled (i.e. a 10 mm wheel further thins the specimen centre) resulting in a minimum thickness of ~20 μm at the sample centre as pictured in Figure 2.4(b). The process of dimpling allows for thick sample edges that yield superior mechanical support while also producing the thinnest region at the centre of the sample, the centre of the sample being the region of interest. The sample is supported at the edges by a 3 mm Cu grid. Finally, an ion beam miller thins the sample to the thickness required for electron transparency. Figure 2.4(c) is a schematic of ion-beam thinning. Two ion guns are situated opposite each other at 75° from the sample normal. Ions are accelerated through a potential difference of 5 kV and directed towards the sample. The specimen is rotated at a rate of 2 revolutions/minute to evenly thin the sample at a rate of ~6 μm/hour.

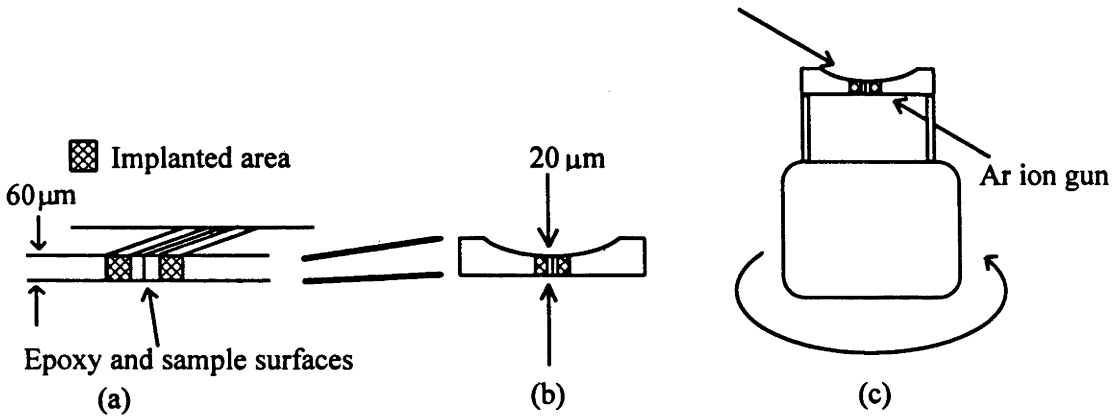

Figure 2.4: XTEM sample preparation steps: (a) Implanted faces glued together and mechanically polished, (b) sample after dimpling, (c) ion beam thinning of the sample.

2.2.3 Double Crystal X-Ray Diffraction (DCXRD)

DCXRD analysis is a non-destructive technique widely used for compositional and structural analysis of thin films. It can be utilised to obtain a quantitative measurement of lattice strain which is measurable to 1 part per million (ppm). By comparison with theoretical rocking curves (RCs), depth distributions of lattice strain can be obtained.

Figure 2.6 shows the experimental arrangement of a double crystal diffraction system. A Bede QC2a diffractometer functioning in a (+,-) non-dispersive parallel arrangement (identical crystals for the reference and sample crystal, which are arranged anti-parallel to each other) was used in this work. Cu K_α x-rays are incident on a reference crystal of the same material and orienatation as the sample. The reference crystal acts as a monochromator, removing the wavelength dispersion inherent in an x-ray source. X-rays are diffracted when the incident angle θ, is equal to the Bragg angle. The Bragg condition is:

$$n\lambda = 2d\sin\theta_B \qquad (2.5)$$

where d is the spacing between crystallographic planes, λ is the x-ray wavelength, n is the order of diffraction (n=1,2,...) and θ_B is the Bragg angle (34.564° for (004) Si). The slits in front of the detector transmit only Cu K_α radiation yielding better resolution,

while a scintillation detector measures the diffracted x-ray intensity. Because the specimen and reference crystal are parallel, only x-rays satisfying the Bragg condition for both crystals reach the detector. The extinction depth (the depth at which the x-ray intensity falls to 1/e of the initial intensity) is given by:

$$L_e = \frac{V_c}{2\lambda r_e F_h} \sin\theta_B \qquad (2.6)$$

where r_e = classical electron radius, F_h = real part of the structure factor and V_c = volume of the unit cell.[53] For Cu K_α radiation incident on (004) Si at the Bragg angle, $L_e = 4.82\ \mu m$.

The sample is "rocked" through some angle ω, by tilting the sample as indicated in Figure 2.5. The detector is simultaneously moved through an angle 2ω and the diffracted x-ray intensity as a function of detector angle is recorded. A substrate peak as well as satellite peaks from any variations in lattice spacing due to mismatch, strain and/or compositional differences appear in the spectra when $\omega=\theta_B$. The differential form of Bragg's law relates the strain and therefore the difference in lattice parameter between the layer and substrate to the angular separation $\Delta\omega$, of the their Bragg peaks:

$$\frac{\Delta d}{d} = (-\cot\theta)\,\Delta\omega\,. \qquad (2.7)$$

Peaks to the right of the substrate peak are due to a lattice contraction (tensile strain) while peaks to the left of the substrate peak are due to lattice expansion (compressive strain). In ion-implanted material, the angular separation between peaks is determined by the difference in lattice spacing between the implanted layer and substrate. The intensity and width of the diffraction peak is related to the thickness, depth, composition and structural damage of the strained layer.

For thin epitaxial layers, fringes appear in the RC which can be used to calculate layer thicknesses. Each layer will give rise to a specific periodicity in the rocking curve. This characteristic period ($\Delta\theta$) is given by:

$$\Delta\theta = \frac{\lambda\gamma_h}{t\sin 2\theta_B} \qquad (2.8)$$

where t = layer thickness, λ = x-ray wavelength, θ_B = Bragg angle, and γ_h = cosine of the angle between the inward surface normal and the diffracted beam.[54] For a more complete review of high resolution x-ray diffraction see Wie[53] or Tanner, et al.[55]

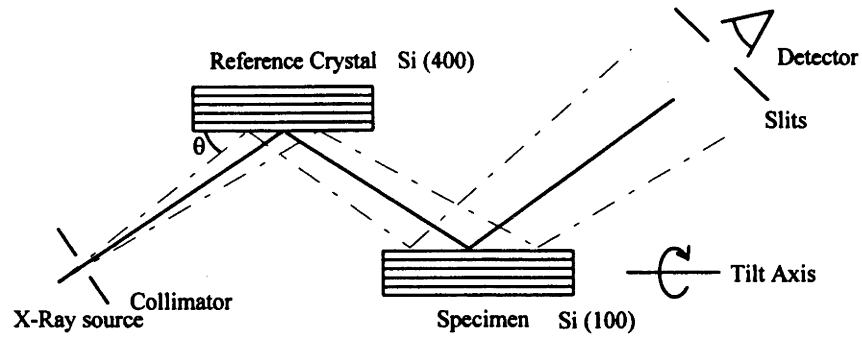

Figure 2.5: Schematic of a double crystal x-ray diffractometer.

2.2.3a Depth Distribution of Strain in Ion-implanted Material

Several models for the evaluation of strain in ion-implanted material have been reported (see Table I). Typically, the strain depth distribution is modeled after the displaced atom distribution. It has been reported that strain due to interstitials is an order of magnitude higher than that due to vacancies.[56] Indeed, Pesek, et al[57] noted that the strain profile in Ge-implanted Si was proportional to a linear combination of the damage and ion distributions; at low doses, the strain was proportional to the damage distribution while at high doses it was proportional to the ion distribution. More recently, a fitting procedure for RC analysis in ion-implanted semiconductors was reported wherein strain caused by implantation-induced vacancies was neglected due to the aforementioned studies.[58]

Under common experimental conditions (room temperature and a dose of ~10^{15}-10^{16} ions/cm^2), compressive strain measured in ion-implanted material is due to the displaced atom distribution. However, as evident in Chapter 4 as well as other reports,[39,59,60] tensile strain is also measurable in ion-implanted material. In B-implanted Si, tensile strain is caused by substitutional B atoms which have a smaller tetrahedral radius than the Si lattice and hence, a lattice contraction results.[61] In Chapter 4, the spatial separation of Frenkel pairs (which results in an implantation-induced vacancy excess at depths < R_p and an implantation-induced interstitial excess at depths ~ R_p) is shown to give rise to a lattice contraction. Upon formation of an amorphous layer (assumed to be strain free) near R_p, the contribution of interstitial-type defects to the measured strain is negated and as a consequence the RC is dominated by the presence of

Author	Materials system	Modeled strain distribution	Comments
MacNeal et al[62]	Ne,B,He-implanted magnetic bubble garnet materials	∝ damage (nuclear displacements) distribution * ion distribution	signal disappeared upon amorphous layer formation
Pesek et al[57]	Ge-implanted Si	∝ damage (nuclear displacements) distribution * ion distribution	-
Servidori[59]	Si-implanted Si	∝ displaced atom density	negative strain appeared after onset of amorphisation
Paine et al[63,64]	He,B,C,Ne,Si,P,Te-implanted GaAs	∝ energy deposited into nuclear collisions	-
Hart et al[65]	Si,Ar-implanted Si	∝ displaced atom density	-
Berti et al[66]	N-implanted Si	∝ displaced atom density (correlated with RBS/C measurements)	area under the (DCXRD) strain peak saturated after amorphisation
Bai et al[67]	Si-implanted Si	∝ displaced atom density	-
Fabbri et al[61]	B,Ge-implanted Si	∝ displaced atom profile and lattice expansion/contraction due to implanted ion substitutionality	negative and positive strain evident at all doses
Ellingboe et al[68]	O,Si-implanted Si	∝ implantation-induced vacancy excess depth profile	only negative strain evident (all samples had an amorphous layer at R_p)
Venables et al[39]	O-implanted Si	∝ excess point defect profile	positive strain at low doses and negative strain at high doses
Zhou et al[69]	O-implanted Si	∝ vacancy-rich region ahead of O ion end of range	negative strain evident, only high doses reported ($\geq 8 \times 10^{17}$ cm^{-2})

Table I: Reports of strain models in ion-implanted material.
(∝ = proportional to)

vacancy-type defects at lesser depths. (It is assumed the implant temperature is high enough to reduce the number of displaced atoms in the surface layer such that the point defect profile in this region is dominated by vacancy-type defects.)

2.2.3b Rocking Curve Analysis by Dynamical Simulation (RADS)

Simulations of RCs in this work were performed with the software package RADS[70] which uses the solution of the Takagi-Taupin equations[71,72] of dynamical theory for the analysis of strain in epitaxial thin films. Trial strain distributions (based on implantation parameters, TRIM90[73] simulated point defect depth distributions and XTEM analysis) are iteratively entered into RADS until a reasonable agreement between theory and experiment results. Given the depth-dependent defect distribution in ion-implanted material, the interpretation of RCs from ion-implanted material is difficult. In addition, the diffuse scattering of x-rays (Huang scattering) due to implantation-induced extended defects can greatly influence the calculated strain profile.[74] Typical RCs have a high background signal from the extended defect formation. Furthermore, complex strain profiles must be modeled RADS as thin layers of discrete strain levels. However, changes in strain with implanted dose and/or temperature variations are readily apparent from RADS simulations and the peak strain can also be accurately determined.

2.2.3c Strain depth profiling in ion implanted material

As stated before, the accurate determination of strain depth distributions in heavily-damaged, ion-implanted material is challenging. In order to test the accuracy of a simulated strain profile, a sample was amorphised to various depths from the surface to 1.3 μm using a series of Si-ion implants at liquid nitrogen temperatures. (Table II lists the Si-ion implant parameters and resultant amorphisation depths.) RC simulations were then performed with the assumption that the amorphous layer was strain free.

Implant Energy (keV)	Dose (Si/cm^2)	Depth of amorphisation (μm)*
100	$5x10^{15}$	0.2
300	$5x10^{15}$	0.65
600	$5x10^{15}$	1.05

* as obtained by RBS/C measurements.

Table II: Implant parameters of Si implant amorphisations.

The sample used for this study was O-implanted Si (1 MeV, $7x10^{17}$ cm^{-2}, 225°C), where the numbers in parentheses refer to the implant energy, implant dose and the implant temperature, respectively. This format of describing implant parameters will be used henceforth to ease in the reading of this thesis. The experimental and simulated RC for this sample are shown in Figure 2.6. The inset shows the strain profile used in the RADS simulation. In Figure 2.7, the RC for the same sample but after amorphisation to 0.2 μm is pictured. Again, the inset shows the same simulation used as in Figure 2.6 but with the strain in the implantation-induced amorphous layer set equal to zero. A close fit between experiment and simulation results in both cases indicating that the strain peak at ~100 arcsec in Fig. 2.6 was due to strain in the top 0.2 μm of the Si. After amorphising the sample even further to 0.6 μm and setting the strain to zero in the RADS simulation over this depth, a good fit between the simulated and experimental RCs again results (Figure 2.8). No secondary strain peaks were evident in the RC for the sample amorphised to 1.05 μm (not shown) indicating that all of the strain was contained in the first 1.05 μm i.e. in the Si overlayer.

To the author's knowledge, this is the first report of the use of amorphisation to deduce a strain-depth distribution. A disadvantage of this technique is the potential introduction of interstitials into the residual crystalline region at depths greater than the amorphous layer resulting from Si implantation. Such interstitials could partially compensate residual tensile strain. However, given the low temperature and dose of the Si implants relative to that of the O implants, such effects were considered minimal. This supposition is consistent with the extent of agreement between simulated and experimental RCs in Figures 2.6 - 2.8.

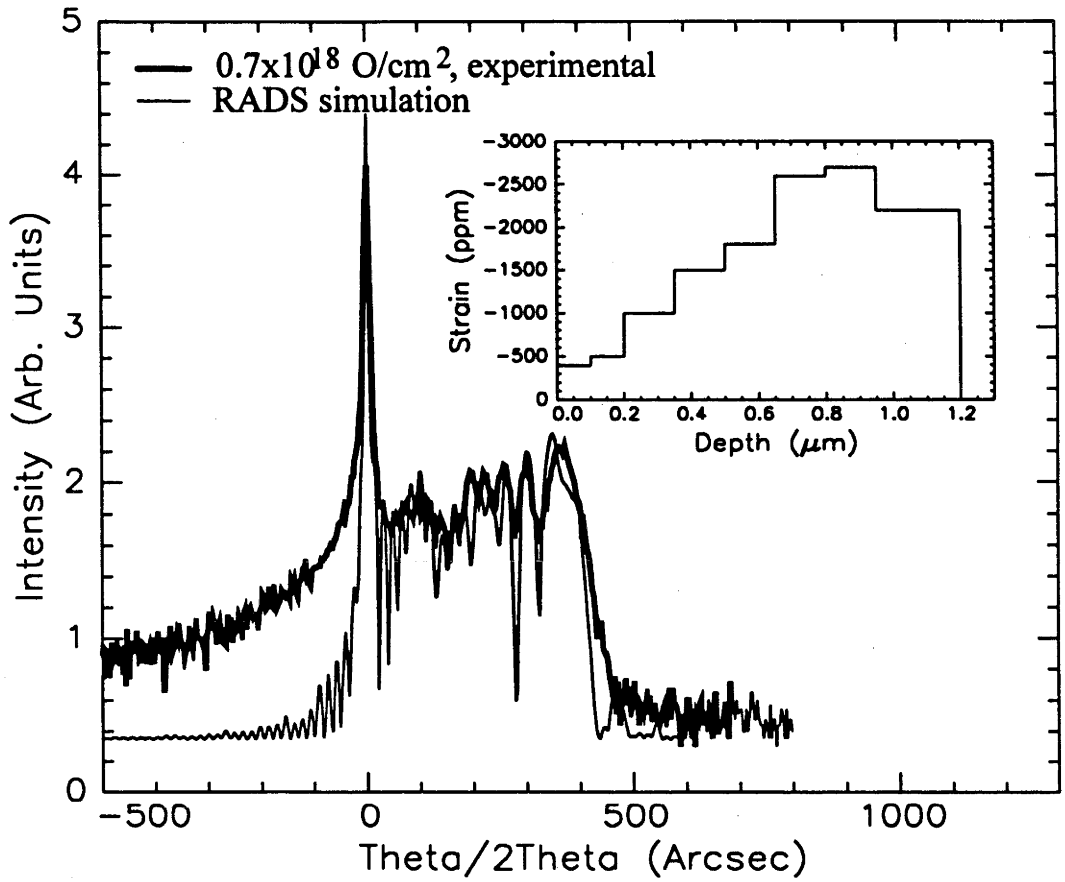

Figure 2.6: DCXRD spectra for the O-implanted Si sample (1 MeV, $7x10^{17}$ cm^{-2}, 225°C). The RADS simulated curve is overlayed. The inset shows the strain profile used in the simulation.

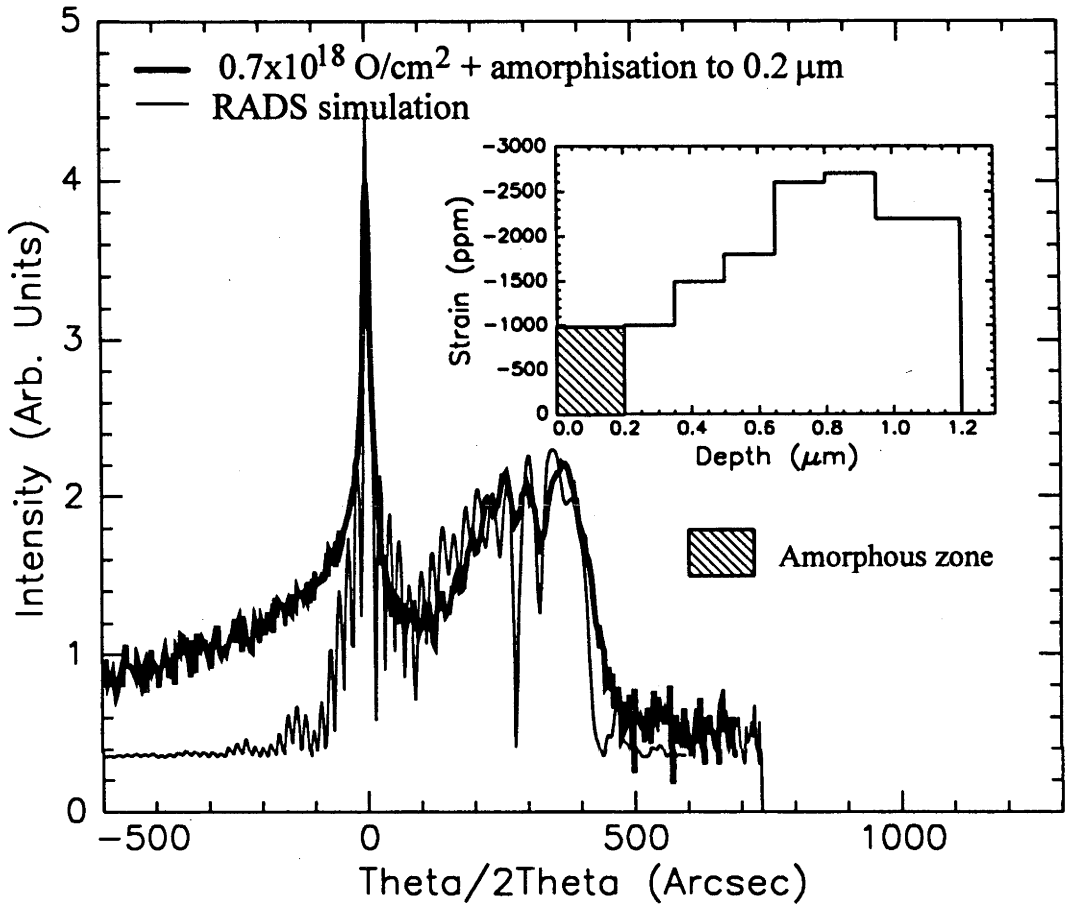

Figure 2.7: DCXRD spectra for the O-implanted Si sample (1 MeV, $7x10^{17}$ cm^{-2}, 225°C) after amorphisation to 0.2 μm. The RADS simulated curve is overlayed. The inset shows the strain profile used in the simulation

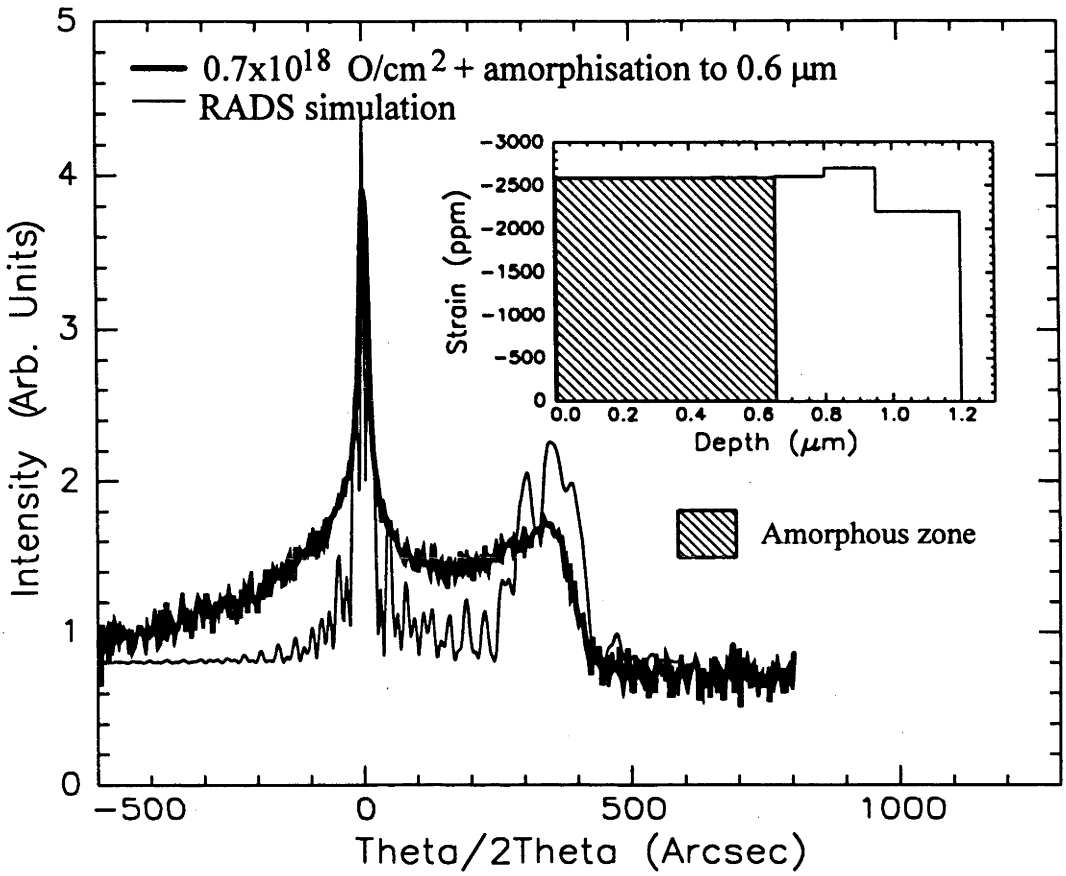

Figure 2.8: DCXRD spectra for the O-implanted sample (1 MeV, $7x10^{17}$ cm^{-2}, 225°C) after amorphisation to 0.6 μm. The RADS simulated curve is overlayed. The inset shows the strain profile used in the simulation.

2.2.4 Variable Energy Positron Annihilation Spectroscopy (VEP)

Energetic positrons incident on a solid will rapidly thermalise upon contact and diffuse through the solid. After spending the majority of their lifetime in this freely diffusing state, positrons will annihilate with electrons in the solid. The probability of a positron annihilating with an electron from a given momentum state is determined by the overlap of its wave function. The annihilation γ-rays emitted will be Doppler-broadened about the mean energy of 511 keV due additional electron momentum (or energy). The γ-ray distribution can be measured directly using the angular correlation of the annihilation radiation (ACAR) technique[75] but it is more common to employ Doppler-broadening spectroscopy which is faster and more economical.[75,76] (The latter technique was used in this work.)

Thermalised positrons have a high probability for capture and annihilation in open volume (i.e. vacancy-type) defects.[77] When an open-volume defect is encountered by a diffusing positron, the positron will rapidly ($\sim 10^{-15}$ sec) be localised by the defect. Trapping of the positron results in the overlap of the positron wave function with the core electrons to either be reduced (vacancies) or increased (impurities) and the lineshape of the γ-ray distribution is accordingly narrowed or broadened. The annihilation lineshape is usually characterised by an S ("*S*harpness") or W ("*W*idth") parameter. The definition of these parameters is illustrated in Figure 2.9 and the specific γ-ray energies over which the W and S parameters were measured is stated. The response of the positron wave function in different trap environments and the corresponding change in lineshape parameters is illustrated in Figure 2.10. The S-parameter increases as the lineshape becomes narrower while the W-parameter increases as the lineshape broadens. With the use of variable energy positrons, the probing depth may be varied and the vacancy and/or impurity-type defect depth distribution subsequently derived. This technique has been successful in studying ion-implanted Si[78-80] and the Si/SiO_2 interface.[81]

Modeling programs are available to aid in data interpretation and deduce whether annihilation has occurred from either a freely diffusing positron, trapping at the surface or trapping by a point defect. Without any guidance in the fitting procedure, there is any number of solutions. The models used in this work therefore involved a systematic study of different samples and fixing of parameters such as layer depth (which was obtained using other techniques such as XTEM or RBS). The VEP measurements reported in this work were performed by P.J. Schultz and co-workers at the University of Western Ontario using the apparatus described by Leung, et al.[81]

Lineshape Parameters

Total Peak: integrated from 504.5 - 517.5 keV

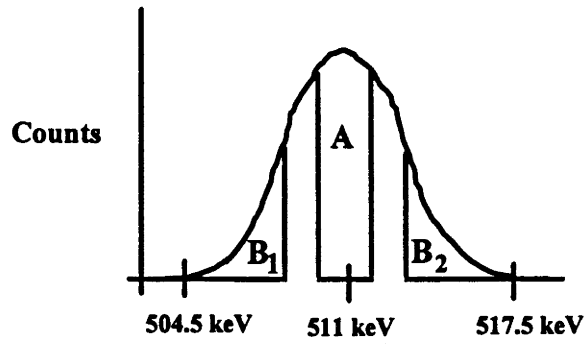

$$S = \frac{A}{\text{total peak}}$$ A is integrated over: 510.1 - 511.9 keV

$$W = \frac{B_1 + B_2}{\text{total peak}}$$ B_1 is integrated over: 507.7 - 509.5 keV

B_2 is integrated over: 512.5 - 514.5 keV

Figure 2.9: A definition of lineshape parameters, S and W.

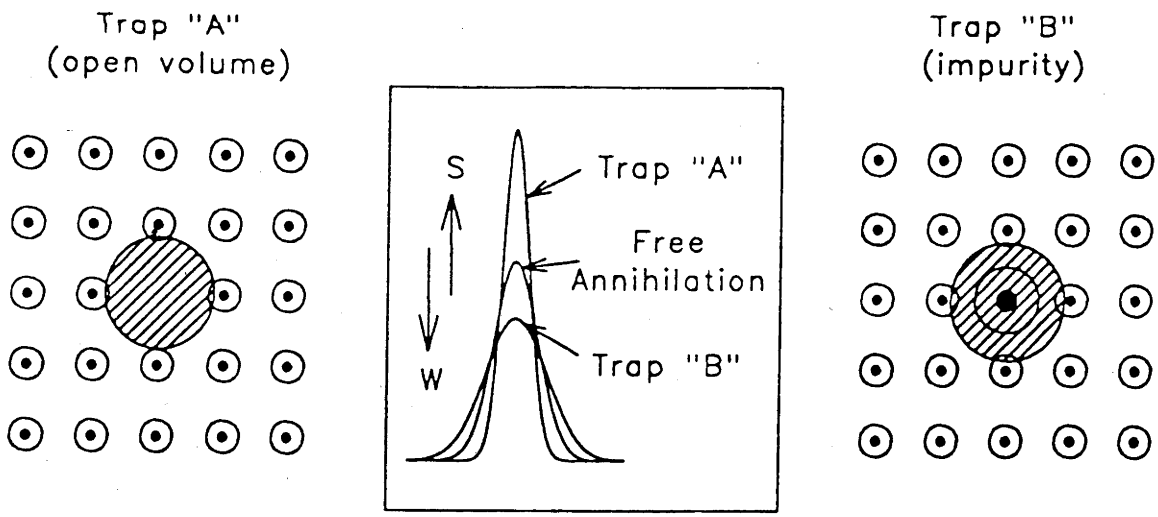

Figure 2.10: Schematic illustration of the positron wave function in different trap environments.

Chapter 3

SIMOX Substrate Formation by High-Energy O-ion Implantation

3.0 Introduction

As noted previously, "conventional" SIMOX substrates are typically formed by 200 keV O implantation in Si to a dose of 1.4×10^{18} cm^{-2}. At this dose, stoichiometric SiO_2 is formed during implantation when the peak of the O depth distribution reaches 67 atomic %. During implantation, the substrate is maintained at ~600°C to inhibit amorphisation of the Si overlayer. A post-implant anneal at high temperature (~1300°C for 4 hours) is necessary to induce O segregation from substoichiometric depths and reduce lattice disorder. If a thicker overlayer is required, an epitaxial Si layer is subsequently grown by chemical vapour deposition.

MeV ion implantation offers many potential advantages over keV ion implantation for SIMOX substrate fabrication. Due to the energy dependence of the elastic and inelastic components of the ion stopping power, for a given temperature, a lower average rate of nuclear energy deposition (and hence, damage) will result in the Si overlayer with implantation at MeV energies. As a consequence, low temperature implantation (~150°C) is possible without total amorphisation of the Si overlayer. Also, a thicker Si overlayer results by virtue of the increased ion range. However, increased straggle is inherent with increased range. Consequently, a higher ion dose is needed to

achieve stoichiometry during implantation. From TRIM90 simulations, the ion dose must be increased by a factor of ~1.5 to achieve stoichiometry when the energy is increased from 200 to 1000 keV.

To date, the author is unaware of any report of MeV O-ion implantation in Si to stoichiometric doses though several groups have investigated SIMOX substrate fabrication with sub-stoichiometric doses.[50,82-85] In the earliest report of sub-stoichiometric MeV O-ion implantation, White et al[50] found that buried SiO_2 layers from high-energy implants formed in essentially the same way as those from low-energy implants, i.e. implant temperature was the most crucial parameter in forming a uniform buried SiO_2 layer. At implant temperatures >400°C, O segregated into SiO_2 precipitates prematurely and impeded the formation of a uniform buried oxide layer. Low implant temperatures resulted in more uniform buried SiO_2 layers and the formation of polycrystalline or twinned Si at the front amorphous/crystalline (a/c) interface, depending on the annealing conditions.

In 1988, Nieh et al[82] reported 2 and 5 MeV sub-stoichiometric O-ion implantation at -197, 20 and 500°C. This was the first report of MeV, high dose O-implanted Si at and below room temperature. In such material, the defect density in the Si overlayer after a 1300°C anneal was estimated to be ~10^7 cm^{-2}, comparable to that observed in single implant and anneal SIMOX fabricated at 200 keV implant energies at a temperature of 500°C.

In this chapter, the formation of a SiO_2 layer by 1 MeV O-ion implantation to stoichiometric doses is presented. The dose, implant and annealing temperature dependencies of both defect evolution in the Si overlayer and the formation of a buried SiO_2 layer are described. The results of Si-ion implantation, performed under similar conditions to those used for the O implantation, are then presented with the aim of elucidating any chemical effects relevant to damage formation in SIMOX material.

3.1 High-Energy O-ion Implantation

3.1.1 Dependence of Damage on O Dose

Figure 3.1 shows the ion and vacancy depth distribution (as calculated by TRIM90) of O-ion implantation in Si at 200 keV and 1 MeV. The magnitude of the simulated vacancy concentration demonstrates that lattice atoms are necessarily displaced hundreds of times during such high-dose implantations. As noted previously, the doses utilised in the calculations shown in Fig. 3.1 (1.4×10^{18} O/cm^2 and

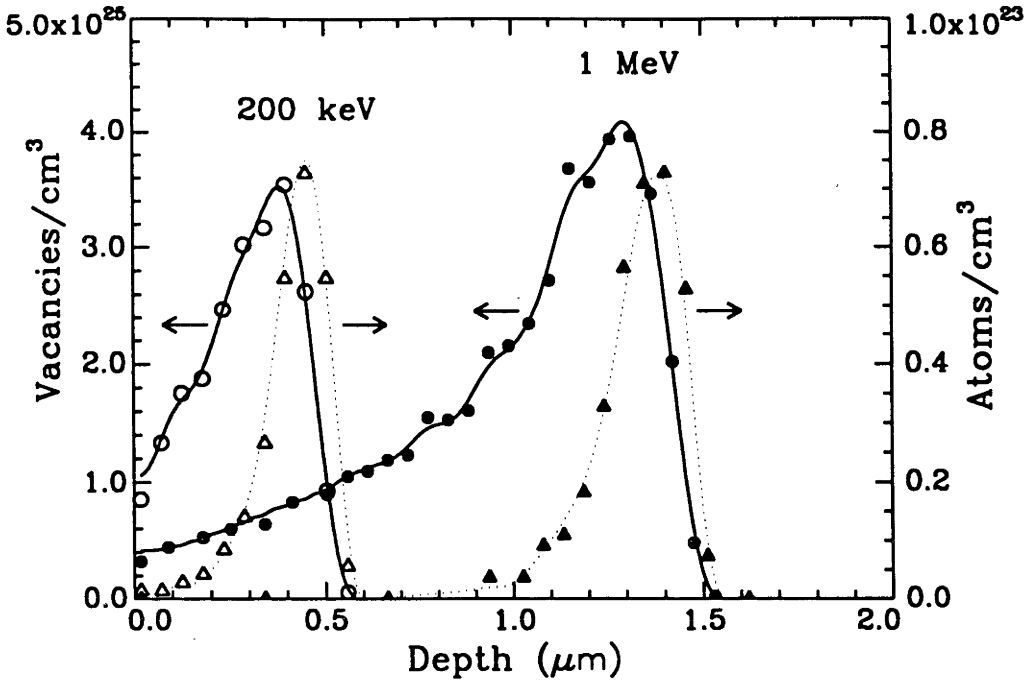

Figure 3.1: Calculated vacancy (—) and O atom (----) depth distribution at 200 and 1000 keV for doses of $1.4x10^{18}$ and $2.15x10^{18}$ O/cm^2, respectively.

$2.15x10^{18}$ O/cm^2 at 200 keV and 1 MeV, respectively) are those necessary to achieve stoichiometry during implantation. The predicted vacancy concentration at the surface is lower for 1 MeV implantation, indicating that less damage within the Si overlayer results from implantation at higher implant energies.

Initial experiments were performed with an implant energy of 1.0 MeV and implant temperatures of 150, 300 and 450°C to doses of 0.73, 1.45, 2.18, $2.64x10^{18}$ O/cm^2. Figure 3.2 shows the random and channeled RBS spectra for a 450°C implant temperature at these doses. Note the contracted depth scale for the channeled spectra at low doses (0.73 and $1.45x10^{18}$ O/cm^2) due to the difference in stopping powers between the channeled and randomly penetrating ions. An amorphous layer near the O ion $R_{p,}$ ~1.3 μm, has formed at doses $\geq 1.45x10^{18}$ O/cm^2. It is apparent that the amorphous layer is centred about the peak of the O atom concentration maximum. As expected, the width of the amorphous layer increases with dose. A dose of $2.18x10^{18}$ O/cm^2 (Fig. 3.2(c)) results in the formation of stoichiometric SiO_2 during

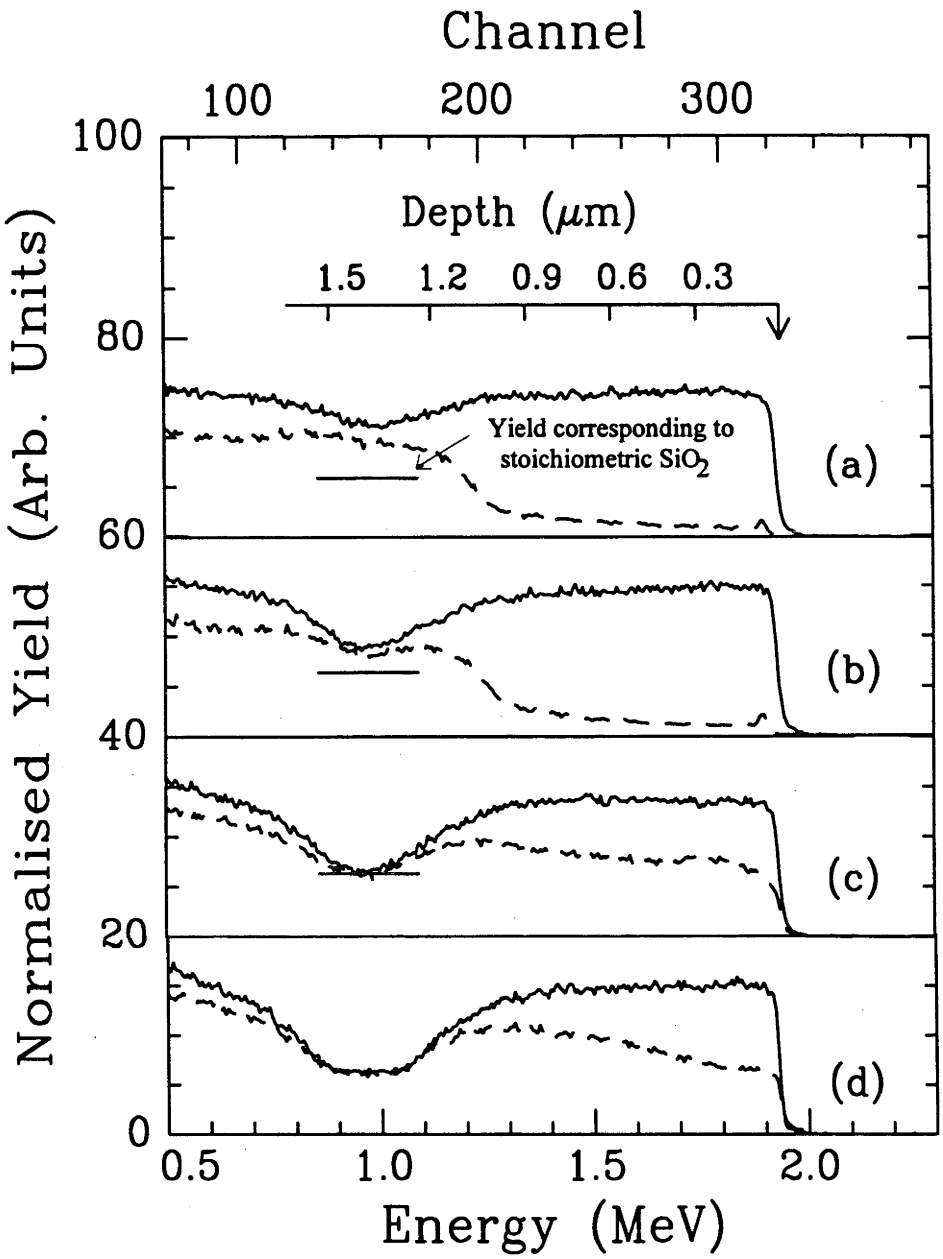

Figure 3.2: RBS/C spectra (obtained with 3 MeV He^+ ions) for a 450°C implant at various O doses: (a) $0.73x10^{18}$, (b) $1.45x10^{18}$, (c) $2.18x10^{18}$ and (d) $2.64x10^{18}$ cm^{-2}. The detector was at a scattering angle of 120°.
(—) Random (----) Channeled

implantation. At the higher dose of 2.64×10^{18} O/cm^2, the O concentration has saturated over depths of ~1.2-1.4 μm.

Damage in the Si overlayer (as measured by χ_{min}) is minimal at the two lowest doses, yet increases abruptly as the dose is increased from 1.45 to 2.15×10^{18} cm^{-2}. Further increasing the dose to 2.64×10^{18} cm^{-2}, yields little change in χ_{min}. The same behaviour is evident, but over a different dose range (see Chapter 4 for more details) for the other implant temperatures studied. Unlike low-energy SIMOX, crystallinity within the Si overlayer is maintained at doses as high as 2.64×10^{18} cm^{-2} even for implant temperatures as low as 150°C.

Figure 3.3 shows the RBS/C spectra of these samples after annealing for 2 hours at 1250°C. It is apparent that lower doses (Fig. 3.3(a) and (b)) were insufficient to form a continuous SiO_2 layer upon annealing. SiO_2 precipitates in the Si overlayer are evident by a slight decrease in the yield of the random spectra and concurrent increase in yield in the channeled spectra at ~1.0 μm. SiO_2 precipitates are nucleated in regions of both high nuclear energy deposition (~$0.8R_p$) and high O concentration (R_p).[86] If the O dose is sufficiently large, the two layers of precipitates coalesce to yield a single uniform layer.

The χ_{min} in the Si overlayer is remarkably similar for all doses, indicating that the amount of damage (as measurable with RBS/C) after annealing is not significantly dose dependent. The width of the SiO_2 layer, however, increases linearly with O dose. (As will be demonstrated in section 3.1.3, annealing temperatures ≥1300°C can further decrease disorder in the Si overlayer and increase uniformity in the SiO_2 layer.)

3.1.2 Dependence of Damage on Implant Temperature

The dependence of damage on implant temperature is evident both before and after annealing in O-implanted Si. Figure 3.4 shows the RBS/C spectra of O-implanted Si to a dose of 2.18×10^{18} cm^{-2} and an energy of 1.0 MeV for different implant temperatures. The formation of an amorphous region is evident at all temperatures, though the width of the amorphous region increases as the implant temperature decreases. In Fig. 3.4(a) (150°C implant), abrupt dechanneling and direct scattering in the Si overlayer are apparent at depths of ~0.45 μm and ~0.8 μm, respectively, delineating three different regions of damage. Amorphisation has occurred at ~$0.8R_p$ and extends toward the surface while the near-surface region is crystalline, though damaged. Separating these regions is a layer with an intermediate damage level. At 300°C, dechanneling is apparent at ~0.3 μm, i.e. closer to the surface, and a thin well-

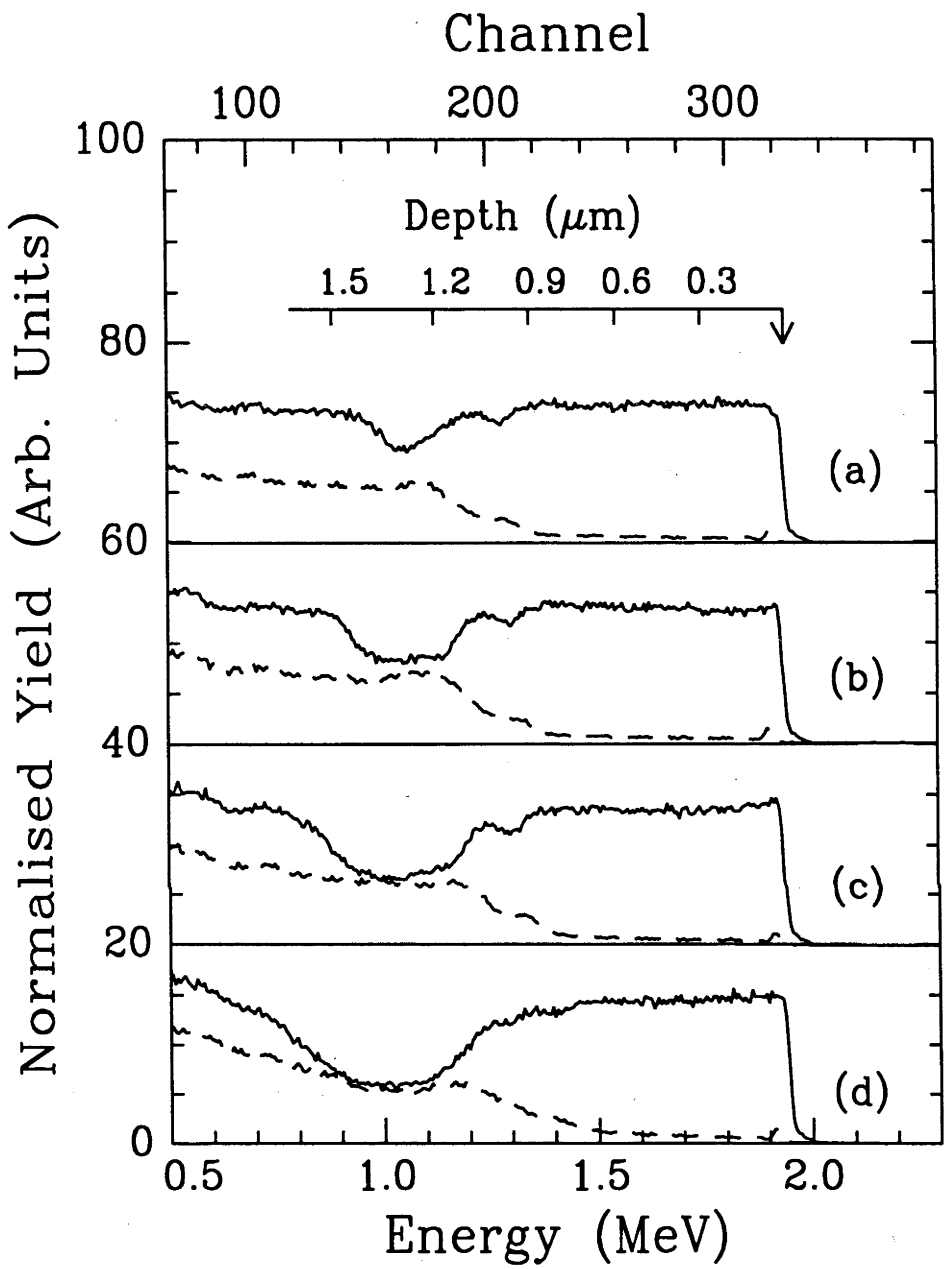

Figure 3.3: RBS/C spectra (obtained with 3 MeV He^+ ions) after annealing (1250°C/2 hours) for a 450°C implant at various O doses: (a) $0.73x10^{18}$, (b) $1.45x10^{18}$, (c) $2.18x10^{18}$ and (d) $2.64x10^{18}$ cm^{-2}. The detector was at a scattering angle of 120°. (—) Random (----) Channeled

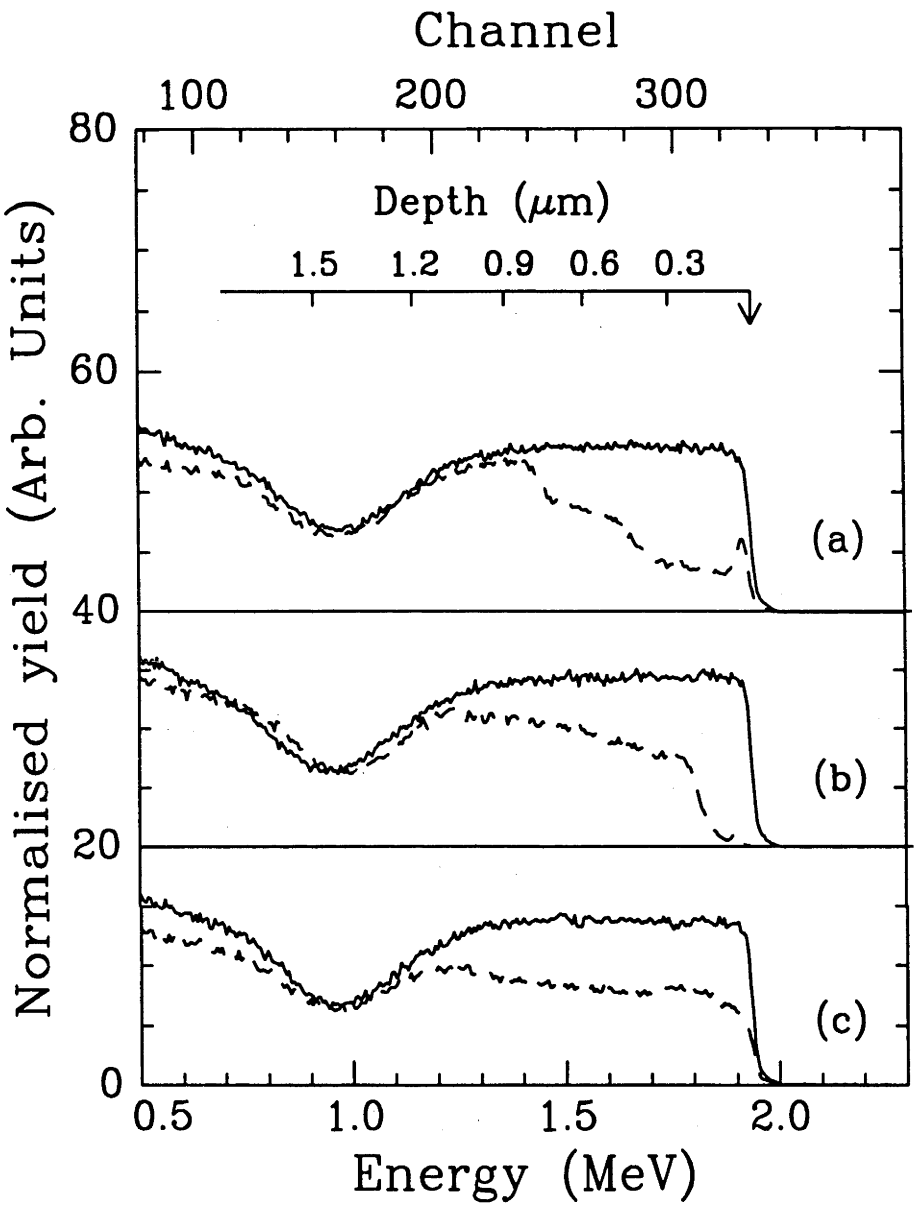

Figure 3.4: RBS/C spectra (obtained with 3 MeV He^+ ions) for a dose of $2.18x10^{18}$ O/cm^2 at various implant temperatures: (a) 150°C, (b) 300 °C and (c) 450 °C. The detector was at a scattering angle of 120°.
(—) Random (----) Channeled

channeled surface region is apparent. At 450°C, significant dechanneling is apparent from disorder at the surface.

XTEM micrographs of these samples are shown in Figure 3.5. In the micrographs, the amorphous regions appear lighter than the crystalline regions. For the lowest implant temperature, the amorphous layer is the widest as noted above. The a/c interface is well defined, i.e. has very sharp interfaces, as consistent with the direct scattering peak at ~0.8 μm evident in the RBS/C spectra. The surface region exhibits two highly damaged areas at depths of 0-0.2 μm and ~0.45-0.8 μm separated by a crystalline region. "Tracks" of damage with an orientation corresponding to the angle of ion implantation are evident within the crystalline region. The columnar damage may be voids stabilised by O gas as previously observed by several groups.[36,37,87] (However, high dose rates and implant temperatures are reportedly necessary conditions for void formation and are contrary to the conditions used in this work.) Finally, a dislocation network bounds the back a/c interface.

In the 300°C O-implanted sample, the amorphous layer is narrower yet still well delineated, although the boundaries are not as sharp as for the 150°C sample. A network of dislocations separating the amorphous layer and a thin crystalline layer at the surface is apparent. The density of the dislocation loops is greatest near the surface and gradually decreases with depth. Further studies (presented in Chapter 4) indicate this damage is the result of relaxation from a strain state produced by an implantation-induced vacancy excess. Once the yield strength of Si is exceeded, strain is relieved through dislocation formation. This damage nucleates at depths consistent with a tensile strain maximum near the middle of the Si overlayer and subsequently increases in width as the O dose is increased. Again, a dislocation network borders the back a/c interface. As expected at this higher implant temperature, less damage (i.e. decreased amorphous layer width and less dense dislocation networks within the Si overlayer) is observed as a result of increased dynamic annealing.

Finally, the defect depth distribution in the 450°C implanted sample appears similar to conventional SIMOX material.[50,88] The amorphous region is no longer clearly delineated. Instead, crystalline platelets are surrounded by amorphous material. Stacking faults are visible at a depth of ~1.1 μm. Due to the higher defect mobility at 450°C, a dislocation network has formed at the surface where there is a high availability of sinks for excess point defects.

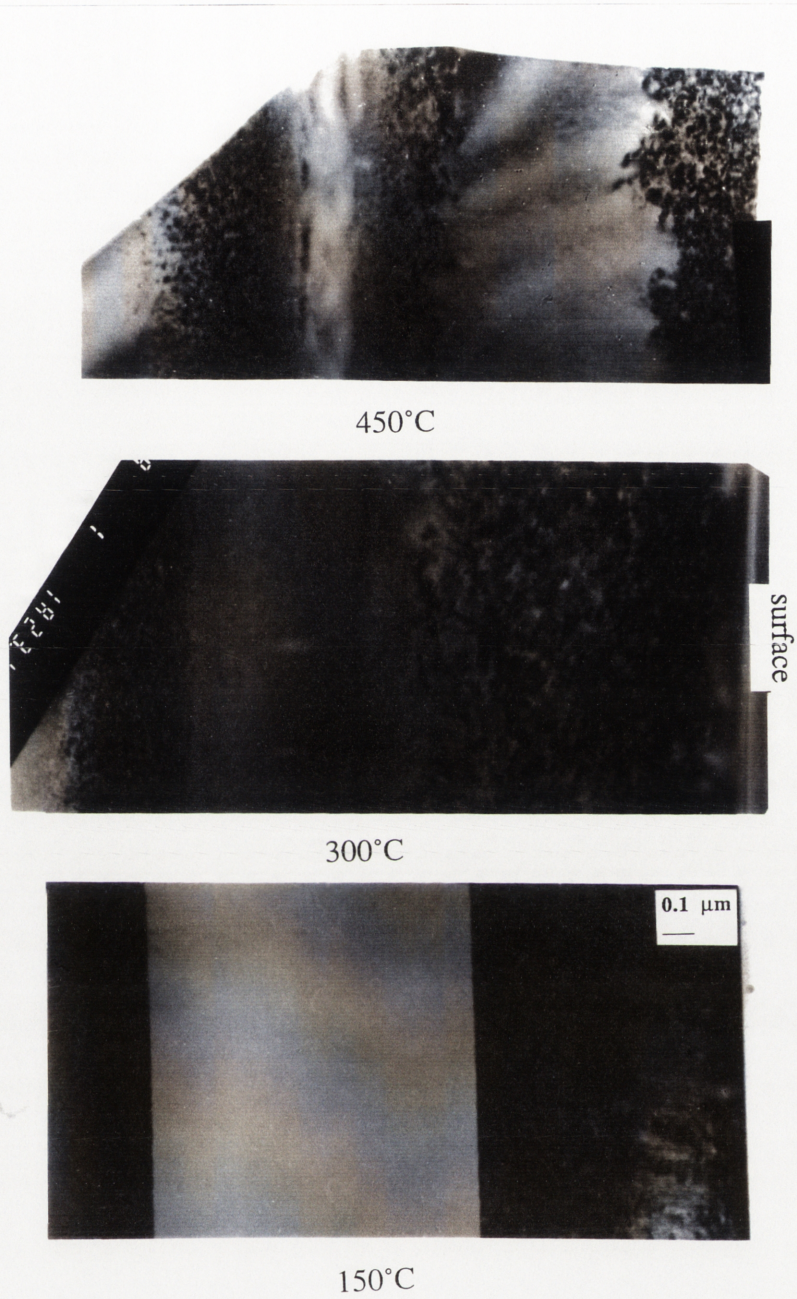

Figure 3.5: XTEM micrographs of O-implanted Si to a dose of $2.18x10^{18}$ cm^{-2} at various implant temperatures.

Figure 3.6 shows RBS/C spectra of 2.18×10^{18} cm^{-2} O-implanted Si at various implant temperatures after a 1250°C/2 hour anneal. In all samples, O segregation towards R_p is evident and the yield in the random spectra at a depth of 1.2-1.5 μm indicates an SiO_2 layer ~4700Å wide has formed. SiO_2 precipitate formation within the Si overlayer is apparent at all implant temperatures by the slight decrease in yield in the random spectra at ~0.9 μm in conjunction with an increase in yield at the same depth for the channeled spectra. The SiO_2 precipitate concentration (as measured by RBS) is greatest at high implant temperatures while the most abrupt Si/SiO_2 interface is evident at the low implant temperature.

In annealed samples, the RBS/C yield near the front Si/SiO_2 interface varies significantly with implant temperature although disorder in the near-surface layer exhibits little implant temperature dependence. (The χ_{min} in the near-surface layer for all samples is ~4%, equivalent to that of virgin Si.) For the sample implanted at a temperature of 150°C, a layer with χ_{min} ~100% at the front Si/SiO_2 interface is consistent with either amorphous Si (unlikely after such high temperature annealing) or randomly oriented polySi. For the 300 and 450°C implants, the χ_{min} at the Si/SiO_2 interface is significantly lower. In addition, Si precipitates in the SiO_2 layer are indicated by an increased yield in the random spectra at a depth of ~1.1 μm (most evident in Fig. 3.6(b)).

VEP Spectroscopy was also performed on these samples. As previously described, the depth distribution of open-volume defects can be measured by changes in the width of the lineshape (as measured by the "W" parameter) of the momentum distribution of γ-rays detected upon positron annihilation at a defect. The W parameter is normalised with respect to the bulk material (W_b), allowing an accurate comparison between samples. Figure 3.7 (a) and (b) show VEP data from a "control" sample of Si (oxidised/annealed but not implanted) and an O-implanted Si (1 MeV, 2.18×10^{18} cm^{-2}, 300°C) sample, respectively. A schematic diagram of the microstructure of the O-implanted Si after a 1250°C/2 hour anneal, as deduced from XTEM measurements, is also included. Note that this sample was not capped with SiO_2 during annealing. The results from the modeling package POSTRAP5 are indicated by solid lines and the experimental data by symbols.[89] From modeling, the depth, number of defects/atom and type of defect (impurity or open-volume) can be deduced. The increase in W/W_b at ~1.0 μm indicates impurity-type defects and is indicative of the buried oxide layer. The other microstructural features evident by XTEM are not apparent in the VEP data because (a) positrons are insensitive to this form of microstructure and/or (b) the distinct features are unresolvable due to the combination of positron diffusion in the solid and the straggle of the positron distribution at large depths.

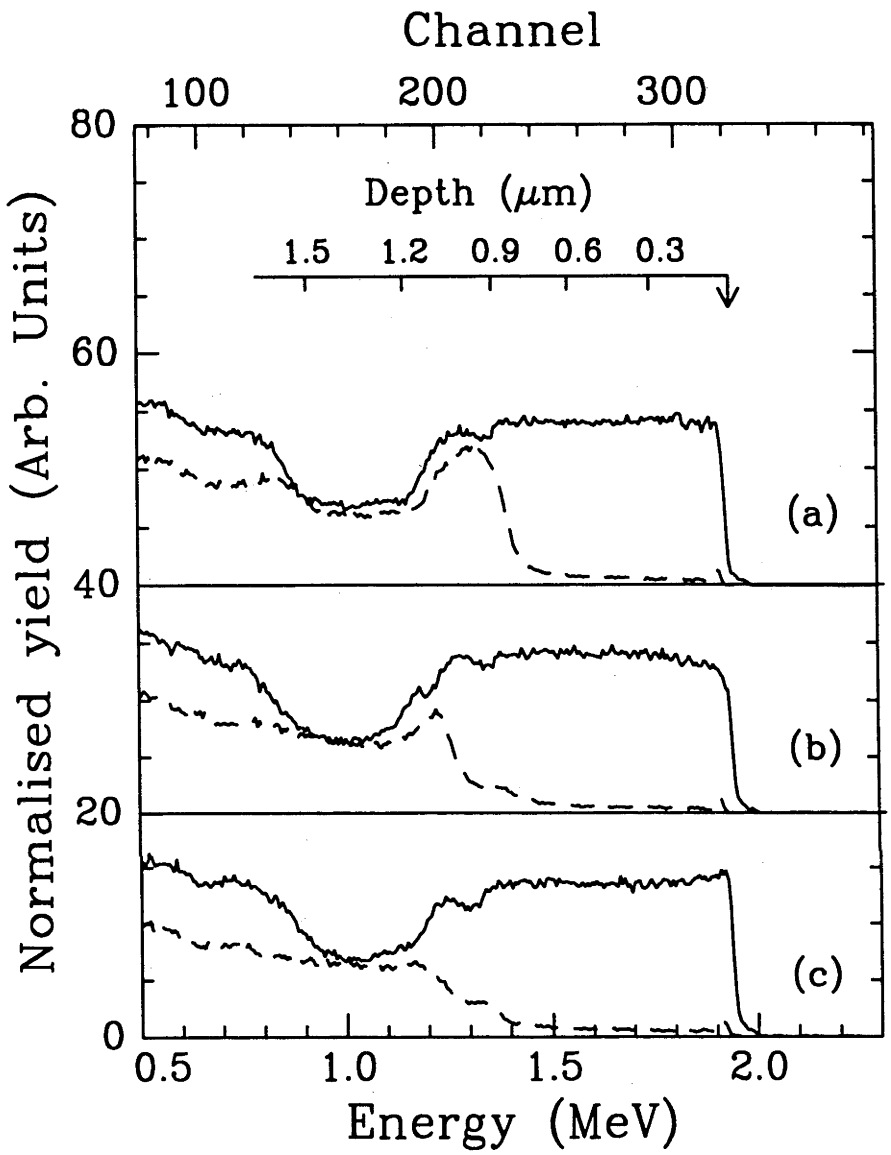

Figure 3.6: RBS/C spectra (obtained with 3 MeV He^+ ions) of Si implanted to a dose of $2.18x10^{18}$ O/cm^2, after a 1250°C anneal, at various implant temperatures: (a) 150°C, (b) 300°C and (c) 450°C. The detector was at a scattering angle of 120°. (—) Random (----) Channeled

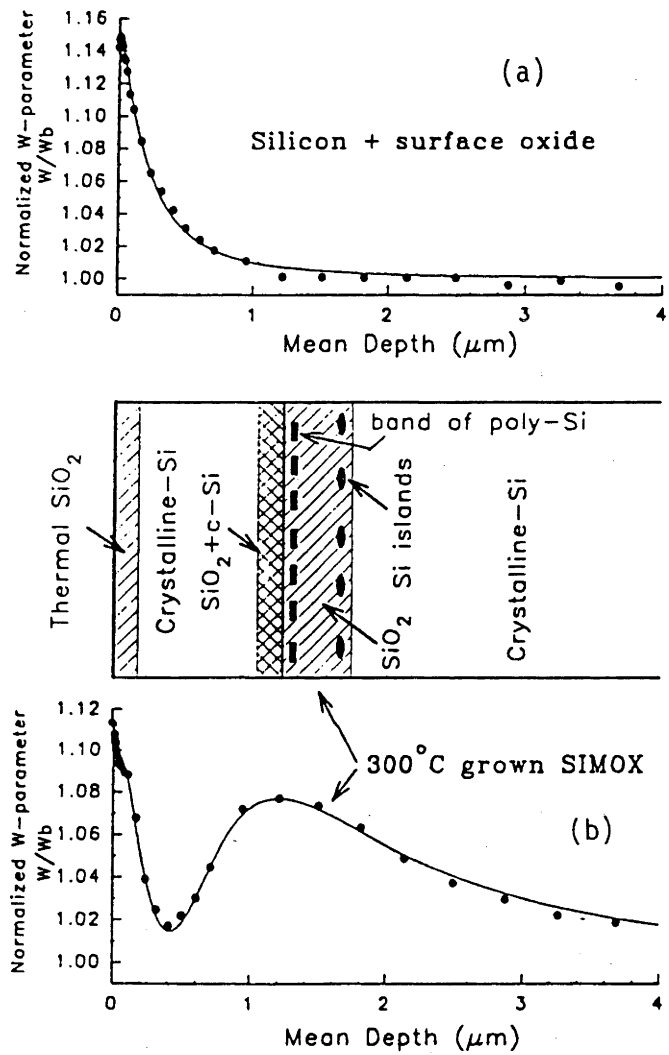

Figure 3.7: VEP data of (a) control Si sample which was oxidised/annealed but not implanted and (b) O-implanted Si (1 MeV, 2.18x10^{18} cm^{-2}, 300°C) after a 1250°C/2 hour anneal. In the centre is a drawing of the O-implanted Si microstructure as determined by XTEM.

Figure 3.8(a) shows VEP data of O-implanted Si (1 MeV, 2.18×10^{18} O/cm^2, various implant temperatures) after annealing (1250°C/2 hours) and removal of the surface oxide. Figure 3.8(b) shows VEP data of the same samples with the Si overlayer removed, to improve the depth resolution in the buried SiO_2 layer. Differences between the 150°C implant relative to the 300 and 450°C implanted samples are apparent. In Fig. 3.8(b), two regions of different W parameters are evident for all implant temperatures indicating the formation of two different SiO_2 "layers" after 1250°C annealing.

Various parameters deduced from modeling of the samples in Fig. 3.8(b) are listed in Table III. (The VEP spectra for samples 4 and 5 are not shown.) It should be noted that the layer 1 and 2 thicknesses of the buried SiO_2 used in the VEP model simulation is particularly wide for the 300 and 450°C implanted samples. This is because layer 2, the deeper layer, of the 300 and 450°C implanted samples is best described as a Si layer in which a great number of SiO_2 precipitates have formed outside the continuous buried SiO_2 layer. Such precipitates were not observable by RBS/C because of their depth. It is evident that in samples 1-3, W/W_b for the shallower layer (layer 1) is less than W/W_b for the deeper layer (layer 2); these values vary most widely in the 300 and 450°C implanted Si. The thickness of these SiO_2 layers is also a function of implant temperature. The W parameters in Table III are normalised to bulk Si. Hence, a value of $W/W_b>1$ indicates a region rich in impurities. For thermally grown oxide, $W/W_b=1.092$. For all of the O-implanted Si samples, layer 1 exhibits a W/W_b parameter similar to that of thermally grown oxide whereas the W/W_b parameter in layer 2 is higher than that of thermally grown oxide. Layer 1 is thickest for the 150°C O-implanted Si indicating that low temperature implantation promotes high-quality oxide formation. However, the number of defects/atom in the Si overlayer (as measured with VEP spectroscopy and shown in Table III) is an order of magnitude greater in the low temperature implanted sample than for samples implanted at higher temperatures.

Figure 3.9 shows XTEM micrographs of these annealed O-implanted Si samples (1 MeV, 2.18×10^{18} cm^{-2}, various implant temperatures). Again, it is apparent that for an implant temperature of 150°C, the nature and depth distribution of disorder is different from that of samples implanted at higher implant temperatures. In the O-implanted Si sample (1 MeV, 2.18×10^{18} cm^{-2}, 150°C), twins border the back Si/SiO_2 interface while polySi borders the front Si/SiO_2 interface. A thin layer of twinned material separates the polycrystalline layer from the single-crystal overlayer. Within the polycrystalline layer, SiO_2 precipitates are not readily discernible although the presence of a low concentration can be inferred from the random RBS spectra of Fig. 3.6. The speckled contrast in the SiO_2 layer is attributable to Si islands, the size of which are considerably smaller than those observed at higher implant temperatures and are consistent with a

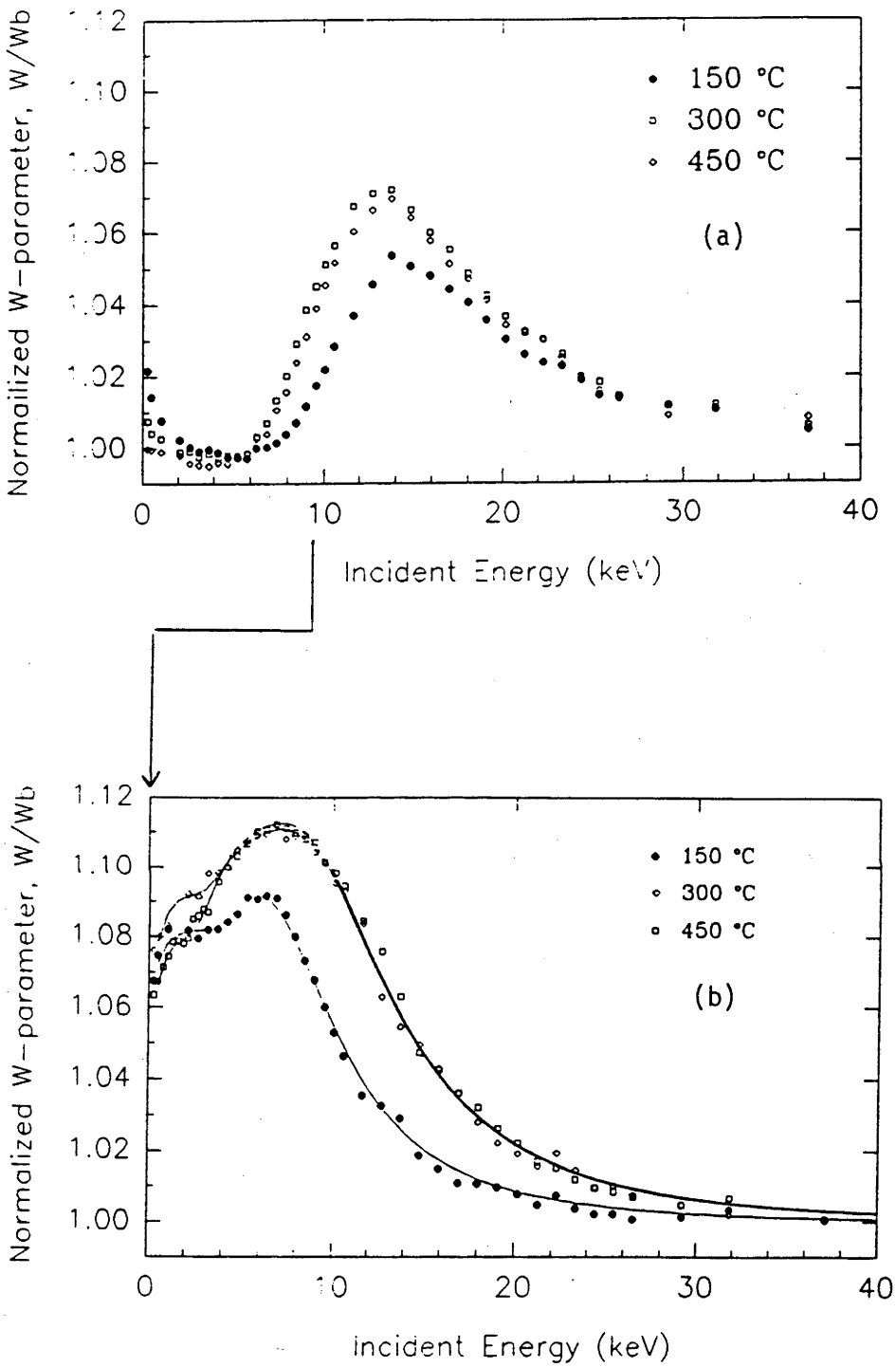

Figure 3.8: VEP data of O-implanted Si (1 MeV, 2.18x10^{18} cm^{-2}, various implant temperatures). (Samples were annealed at 1250°C for 2 hours.) (a) after removal of the surface oxide and (b) after removal of the surface oxide and the Si overlayer.

Sample	O^+ energy (MeV)	Implant/ Anneal Temperature	Silicon Overlayer		Buried Oxide			
			Depth (Å)	Defect ($atom^{-1}$	Thickness (Å)		W/W_B	
					Layer 1	Layer 2	Layer 1	Layer 2
1	1.0	150/1250	10,000	$5x10^{-5}$	3,000	3,000	1.080	1.090
2	1.0	300/1250	9,500	$5x10^{-6}$	1,500	9,000	1.090	1.116
3	1.0	450/1250	9,500	$5x10^{-6}$	2,000	8,500	1.078	1.116
4	1.0	150/1350	12,000	$5x10^{-5}$	4,800		1.086	
5	0.2	600/1350	1,200	$5x10^{-5}$	4,500		1.082	

SiO_2/Si:

1250 Å of thermally grown oxide	W/W_B: 1.092

Table III: VEP parameters deduced from modeling are listed for various SIMOX and thermally grown SiO_2/Si samples. Layer 1 is the shallower layer.

more homogeneous SiO_2 layer. Also, threading dislocations between the surface and the polycrystalline layer were apparent, though are not shown in this micrograph.

In the O-implanted Si sample (1 MeV, $2.18x10^{18}$ cm^{-2}, 300°C), SiO_2 precipitates in the Si overlayer and Si islands within the SiO_2 layer are visible. In contrast to the 150°C implanted sample, the Si islands are not distributed throughout the SiO_2 layer, but rather there is a band of Si precipitates near both Si/SiO_2 interfaces. Threading dislocations emanate from many of the SiO_2 precipitates within the Si overlayer and extend toward the buried SiO_2 layer, possibly as a mechanism of stress relief.

Finally, in the O-implanted Si sample (1 MeV, $2.18x10^{18}$ cm^{-2}, 450°C), there are a greater number of Si islands distributed throughout the SiO_2 layer. These islands are elongated and oriented parallel to the Si/SiO_2 interfaces. The SiO_2 precipitates within the Si overlayer are again located near the front Si/SiO_2 interface but are spatially confined to within ~0.15 μm of the SiO_2 layer and are apparent in greater concentration. Threading dislocations emanating from these SiO_2 precipitates were not observed.

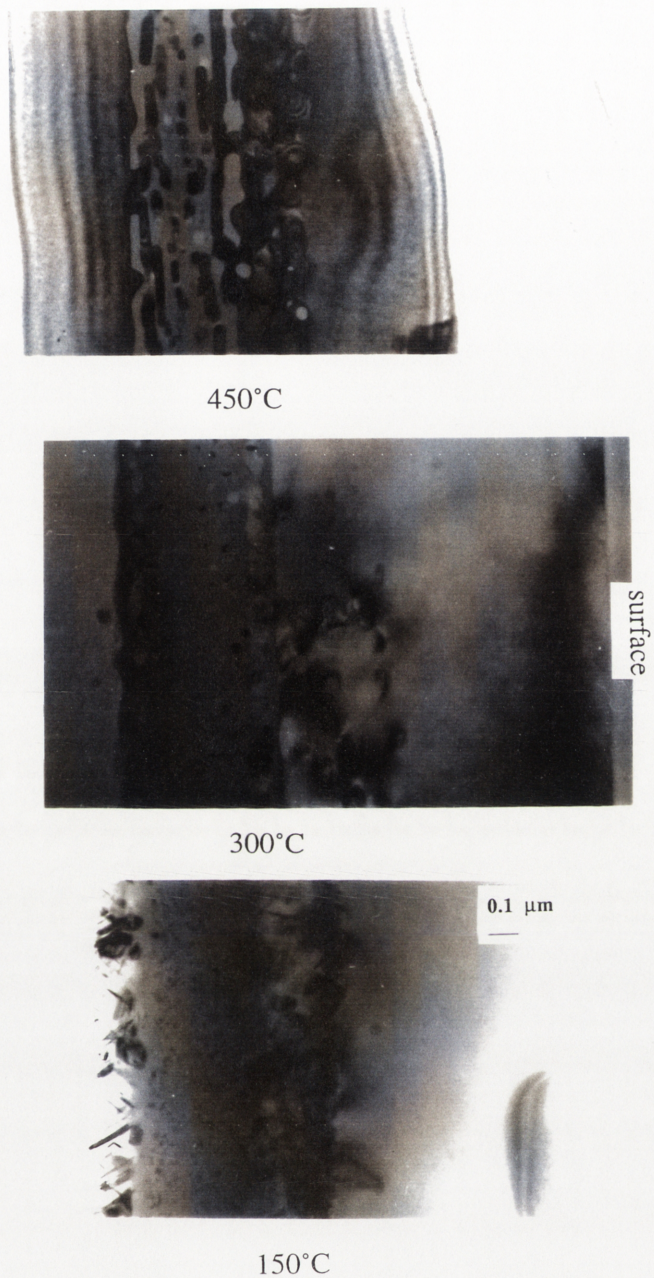

Figure 3.9: XTEM micrographs of O-implanted Si (1 MeV, 2.18x10^{18} cm^{-2}, various implant temperatures) after a 1250°C/2 hour anneal

3.1.3 Anneal Temperature and Time Dependence

In 1985, the benefits of high temperature annealing were realised; it was shown that annealing at ≥1300°C resulted in the complete dissolution of the SiO_2 precipitates within the Si overlayer and a more abrupt Si/SiO_2 interface.[90,91] In addition, the electrical properties of the SIMOX material were improved.[92-94] Previously, the standard annealing temperature had been ~1150°C and the resultant material was of poor quality with a dislocation density of ~10^9 cm^{-2}.

The free energy of the O-implanted Si system is given by:[95]

$$\Delta G = \frac{4}{3}\pi r^3 \Delta G_V + 4\pi r^2 \sigma + \text{elastic energy} \qquad (3.1)$$

where ΔG_V = change in the free energy per unit volume associated with the creation of the SiO_2 phase.

σ = Si/SiO_2 interfacial energy per unit surface area

r = radius of (spherical) precipitates.

To fabricate a uniform buried SiO_2 layer, the critical radius r_c should be as large as possible. (A description of r_c was previously given in Section 1.2.4.) Figure 3.10 is a plot of free energy versus precipitate radius. It is evident that r_c increases as T increases (or as $(T-T_E)$ decreases). As a consequence, large precipitates can only be dissolved at high temperatures. It has been shown that dissolution of all precipitates requires 30 minutes at 1405°C or 4 hours at 1300°C.[96]

RBS/C spectra of O-implanted Si (1 MeV, 2.15x10^{18} cm^{-2}, 300°C) are shown in Figure 3.11. All samples were annealed in a 2% O in Ar atmosphere for 2 hours at (a) 1250°C, (b) 1300°C and (c) 1350°C. A decrease in the Si and SiO_2 precipitate concentration in the SiO_2 and Si layers, respectively, is evident with increasing anneal temperature This is indicated by the changes in the RBS/C yield at depths of ~1.45 and ~1.1 μm, respectively. At an anneal temperature of 1350°C, no precipitates were evident in the RBS/C spectra. Finally, the front Si/SiO_2 interface becomes more abrupt as the anneal temperature is increased.

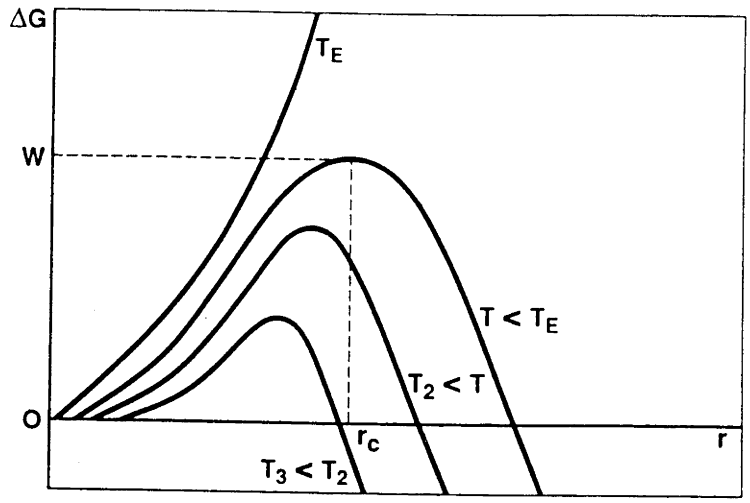

Fig. 6 Variation of ΔG as a function of precipitates radius

Figure 3.10: Variation of ΔG as a function of precipitate radius. T is an arbitrary temperature where $T_E > T > T_2 > T_3$.[90]

VEP spectroscopy was performed on O-implanted Si (1 MeV, 2.18×10^{18} cm^{-2}, 150°C) that was annealed at 1350°C for 2 hours. Figure 3.12 show VEP data (a) before Si overlayer removal and (b) after Si overlayer removal. When compared to the sample implanted under the same conditions but annealed at 1250°C (Fig. 3.8), differences are apparent. The two layer structure evident at the low annealing temperature has been replaced by a single layer with $W/W_b \sim 1.08$; this W/W_b parameter is comparable to that of a thermal oxide. Although the number of defects/atom in the Si overlayer is unchanged, the higher annealing temperature dramatically improved the buried SiO_2 homogeneity. For comparison, Table III also lists the VEP spectroscopy results from O-implanted Si (0.2 MeV, 1.4×10^{18} cm^{-2}, 600°C) which was obtained from a commercial SIMOX manufacturer. The extracted number of defects/atom within the Si overlayer and the W/W_b parameter is comparable to that of the annealed low temperature O-implanted Si (1 MeV, 2.18×10^{18} cm^{-2}, 150°C).

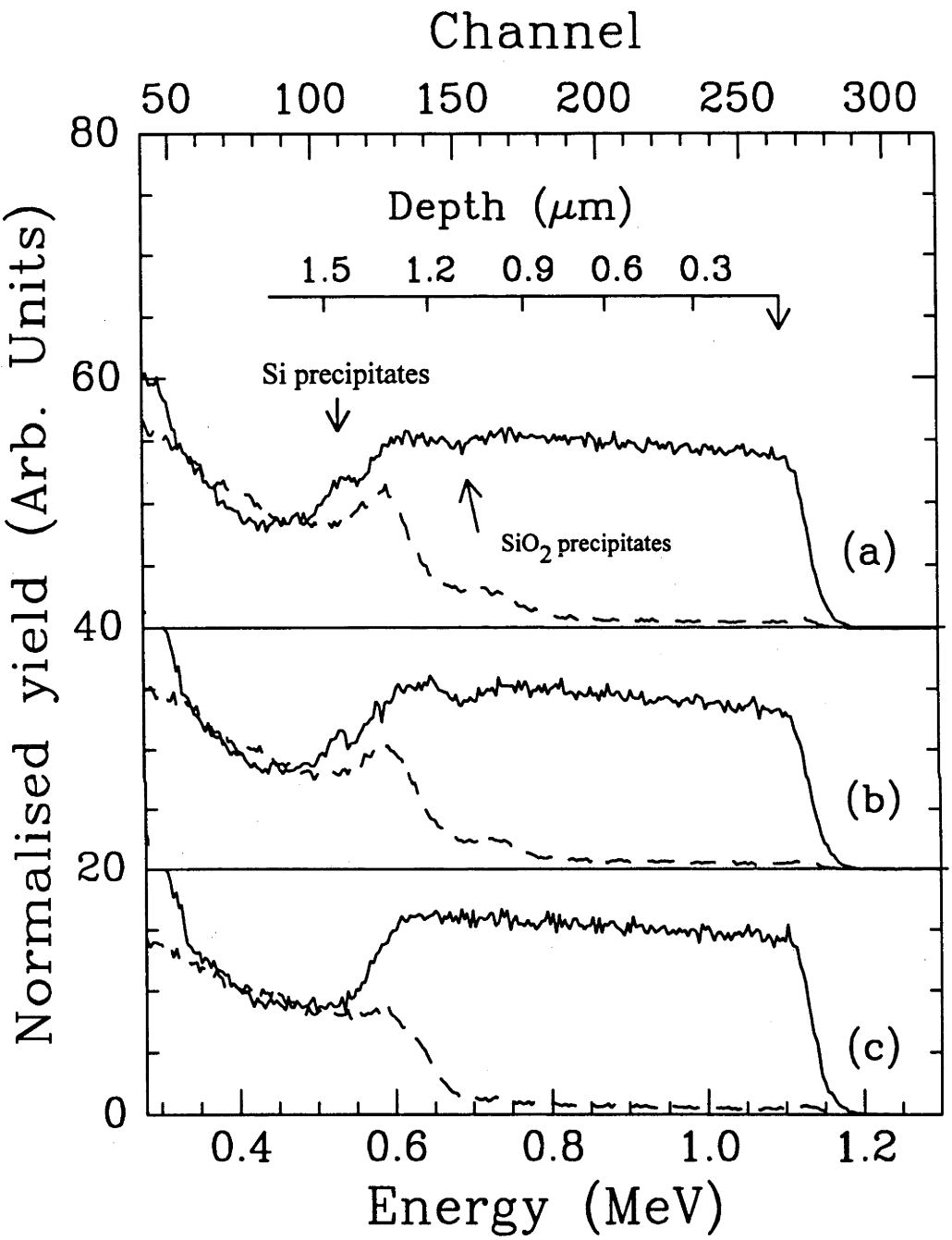

Figure 3.11: RBS/C spectra of O-implanted Si (1 MeV, 2.18x10^{18} O/cm^2, 300°C) after annealing for 2 hours at: (a) 1250°C, (b) 1300°C and (c) 1350°C

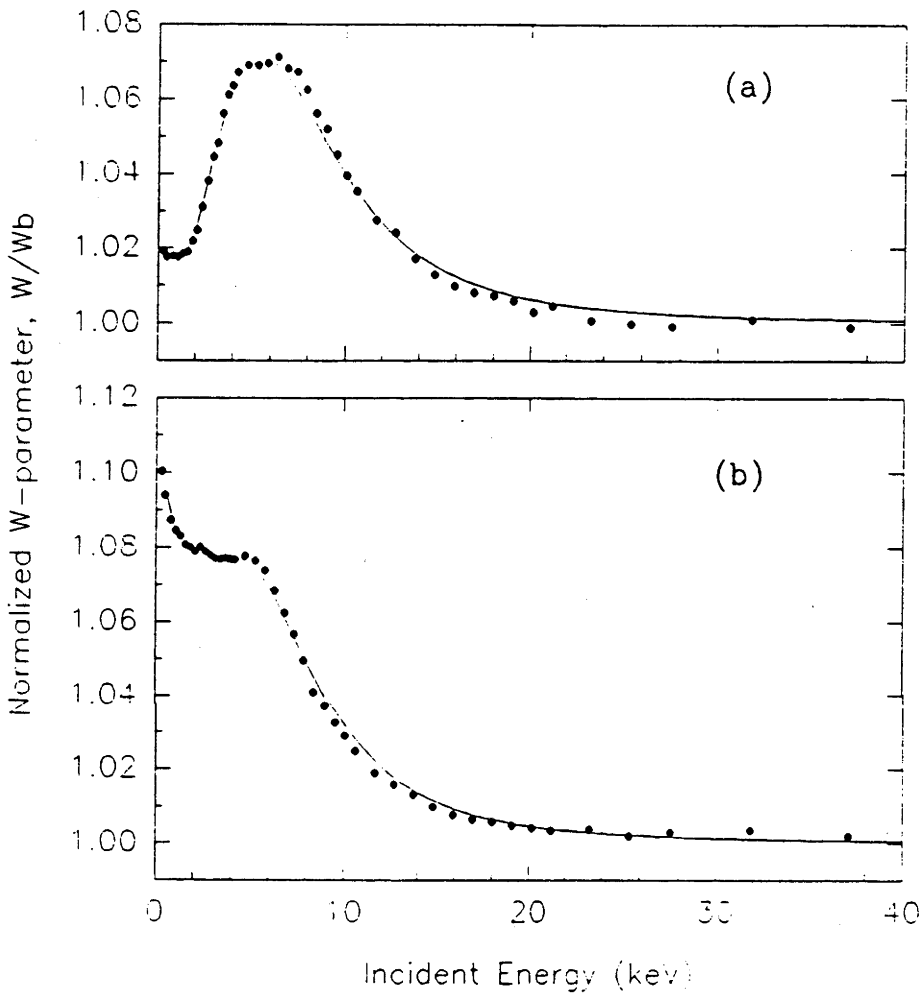

Figure 3.12: VEP data for O-implanted Si (1 MeV, 2.18x10^{18} O/cm^2, 150°C) after annealing for 2 hours at 1350°C (a) after removal of the surface oxide and (b) after removal of the surface oxide and the Si overlayer.

3.1.4 Discussion

The final defect structure in the annealed SIMOX results from (1) the level of dynamic annealing that occurs during implantation and (2) the temperature of the post-implantation anneal. (As discussed in more detail in Chapter 4, the O dose significantly affects the damage within the Si overlayer of unannealed O-implanted Si between 1.45 and 2.18×10^{18} cm^{-2} for a 450°C implant temperature. However, outside this dose range, increases in dose do not significantly increase the damage.) During implantation, the interaction of implantation-induced point defects and dislocations as well as the formation of SiO_2 precipitates is influenced by the level of dynamic annealing. For example, at higher implant temperatures (300 and 450°C), O segregates into SiO_2 precipitates during implantation. As the SiO_2 precipitates grow, they impede the movement of interstitial Si, blocking ejected Si interstitials from diffusing to sinks and/or annihilation sites. This effect is enhanced as the implant temperature is increased. The amount of point defect recombination and/or annihilation during implantation significantly influences the damage within the Si overlayer. The increased point defect mobilities at higher implant temperatures result in lower concentrations of point defects. As will be described in further detail in Chapter 4, point defects can cause strain within the Si overlayer and lead to dislocation formation when the yield strength of Si is exceeded.

The damage microstructure after implantation also influences the recrystallisation of the implantation-induced amorphous Si during the post-implantation anneal. Recrystallisation of the amorphised Si can proceed in two ways: via solid phase epitaxy (SPE) or random nucleation and growth (RNG). SPE is a layer by layer epitaxial regrowth of amorphous regions whereas RNG involves the nucleation of Si crystallites that grow and eventually coalesce with other Si crystals in surrounding areas yielding polySi. These two processes have different activation energies, with RNG having the larger of the two and thus, becoming more important at high temperatures.[97] The competition between SPE and RNG is also a strong function of impurity level. In particular, O retards the rate of SPE[24] and enhances RNG.[97] As the temperature is increased during annealing, crystalline material at the a/c interface acts as a seed for SPE of amorphised O-rich Si. As recrystallisation proceeds and the O concentration at the a/c interface increases, SPE is retarded with a probable concomitant loss of interface planarity and subsequent twin formation. (The SPE process is assumed to be complete prior to O segregation.) Simultaneously, O-rich amorphous material bordered by the buried SiO_2 layer and the a/c interface may recrystallise via RNG yielding polySi.

In the low implant temperature O-implanted Si (1 MeV, 2.18×10^{18} cm^{-2}, 150°C), twinning was evident at the back Si/SiO_2 interface and a polySi/twinned layer formed at

the front interface. This defect structure is similar to the O-implanted Si (5 MeV, $2x10^{18}$ cm^{-2}, -197°C) reported by Nieh, et al.[82] As the SPE regrowth of the amorphous Si proceeds, the recrystallisation front advances toward R_p and hence, a higher O concentration. Eventually, a region with an O concentration high enough to inhibit SPE and/or enhance RNG is reached. As a result, regrowth of the heavily oxygenated Si overlayer no longer proceeds uniformly and twinning results. The polySi evident at the front Si/SiO_2 interface is a result of the RNG process.

In samples implanted at higher temperatures (300 and 450°C), SiO_2 precipitates which form during implantation impede the formation of a uniform buried oxide. During post-implantation annealing, excess Si becomes trapped within the SiO_2 layer and large Si precipitates form resulting in a less uniform SiO_2 layer. This was evident in XTEM micrographs of Fig. 3.9. In addition, SiO_2 precipitate formation during implantation in regions adjacent to the buried SiO_2 layer was observed. These precipitates must be dissolved by the final annealing step to free O for migration to, and subsequent encorporation in, the buried SiO_2 layer. As demonstrated, a post-implantation anneal of $\geq$1350°C is necessary to free the Si overlayer of SiO_2 precipitates.

3.2 High-Energy Si-ion Implantation

Pre-anneal disorder in Si-implanted Si was compared with O-implanted Si to elucidate the mechanisms of defect formation during SIMOX substrate fabrication. As previously stated, typical defects in SIMOX substrates include SiO_2 precipitates, microtwins, stacking faults and dislocations. Dislocations can be generated via several nucleation processes including: 1) agglomeration of point defects 2) surface disorder and/or 3) precipitates of a second phase.[98] In the high-dose, high temperature regime of SIMOX substrate fabrication, all three nucleation processes must be considered. By comparing high-dose O and Si ion implantation, the relative contribution of the individual nucleation mechanisms can be examined. Equivalently, the relative influence of irradiation-induced atomic displacements and high O concentrations can be differentiated.

3.2.1 Experimental Results

Figure 3.13 shows TRIM90 simulated range and vacancy distributions for 1 MeV Si- and O-implanted Si at doses of 0.8×10^{18} cm^{-2} and 2.18×10^{18} cm^{-2}, respectively. Due to the mass and stopping power of Si as compared to O, a Si dose of 0.8×10^{18} cm^{-2} yields a similar areal vacancy density within the Si overlayer (0 to 1.0 μm) as that resulting from an O implant to a dose of 2.18×10^{18} cm^{-2}. These doses were chosen in order to compare the damage which results from these two implants within the Si overlayer. An energy of 1 MeV results in a comparable R_p for O and Si implantation though the peak atom concentration is lower for the Si implant given the lesser dose and greater straggle. Si substrates were implanted at 1 MeV to 0.8×10^{18} Si/cm^2 at 300 and 450°C, while at 150°C, implantation to 0.7×10^{18} Si/cm^2 was performed. The Si dose rate was 2.3×10^{13} $ions/cm^2$-sec. The comparable study for O-implanted Si was performed at a dose rate of 3.3×10^{13} $ions/cm^2$-sec. (RBS/C spectra were shown in Fig. 3.4)

Figure 3.14 is the RBS/C spectra of Si-implanted Si. The effect of implant temperature on dechanneling is slight for Si-implanted Si, but is nevertheless evident. As for O implantation, the 300°C sample appears to have a thin crystalline layer in the near-surface region. At greater depths (~0.6-0.9 μm), a slight increase in the channeled yield for samples implanted at 300 and 450°C as compared to 150°C is apparent.

The nature of disorder is apparent from the XTEM micrographs shown in Figure 3.15. Within the bulk of Si-implanted Si, amorphisation has not occurred at any implant temperature. Dislocations are evident near R_p for all implant temperatures and this is consistent with depths of large nuclear energy deposition density. Such dislocations are formed by the agglomeration of point defects. (For the O-implanted samples, the stress associated with SiO_2 precipitation will also contribute to dislocation formation.) The dislocation depth distribution is quite similar for the 150 and 300°C O- and Si-implanted samples, but the 450°C samples show some dissimilarities. Si-implanted Si at 450°C exhibits dislocation formation extending from the bulk to the surface while a dislocation-free region is apparent at intermediate depths in O-implanted Si. For both O- and Si-implanted samples, a thin dislocation-free surface layer is evident at the intermediate implant temperature (300°C) while a dislocation network at the sample surface and near R_p is common to both samples implanted at 150°C.

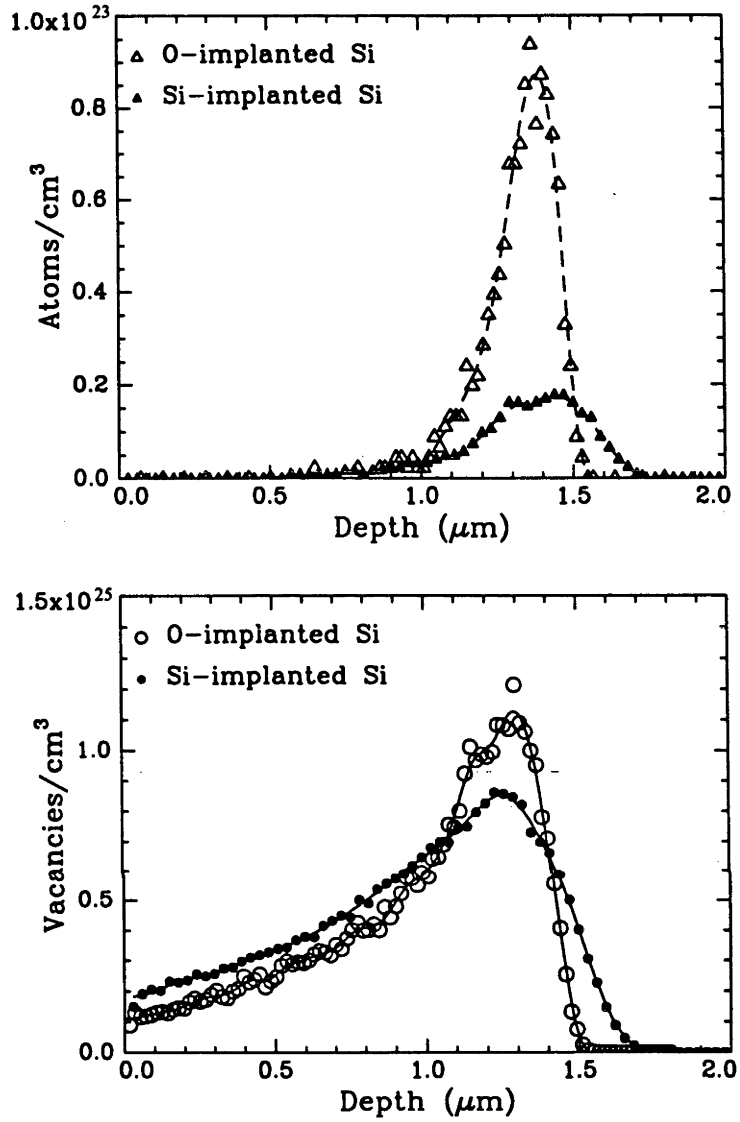

Figure 3.13: Range and vacancy distributions as simulated by TRIM90 for O- and Si-implanted Si at 1.0 MeV to doses of $2.18x10^{18}$ O/cm^2 and $0.8x10^{18}$ Si/cm^2, respectively.

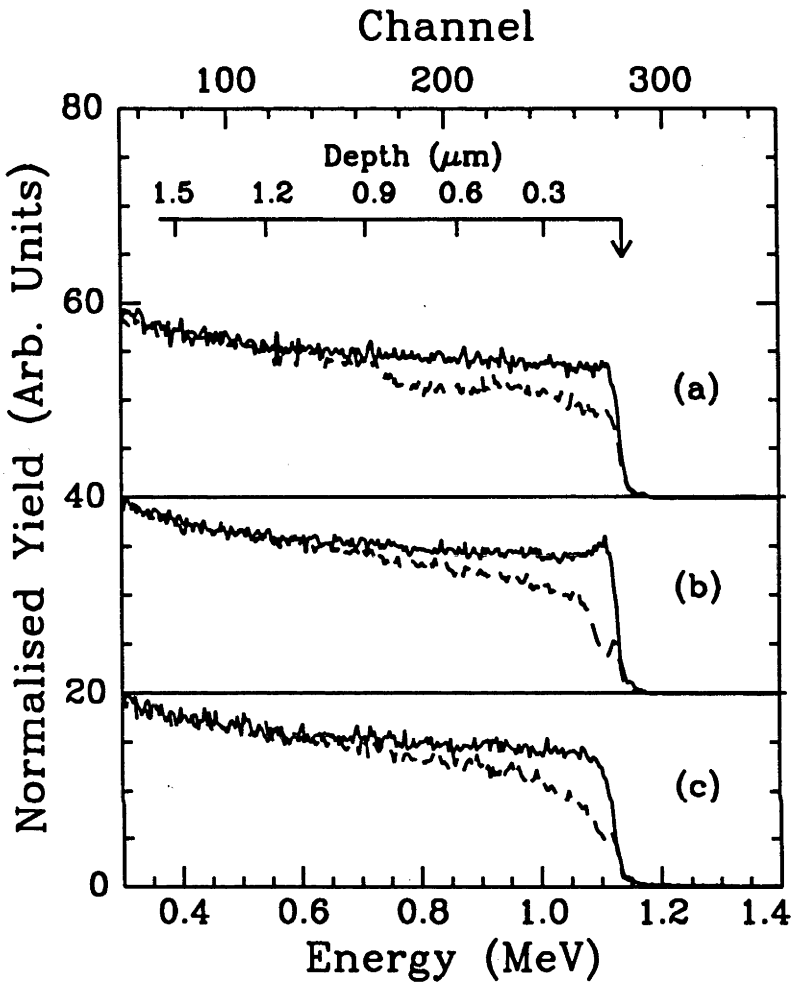

Figure 3.14: RBS/C spectra (obtained with 2 MeV He^+ ions) for a dose of (a) $0.7x10^{18}$ Si/cm^2 at an implant temperature of 150°C and at a dose of $0.8x10^{18}$ Si/cm^2 at an implant temperature of (b) 300°C and (c)450°C. (——) Random (-----) Channeled.

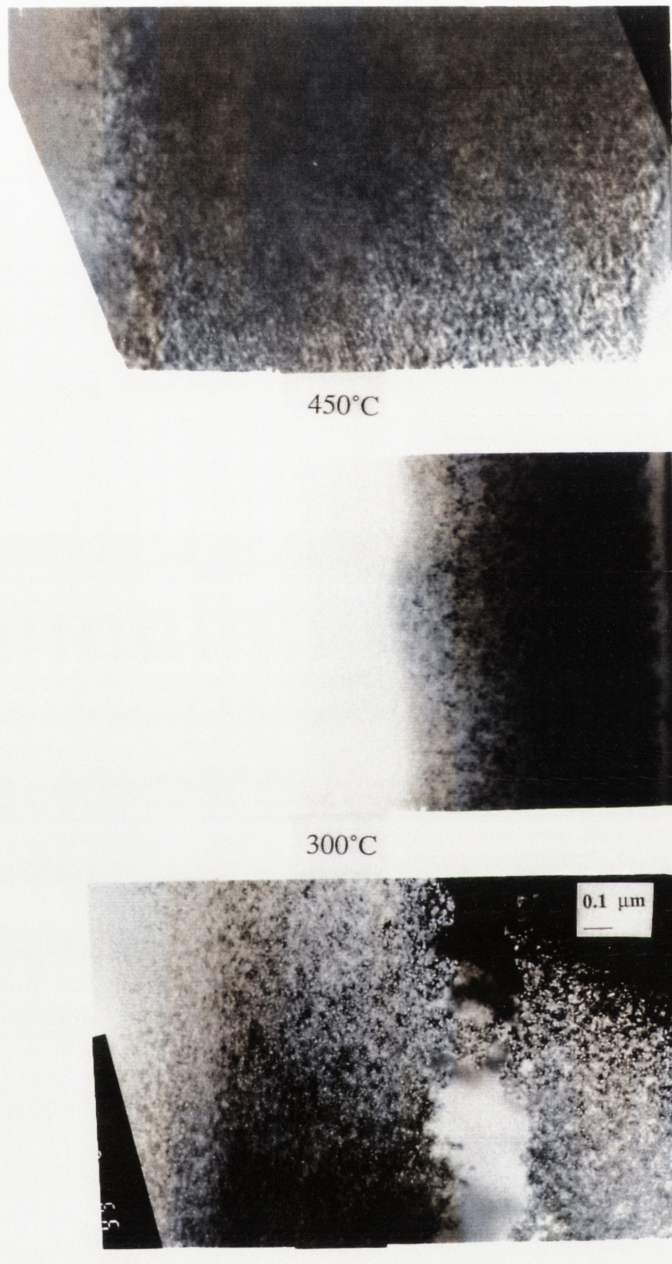

Figure 3.15: XTEM micrographs of (1 MeV, $0.7x10^{18}$ cm^{-2}, 150°C) and (1 MeV, $0.8x10^{18}$ cm^{-2}, 300 and 450°C) Si-implanted Si.

3.2.2 Discussion

As noted previously, amorphous layer formation was not evident in the Si-implanted Si at any implant temperature. In comparison, amorphous layer formation in O-implanted Si was evident at doses $\geq 0.73 \times 10^{18}$ O/cm^2 at implant temperatures of 150-450°C. This demonstrates the influence of impurities on amorphisation. For the O-implanted samples it is evident that both irradiation-induced atomic displacements and the high oxygen impurity concentration contribute to amorphous layer formation. While the O impurity concentration is independent of temperature, the displaced atoms' relative contribution to amorphous layer formation decreases as implant temperature, and hence in-situ dynamic annealing, increases. Consequently, in the O-implanted Si samples described in section 3.1.2, the width of the amorphous layer decreases with increasing implant temperature. (In O-implanted Si at an implant temperature of 450°C, crystalline platelets were evident within the amorphous material.)

In contrast, damage profiles within the Si overlayer were quite similar in the O- and Si-implanted samples. The dislocation network evident at the surface in samples implanted at 150°C is similar to recent observations of surface amorphisation during MeV implantation as reported by Goldberg[99] and Lohner, et al.[100] While the surface is a sink for point defects, complete defect annihilation is not achieved at implant temperatures of 150°C and defect agglomeration yielding dislocation formation results. Recoiled surface oxide atoms and/or contaminants may also enhance this effect. (Dislocation nucleation via surface contamination is inconsistent with the observed implant temperature dependence.) The similarities of damage within the Si overlayer, between O- and Si-implanted Si infer that atomic displacements are the most significant parameter in determining the damage profile of this region. In general, it was apparent from samples implanted with lesser O and Si doses that dislocation formation within the Si overlayer in unannealed samples was non-linear with ion dose (see Chapter 4 for further details), i.e. dislocation formation was observed when a critical areal vacancy density ($\geq 2 \times 10^{21}$ vacancies/cm^2 at an implant temperature of 300°C) was exceeded. This parameter is temperature dependent as both in-situ dynamic annealing and defect mobility increase with implant temperature.

Finally, the large concentrations of O introduced during O-implantation in Si affects the thermal stability of implantation-induced defects. After the annealing of the Si-implanted Si (1 MeV, 0.8×10^{18} cm^{-2}, 150-450°C) at 1250°C for 2 hours, RBS/C measurements indicated no damage was present at depths up 1.5 μm. Thus, in the absence of SiO_2 precipitates, interstitial O (which can pin dislocations) and an amorphous layer, defects that have formed during the Si implantation can and do anneal out.

3.3 Conclusions

The fabrication of SIMOX material by MeV O-ion implantation was investigated and found to be similar to "conventional" SIMOX material implanted at low (~200 keV) ion energies. The importance of the implant temperature, and hence dynamic annealing, in determining the defect microstructure and depth distribution before and after annealing was established. The formation of SIMOX material at a temperature as low as 150°C without total amorphisation of the Si overlayer was demonstrated; the lower atom mobility inherent with low temperature implantation impedes SiO_2 precipitate formation in regions away from R_p. Consequently, low implant temperature implantation resulted in a more homogeneous buried SiO_2 layer and a lower SiO_2 precipitate concentration within the Si overlayer after annealing.

MeV O-ion implantation performed at higher implant temperatures (300 and 450°C) produced a similar microstructure to that of low-energy, high implant temperature SIMOX, i.e. Si and SiO_2 precipitates in the buried SiO_2 layer and Si overlayer, respectively, were evident. Characterisation by VEP spectroscopy showed the number of defects/atom were lower in this material than for in the 150°C O implantation, but that lower implant temperatures promoted SiO_2 formation of a quality comparable to thermally grown SiO_2.

The implant dose was also shown to affect the amount of damage within the Si overlayer in unannealed O-implanted Si. Specifically, a significant increase in damage with dose, over a dose range specific to each implant temperature studied, was evident. At doses above or below this range, a minimal increase in damage with dose was observed. This behaviour is significant in exploring the mechanisms of damage formation within the Si overlayer after high-dose implantation and is further explored in Chapter 4.

The ability to fabricate SIMOX material by MeV implantation ((1) by virtue of the lower nuclear energy deposition throughout the Si overlayer and (2) the extended implant temperature range available for implantation) lends itself to a single implant and anneal process whereby low defect density SIMOX material can be produced. As well, the thicker Si overlayer which results from high-energy implantation may be useful for novel device designs such as 3D circuits.

Comparisons of O- and Si-implanted Si at various implant temperatures were performed at energies and doses yielding similar vacancy concentrations within the Si overlayer. Over the energy and temperature range studied, amorphous layer formation was not evident in any Si-implanted Si whereas in O-implanted Si (under similar implant conditions) amorphisation was apparent. Thus, the contribution of both atomic displacements and high O concentrations to amorphous layer formation was established.

Defect formation within the Si overlayer (i.e. at depths less than R_p) was similar in O- and Si-implanted Si over the implant temperature range studied (150-450°C), indicating that the mechanisms of defect formation in this region are a result of the implantation process rather than a chemical effect. The mechanisms of defect formation within the Si overlayer after high-dose implantation are further examined in Chapter 4.

Chapter 4

Damage and Strain Accumulation in O- and Si-implanted Si

4.0 Introduction

A vast amount of research has been devoted to reducing defect densities within the Si overlayer of SIMOX material.[19,30-31,35,39-41,43,45-47] The importance of a final high-temperature anneal to dissolve Si and SiO_2 precipitates, as well as reducing the threading dislocation density, has been well established.[90,91] However, if threading dislocations form during implantation, they cannot be completely eliminated during the post-implantation anneal.[35] Consequently, recent work has focused on preventing dislocation formation during implantation. However, since the atomistic mechanisms for dislocation formation are still under study, design of the implantation process to form high-quality SIMOX material is continually evolving. Various techniques of reducing defect densities within the Si overlayer were discussed in Section 1.3. At present, the two most common approaches are: 1) prevention of dislocation loop

nucleation during implantation and 2) impeding the propagation of dislocation loops towards the surface where they become threading dislocations.

In this chapter, the role of point defects and point defect clustering in high-dose, high-energy ion-implanted Si is investigated. The extended range inherent to high-energy implantation is well suited for studying damage within both the Si overlayer and at R_p given the large spatial separation between these two regions. Studies of strain in high dose O- and Si-implanted Si as a function of implant dose and implant temperature will be presented. Dislocation formation in the overlayer is shown to be distinct from end-of-range damage and a correlation between tensile lattice strain and dislocation formation within the Si overlayer is established. Through XTEM characterisation in conjunction with DCXRD, tensile strain in unannealed, ion-implanted Si is shown to result from an implantation-induced vacancy excess within the Si overlayer.

4.1 Strain in O- and Si-implanted Si

4.1.1 O-implanted Si

(100) Si was implanted with 1 MeV O ions at 150°C to various doses between 0.3-2.15x10^{18} cm^{-2}. Implantation was performed at a dose rate and current density of 11.8x10^{13} ions/cm^2-sec and 19 μA/cm^2, respectively. The samples were clamped to the target holder and no conductive Ag paint was used. As a result, the temperature rise due to the incident ion beam power is expected to be significant. As previously described in section 2.1.1, the actual implant temperature is estimated to be between 225 and 300°C. Figure 4.1 shows the random and channeled RBS/C spectra for doses ≤1.3x10^{18} cm^{-2}. Amorphous layer formation near R_p (~1.3 μm) is not apparent at doses of < 0.7x10^{18} cm^{-2}. At greater doses, significant increases in the amorphous layer width are evident with increasing dose. Up to a dose of 1.0x10^{18} cm^{-2}, the χ_{min} over the extent of the Si overlayer is low (approximately that of virgin Si). However, at a dose of 1.3x10^{18} cm^{-2}, damage formation (as evident by an increased χ_{min} at ~0.5 μm) is apparent within the Si overlayer. Unlike the end-of-range damage at ~1.2 μm, the onset of disorder within the Si overlayer is evidently non-linear with dose.

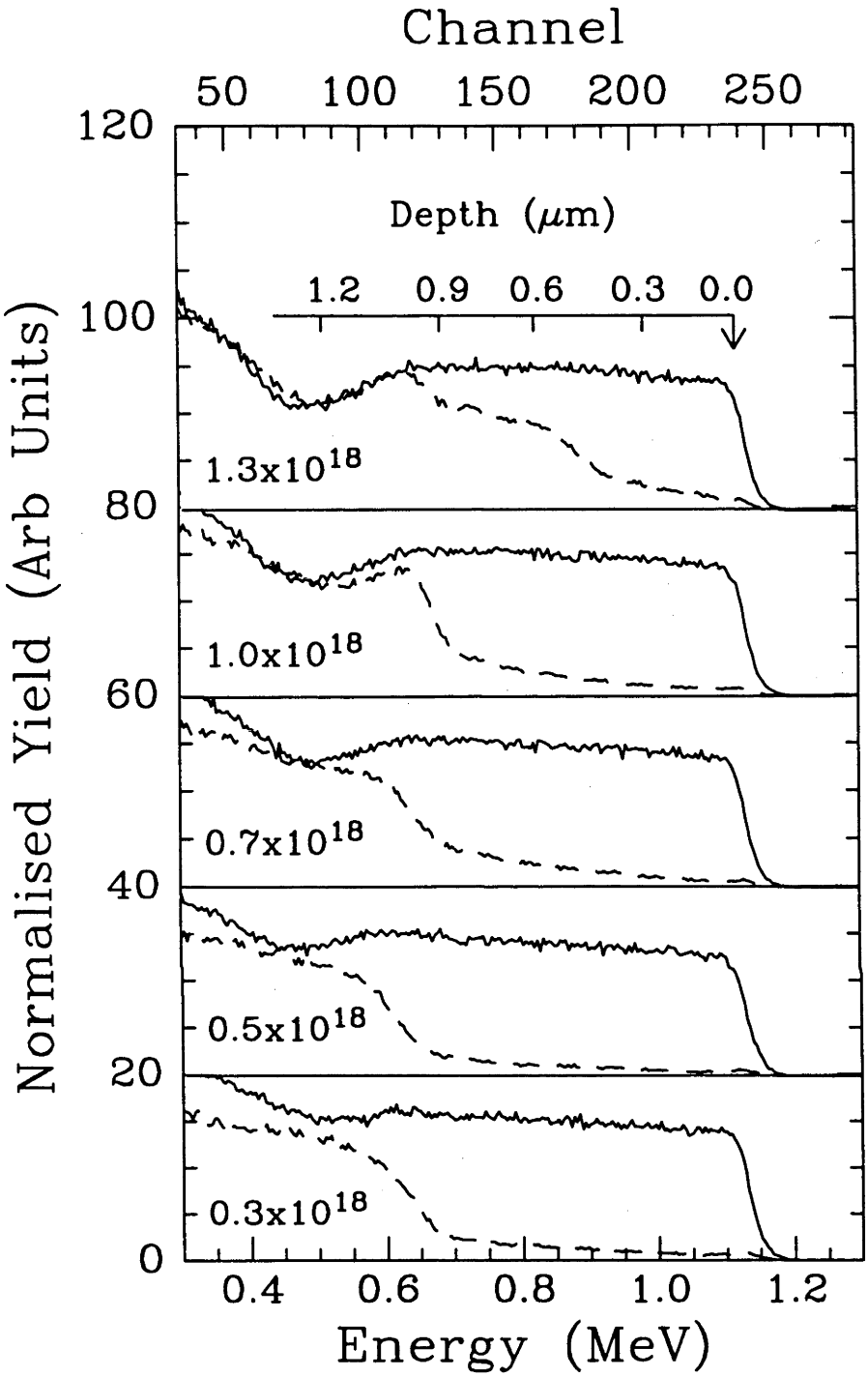

Figure 4.1: RBS/C spectra (obtained with 2 MeV He^+ ions) are shown for O-implanted Si samples (1 MeV, various doses, 150°C). The actual implant temperature is estimated to be between 225 and 300°C. The O dose (cm^{-2}) is listed below the spectra. (——) Random (-----) Channeled

Figure 4.2 shows DCXRD data from these samples. Tensile strain is evident at all doses. An increase in the strain maximum with dose is apparent up to $1x10^{18}$ cm^{-2}. At a dose of $1.3x10^{18}$ cm^{-2}, the strain maximum has decreased but a tensile strain peak is still evident at ~400 arcsec. RC simulations for the O-implanted Si samples (1 MeV, $1.0x10^{18}$ cm^{-2}, 150°C) and (1 MeV, $1.3x10^{18}$ cm^{-2}, 150°C) are shown in Figure 4.3(a) and (b), respectively. The insets show the strain profile used for the simulations; the strain maximum is -4500 and -3750 ppm, respectively. Note that the strain maximum is at a depth of 0.4 μm for the sample (1 MeV, $1.3x10^{18}$ cm^{-2}, 150°C) while it spans depths of 0.7-0.9 μm for the sample (1 MeV, $1.0x10^{18}$ cm^{-2}, 150°C).

The strain maxima (as determined by RADS) for the samples implanted to doses between 0.3-$1.3x10^{18}$ cm^{-2} are shown in Figure 4.4. The strain maximum increases with dose up to $1x10^{18}$ cm^{-2} and decreases at higher doses. Alternatively, the strain maximum increases with dose until a critical strain (~4800 ppm) is reached. Strain relief (or strain relaxation) then occurs, as indicated in Figure 4.4, when the O dose is further increased.

The location of the strain maxima corresponds to a depth within the Si overlayer that is free of damage (as visible by TEM or RBS/C). For example, the strain maximum for O-implanted Si (1 MeV, $1.0x10^{18}$ cm^{-2}, 150°C) spanned depths of 0.7-0.9 μm. In the RBS/C spectra, damage was not indicated over depths of 0-1.0 μm. In the O-implanted Si sample (1 MeV, $1.3x10^{18}$ cm^{-2}, 150°C), damage was apparent by RBS/C at depths >0.45 μm. This is consistent with the simulation of the RC shown in Fig. 4.3(b) wherein strain was not apparent at depths >0.45 μm. Alternatively, for the O-implanted Si sample (1 MeV, $1.3x10^{18}$ cm^{-2}, 150°C), damage formation within the Si overlayer was observed by RBS/C measurements over the same depths at which strain relaxation was apparent.

To further characterise the damage in these samples, XTEM was performed. Figure 4.5 contains micrographs of samples implanted at an energy of 1 MeV and a temperature of 150°C to doses of (a) $7x10^{17}$, (b) $1.0x10^{18}$ and (c) $1.3x10^{18}$ O/cm^2. The end-of-range damage near R_p has resulted in amorphous layer formation in each sample, with stacking faults observed at the front a/c interface at the two lowest doses and dislocations at the back a/c interface for all samples. No damage (over the XTEM field of view) was evident in the Si overlayer for the two lowest fluences whereas in the sample (1 MeV, $1.3x10^{18}$ cm^{-2}, 150°C), a band of dislocations at a depth of 0.55-0.9 μm is apparent. This dislocation network is separated from the a/c interface by crystalline material, i.e. it is spatially separated from the amorphous layer. As well, it is clear that dislocations have formed at the same depth at which an increased χ_{min} was observed in the RBS/C spectra.

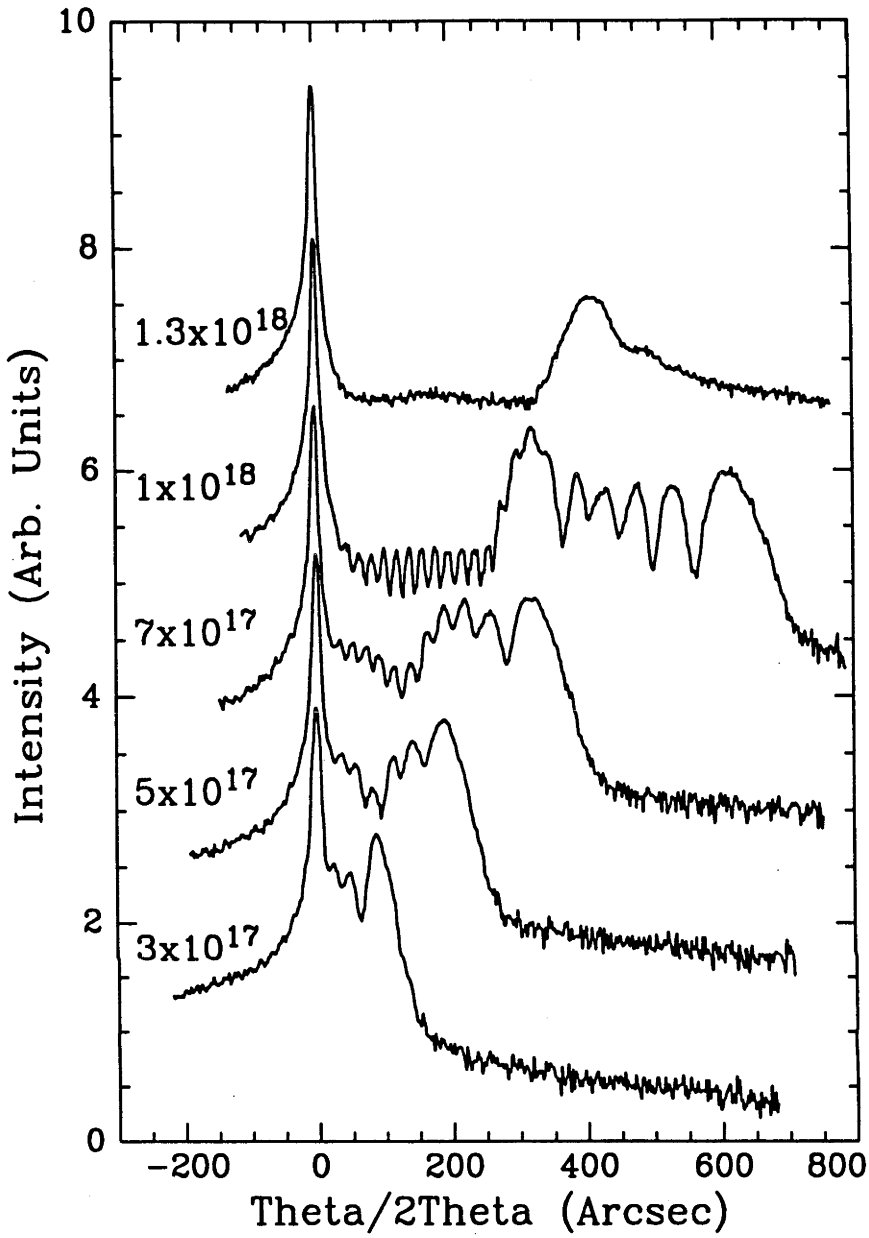

Figure 4.2: DCXRD spectra of O-implanted Si samples (1 MeV, 0.3-1.3x10^{18} cm^{-2}, 150°C). The actual implant temperature is estimated to be between 225 and 300°C. The O dose (cm^{-2}) is listed above the spectra.

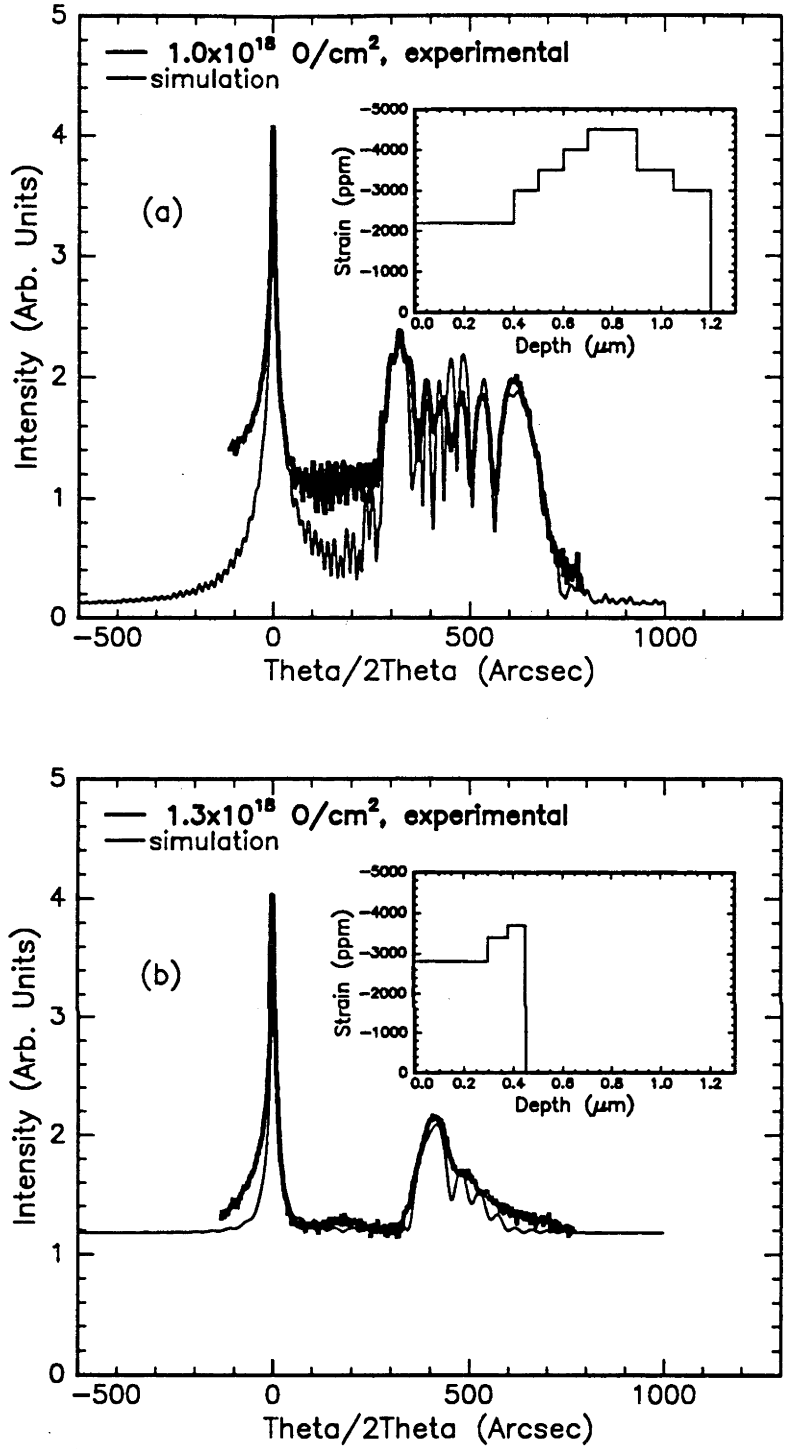

Figure 4.3: Experimental and RADS simulated curve for: (a) O-implanted Si sample (1 MeV, 1.0x10^{18} cm^{-2}, 150°C) and (b) O-implanted Si sample (1 MeV, 1.3x10^{18} cm^{-2}, 150°C). The actual implant temperature is estimated to be between 225 and 300°C. The inset shows the strain profile used in the simulation.

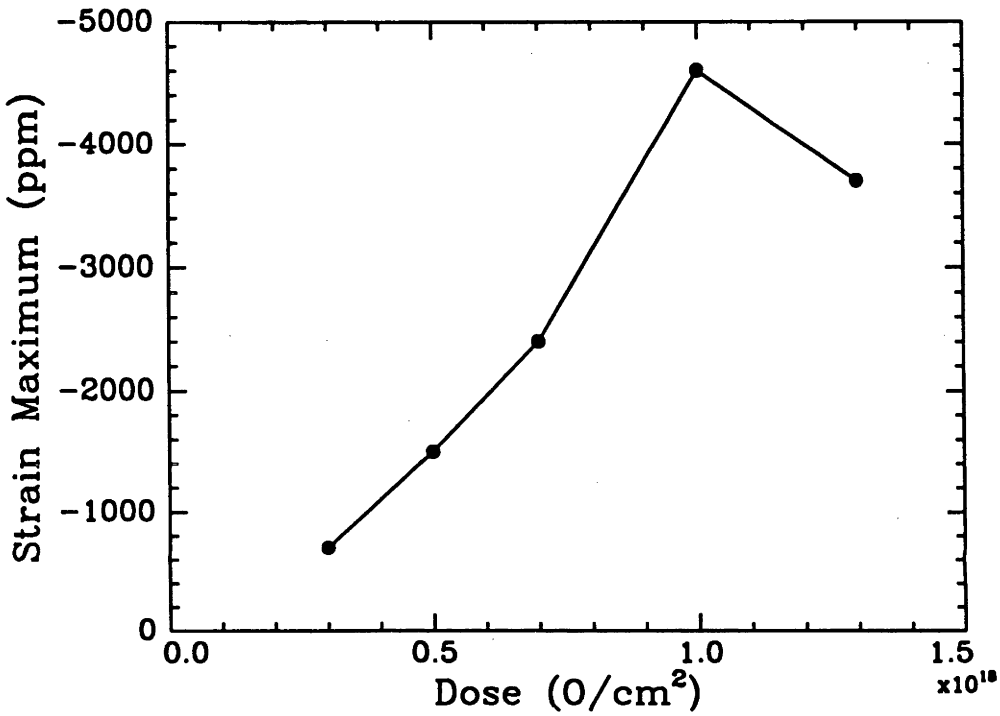

Figure 4.4: The strain maximum at different O doses is shown. Implantation was performed at 1 MeV and an implant temperature of 150°C. (The actual implant temperature is estimated to be between 225 and 300°C).

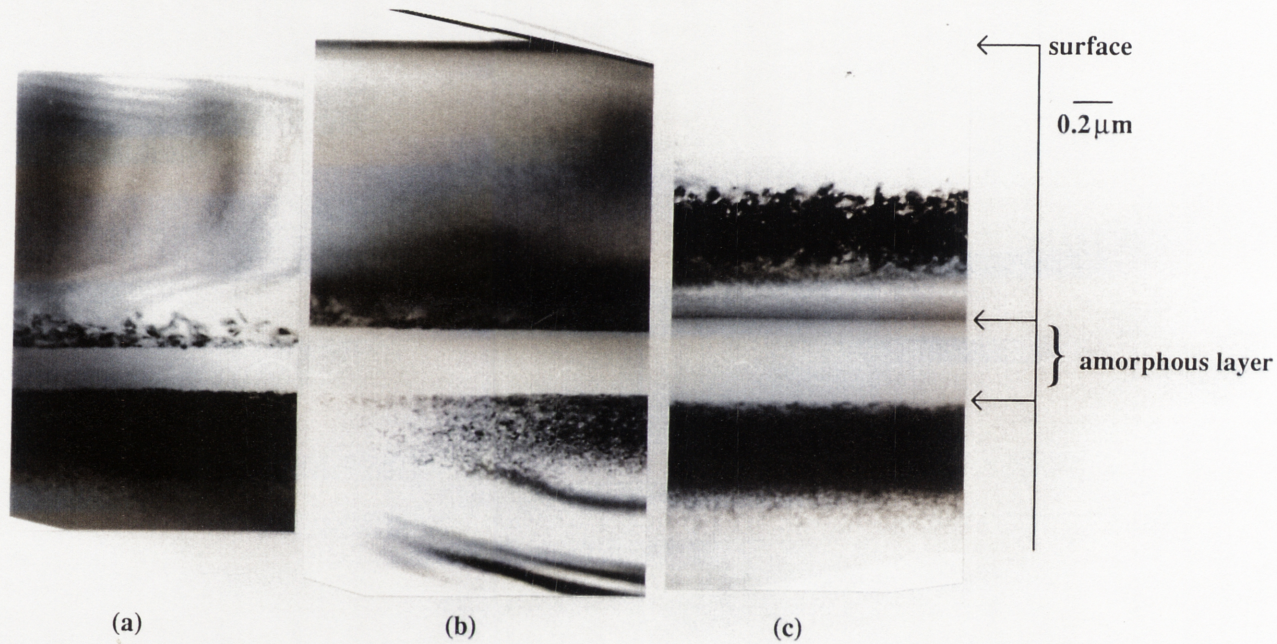

Figure 4.5: XTEM micrographs of Si implanted at 1 MeV and 150°C to doses of (a) $7x10^{17}$, (b) $1.0x10^{18}$ and (c) $1.3x10^{18}$ O/cm^2. (The actual implant temperature is estimated to be between 225 and 300°C.) The samples were oriented along the [011] axis during XTEM analysis.

Hence, the depth of dislocation formation and strain relaxation are correlated in high-dose O-implanted Si.

In the O-implanted Si sample (1 MeV, $7x10^{17}$ cm^{-2}, 150°C), strain was no longer observed with DCXRD after annealing at 950°C for 35 minutes. Figure 4.6 shows the DCXRD spectra before and after annealing. A RC from unimplanted Si is shown for reference. Although the substrate peak has been broadened after annealing (indicating defects are present in the material), the distinct tensile strain peak apparent before annealing has disappeared, indicating strain relief. Figure 4.7 shows a XTEM micrograph of the annealed sample. Cavities (vacancy clusters) are visible within the Si overlayer from the surface to ~0.8 μm. The three-dimensional nature of the bubbles was confirmed by over- and under-focusing of the image. Thus, strain relief in the annealed sample appears to be related to cavity formation from the coalescence of vacancies at high temperature. Cavity sizes ranged from 25-90 Å (cavity size increased with depth) and the cavity concentration was uniform throughout depths of 0-0.8 μm. The presence of cavities at shallow depths (0-0.8 μm) indicates this region was vacancy-rich while the absence of cavities at depths of 0.8-1.2 μm suggests this region was not.

4.1.2 Si-implanted Si

By choosing the appropriate dose, Si implantation will produce similar concentrations of point defects to O implantation, though the chemical effects which were shown to influence damage formation in Chapter 3 will be removed. Figures 4.8(a) and (b) show TRIM simulations of the vacancy and excess vacancy concentrations, respectively, for 1 MeV Si and 1 MeV O implantation in Si. (An excess vacancy concentration within the Si overlayer is the result of the spatial separation of vacancies and interstitials created during implantation. Its' origin and significance is further discussed in section 4.1.3.) In Fig. 4.8(b), a negative excess vacancy concentration actually represents the concentration of excess interstitials. At doses of 2 and $4x10^{17}$ cm^{-2}, Si-implanted Si has the same approximate athermal vacancy and excess vacancy concentration over depths of 0-1.0 μm as O-implanted Si at doses of 7 and $13x10^{17}$ cm^{-2}, respectively. Accordingly, (100) Si was implanted with Si to doses of 2, 4 and $7x10^{17}$ cm^{-2} at an energy of 1.0 MeV and a temperature of 150°C. The dose rate and current density for these implantations were 3.8-4.4$x10^{13}$ ions/cm^2-sec and 6.1-8.5 μA/cm^2, respectively. Again, no conductive Ag paint was used and the sample was simply clamped to the target holder. Thus, the actual implant temperature is estimated to be between 225 and 300°C.

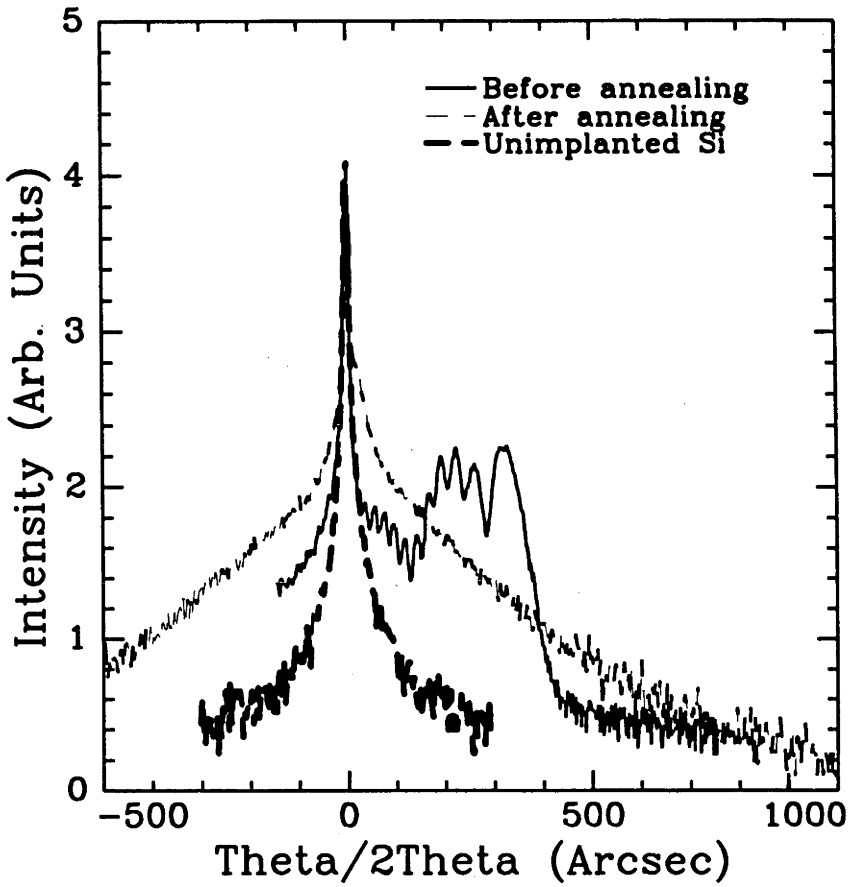

Figure 4.6: DCXRD spectra of O-implanted Si (1 MeV, $7x10^{17}$ cm^{-2}, 150°C) before and after a 950°C, 35 min. anneal. (The actual implant temperature is estimated to be between 225 and 300°C.) A RC from unimplanted Si is also included for reference.

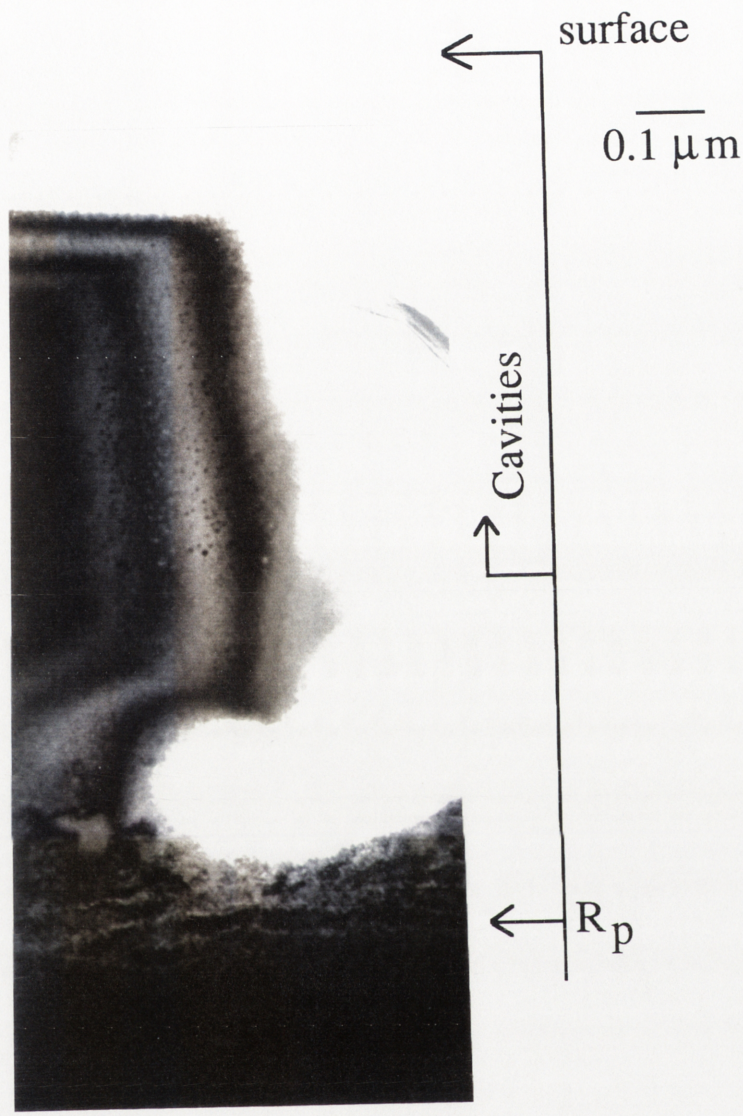

Figure 4.7: XTEM micrograph of O-implanted Si (1 MeV, $7x10^{17}$ cm^{-2}, 150°C) after annealing at 950°C for 35 minutes. The sample was oriented along the [011] axis during XTEM analysis.

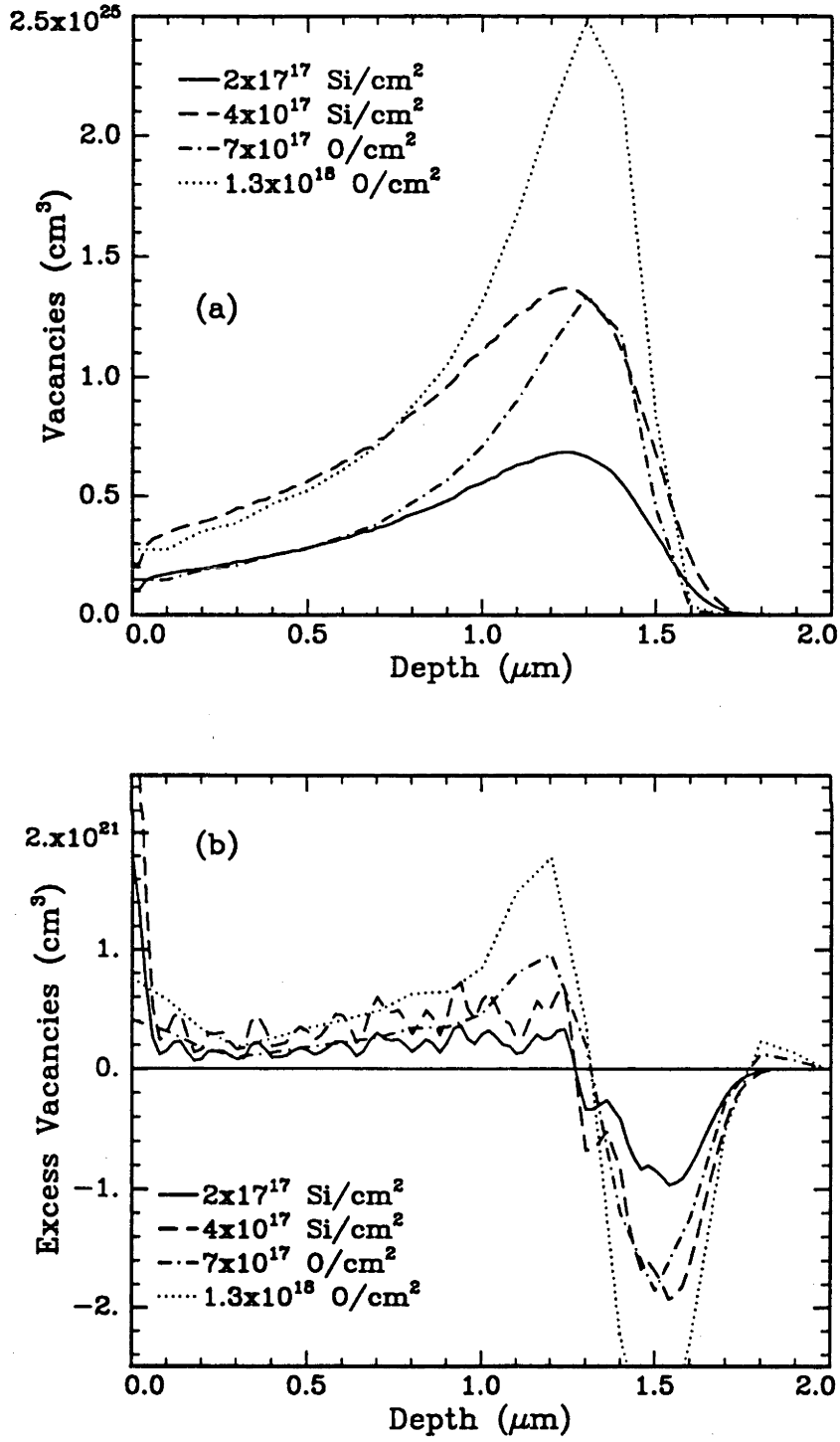

Figure 4.8: TRIM90 simulations of 1 MeV Si-implantation in Si to doses of 2 and 4x10^{17} cm^{-2} and O-implantation in Si to doses of 7 and 13x10^{17} cm^{-2}. (a) vacancy concentration and (b) excess vacancy concentration.

Figure 4.9 shows RBS/C spectra of Si-implanted Si at doses of 2, 4 and $7x10^{17}$ cm^{-2}. A substantially increased χ_{min} within the first 0.9 μm is apparent between fluences of 2 and $4x10^{17}$ cm^{-2} whereas a minimal change in the χ_{min} between 4 and $7x10^{17}$ cm^{-2} is observed. The χ_{min} value of ~30% throughout the Si overlayer in the $2x10^{17}$ cm^{-2} sample results from dechanneling due to a very thin damaged layer at the surface, as observed in the XTEM micrographs shown in Fig. 4.10.

The XTEM micrographs in Figure 4.10 show unannealed Si-implanted Si at various doses. It is evident that the damage at lesser depths than R_p begins closer to the sample surface than for the O-implanted Si sample (1 MeV, $1.3x10^{18}$ cm^{-2}, 150°C) shown in Fig. 4.5. The damage in the Si-implanted Si moves to greater depths with increasing dose. As for O-implanted Si, this damage is spatially distinct from the damage at R_p.

Figure 4.11 shows the DCXRD spectra of these samples. The presence of strain in the Si-implanted Si sample (1 MeV, $2x10^{17}$ cm^{-2}, 150°C) is apparent. For this sample, the strain profile and strain maximum are similar to those of the O-implanted Si sample (1 MeV, $7x10^{17}$ cm^{-2}, 150°C). Assuming point defects are the cause of strain, similar concentrations of point defects in both samples are indicated. This is consistent with TRIM predictions of similar excess vacancy profiles and indicates the vacancy excess for these samples is impurity independent. The dislocations evident by XTEM at the sample surface of the Si-implanted Si (1 MeV, $2x10^{17}$ cm^{-2}, 150°C) are most likely not the result of strain relaxation since the sample is still strained. In the Si-implanted Si samples (1 MeV, 4 and 7 $x10^{17}$ Si/cm^2, 150°C), strain relaxation is evident. As in O-implanted Si, strain relaxation in Si-implanted Si is correlated to dislocation formation as apparent from an increased χ_{min} in the RBS/C spectra of Fig. 4.9. A comparison of the predicted excess vacancy profiles in Fig. 4.8(b) shows that the onset of relaxation and dislocation formation occurred in both O- and Si-implanted Si at doses producing similar excess vacancy concentrations (atomic displacements) over depths of 0-1.0 μm. i.e. at $4x10^{17}$ Si/cm^2 and $1.3x10^{18}$ O/cm^2.

Fig. 4.12 shows a XTEM micrograph of the Si-implanted Si sample (1 MeV, $2x10^{17}$ cm^{-2}, 150°C) after annealing at 900°C for 35 minutes. The presence of cavities is apparent and the cavity size and distribution is similar to the O-implanted Si sample (1 MeV, $7x10^{17}$ cm^{-2}, 150°C). This further suggests the accumulation of the implantation-induced vacancy excess is impurity-independent. It should be noted that the presence of O is generally considered important for stable cavity formation.[35,87,101] However, cavities can be readily produced by high-dose H and He implantation where gas bubbles first form then gas is excluded to leave cavities.[102] The presence of O or

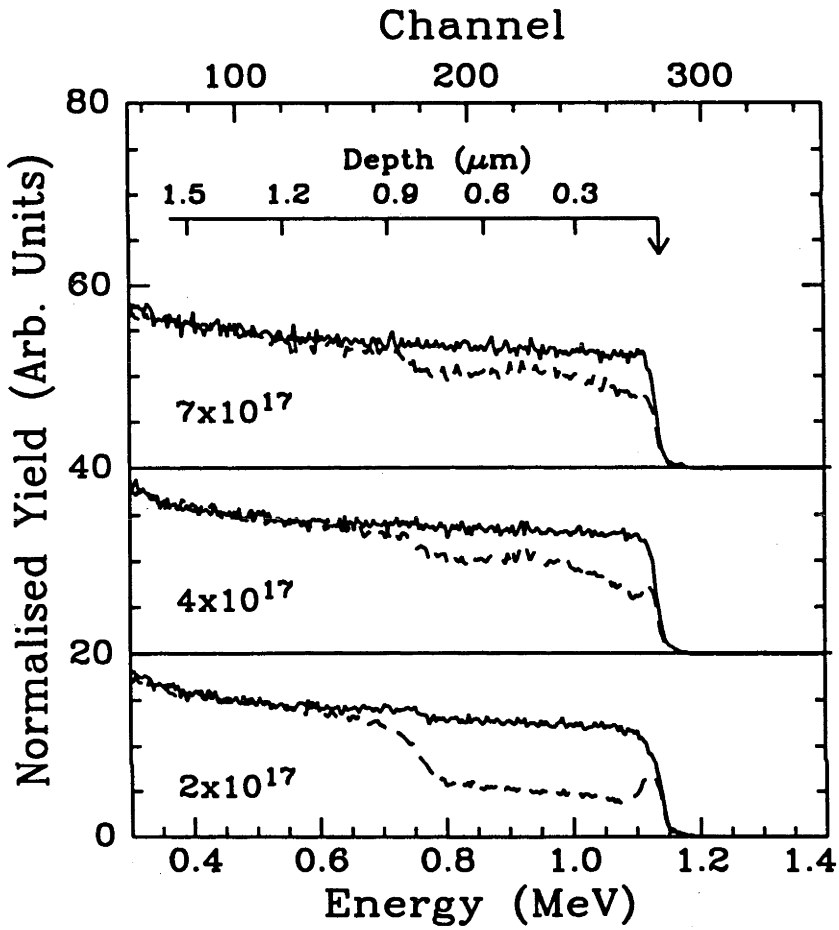

Figure 4.9: RBS/C spectra (obtained with 2 MeV He^+ ions) of Si-implanted Si samples (1 MeV, 2-7x10^{17} cm^{-2}, 150°C). The Si dose (cm^{-2}) is denoted below the spectra.

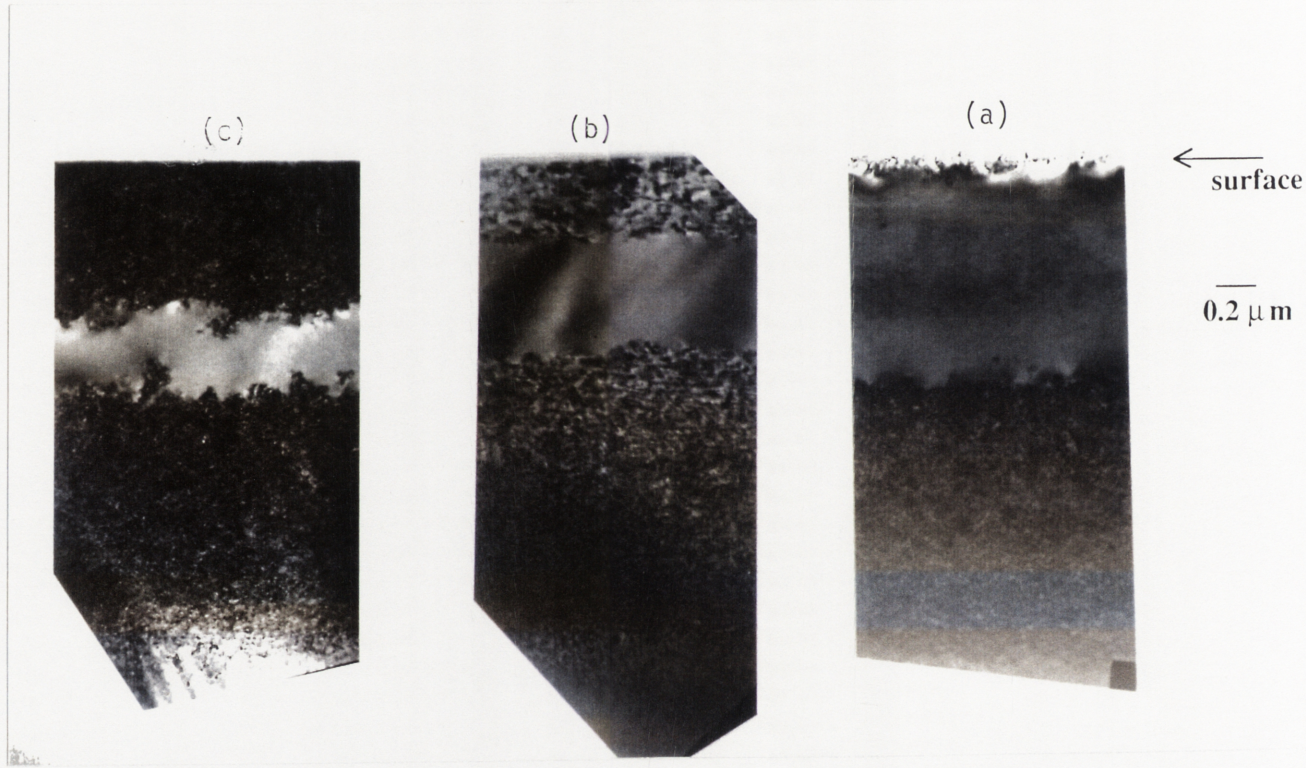

Figure 4.10: XTEM micrographs of 1.0 MeV Si-implanted Si at various doses: (a) $2x10^{17}$, (b) $4x10^{17}$ and (c) $7x10^{17}$ Si/cm^2. The actual implant temperature is between 225 and 300°C. Samples were oriented 2° off the [011] axis during XTEM analysis.

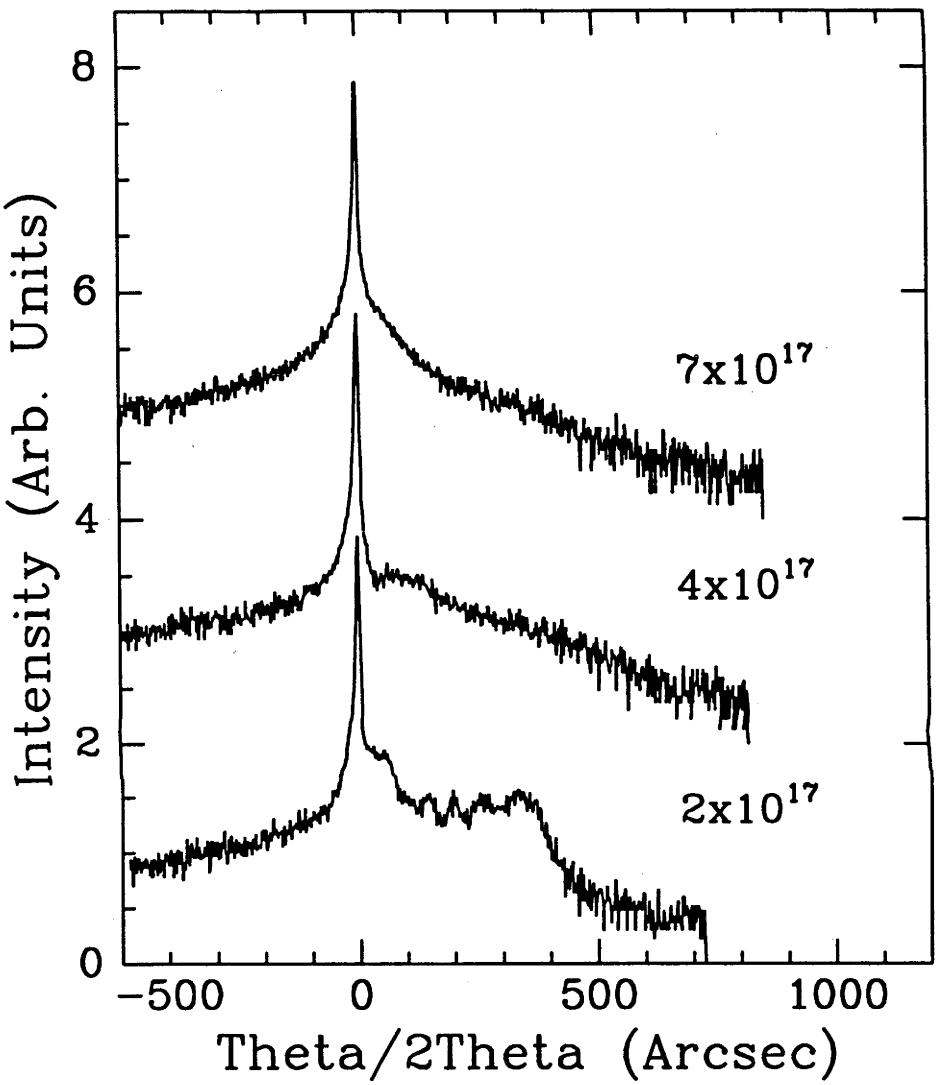

Figure 4.11: DCXRD spectra of Si-implanted Si samples (1.0 MeV, 2-7x10^{17} cm^{-2}, 150°C). The Si dose (cm^{-2}) is given above the spectra. The actual implant temperature is between 225 and 300°C.

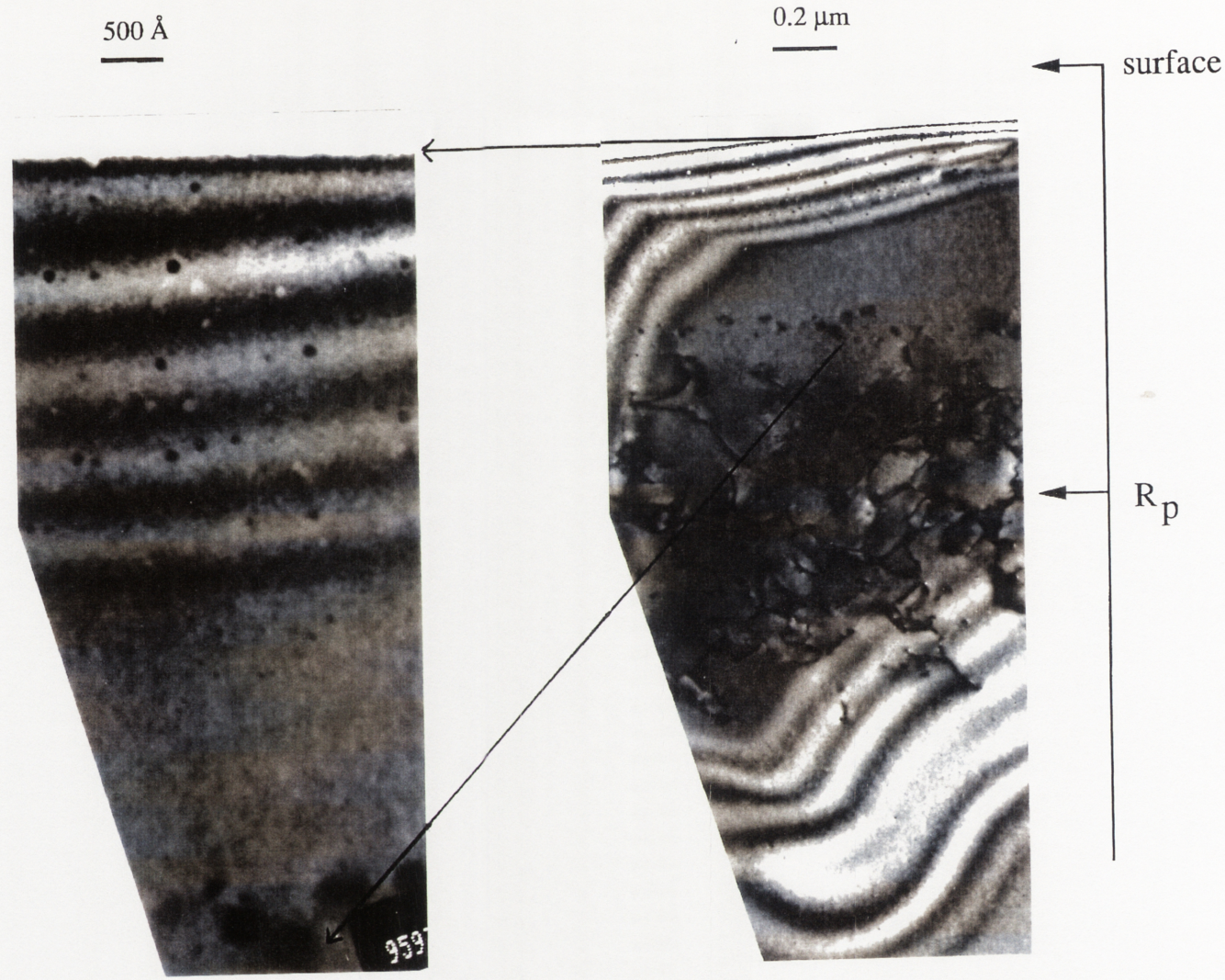

Figure 4.12: XTEM micrograph of a Si-implanted Si sample (1 MeV, $2x10^{17}$ cm^{-2}, 150°C) after annealing at 950°C for 35 minutes. The sample was aligned along the [011] axis during XTEM analysis. The dislocations at the surface seen in the as-implanted sample are no longer visible due to ion milling.

another stabilising gas in the aforementioned Si-implanted samples cannot be completely discounted given the susceptibility to contamination during high-dose implantation.

4.1.3 Discussion

Earlier studies of strain in O-implanted Si (160 keV, various doses, 500°C) reported compressive strain at doses $\leq 3x10^{16}$ cm^{-2}, tensile strain at doses of $0.3\text{-}3x10^{17}$ cm^{-2} and strain relaxation (and dislocation formation) at a dose of $6x10^{17}$ cm^{-2}.[39,40] The compressive strain at low doses was attributed to excess interstitials near R_p prior to the onset of amorphisation. (In the present study, compressive strain was not observed given the dose range of $\geq 3x10^{17}$ O/cm^2.) Tensile strain has been reported by Zhou, et al[69] and Holland, et al[41] in O- and Si-implanted Si. Therein, for O-implanted Si (450 keV, various doses, 450°C), both strain relaxation and damage formation (as measured by RBS/C and XTEM) within the Si overlayer were not apparent until a dose of $1.1x10^{18}$ cm^{-2}. This critical dose (the dose at which strain relaxation occurs) differs from that cited in the present work due to the greater implant energies and lower implant temperatures utilised herein. In the present study, the presence of excess vacancies in high-dose Si- and O-implanted Si has been experimentally confirmed by the existence of tensile strain at depths $<R_p$ and the coalescence of vacancies to form cavities upon annealing. The formation of cavities ~30 Å in diameter in O-implanted Si (160 keV, $0.3\text{-}6x10^{17}$ cm^{-2}, 500°C), after annealing at 900°C for 30 minutes, was observed by Venables et al.[103] In the present study, cavity diameters ranged from 25-90 Å (with diameter increasing with depth) and the cavity concentration was uniform throughout depths of 0-0.8 μm. The greater cavity size reported here indicates a greater number of vacancies (given similar cavity concentrations) in the as-implanted state which is consistent with greater implant doses ($0.3\text{-}1.3x10^{18}$ cm^{-2}).

During irradiation, interstitial-vacancy pairs are created as a result of atomic displacements produced by either the impinging ion or energetic knock-ons between target atoms. These point defects are created in very high numbers (dpa = 60-600) during implantation and result in a distribution of defects throughout the Si overlayer. However, the primary knock-on atoms (atoms displaced by the primary incoming ion) have a component of momentum along the incident ion direction (i.e. into the target). Consequently, on average, the component of momentum transferred in the direction of the incident ion will be non-zero. This leads to a spatial separation of the interstitial and

vacancy depth distributions and can create local excesses of one defect-type at various depths along the ion track. Upon examination of the *net* recoil density, i.e. the difference between the distribution of recoiled atoms (interstitials) and the vacancies generated by the displacement cascade at a given depth, point defect excesses can be predicted.

This spatial separation of Frenkel pairs yielding excess vacancy and interstitial concentrations has been predicted by Mazzone.[104] Using Monte Carlo calculations, the net recoil distribution was calculated for 50 keV P-implanted Si. A vacancy excess between the surface and $0.8R_p$ and an interstitial excess between R_p and $2R_p$ was predicted. Experimentally, the concentration of point defects will be affected by implant conditions. The availability of preferential sinks for vacancies or interstitials will influence the number of residual excess point defects. Residual vacancies/open volume defects will result when there is a spatial separation of vacancies and interstitials (as explained above) as well as when there is a preferential sink for interstitials. In addition, the implant temperature and dose rate will affect the amount of point defect recombination. Point defect excesses are most likely to be detected when the recombination of generated point defects is at a minimum, i.e. at low implant temperatures, or when the total concentration of excess point defects is greatest, i.e. at high doses, since primary knock-ons represent <0.1% of the total number of collisions.

As demonstrated in the previous sections, strain relaxation and dislocation formation in both O- and Si-implanted Si are correlated. One of two explanations is possible. Either (1) dislocations were nucleated within the Si overlayer by some mechanism other than strain relief and strain reduction at depths of damage formation resulted or (2) dislocation formation is a consequence of the Si lattice yielding due to excess strain. The latter explains both the nucleation of dislocations at depths of the highest excess vacancy concentration (as deduced from RADS simulations) and the spatial distribution of cavities in XTEM micrographs of strained samples upon annealing. In the present study, the absence of cavities at depths of ~0.8-1.1 μm indicates either (1) vacancy-interstitial recombination at these depths, (2) gettering of excess vacancies to the a/c interface and/or (3) vacancy diffusion from these depths. The nucleation of damage in O- and Si-implanted Si (which were performed under similar implant conditions) at the same predicted excess vacancy concentration is also consistent with the latter explanation. The presence of an excess vacancy concentration at depths $<R_p$ in both O- and Si-implanted Si implies that this is characteristic of the implantation process rather than a chemical effect. Thus, this effect should be evident in other high-dose ion-implanted materials systems. An investigation into the effect of implant temperature on the critical dose for strain relaxation/ dislocation formation

provides further insight into the observed phenomena; such a study follows in the next section.

Finally, damage nucleation was evident at shallower depths in Si-implanted Si in contrast to O-implanted Si (compare Figs. 4.5 and 4.10). As previously explained, the final disorder depends greatly on dynamic annealing and the availability of sinks for defects. In comparison to O implantation, the nuclear stopping power is higher overall for Si implantation (for a common implant energy) and this will lead to higher instantaneous concentrations of defects that can yield higher net concentration of post-implantation defects. Figure 4.13 shows the electronic, nuclear and total stopping power of Si and O ions implanted in Si versus energy as predicted by TRIM90. For Si, $(dE/dx)_N$ is approximately twice that of O near the surface. Since defects agglomerate at/or near sinks, more damage would be expected at the surface for Si implantation. For the latter, $(dE/dx)_N$ is skewed towards R_p and consequently, more defects would be attracted to sinks near R_p.

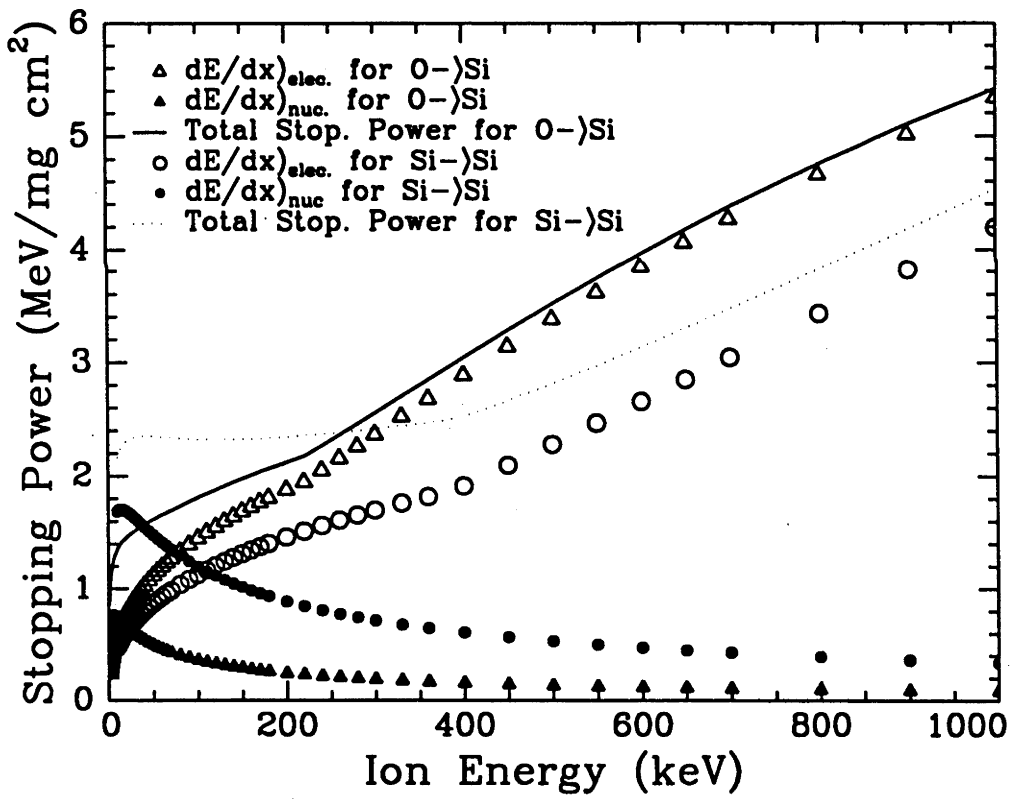

Figure 4.13: Electronic, nuclear and total stopping power of O- and Si-implanted Si versus energy from TRIM90.

4.2 Strain in O-implanted Si; a Temperature Study

4.2.1 Experimental Results

In the previous section, the presence of tensile strain within the Si overlayer of high-dose ion-implanted Si was established. A correlation between strain relaxation and dislocation formation in this region was also demonstrated. In order to gain a better understanding of the mechanism responsible for this correlation, the temperature dependence of dislocation formation and strain relaxation was studied.

The maximum strain before relaxation (and the corresponding critical dose) were studied at implant temperatures of 150-450°C in 1 MeV O-implanted Si. In contrast to the experiments described in the previous section, the wafer and target holder were in good thermal contact due to the use of Ag paint in addition to clamping. Figure 4.14 shows RBS/C spectra for O-implanted Si for various implant temperatures at a dose of 0.7×10^{18} cm^{-2}. At this dose, amorphous layer formation is evident for implant temperatures <450°C. As expected, the width of the amorphous layer increases with decreasing implant temperature. In contrast, the amount of damage within the Si overlayer is low in all samples. The increased χ_{min} in the low implant temperature samples (150 and 225°C) is probably the result of dechanneling due to the larger surface peak and/or the decreased dynamic annealing in these samples which yields a greater net point defect concentration relative to samples implanted at higher temperatures ($\geq$ 300°C). Dislocation formation within the Si overlayer is not evident at any implant temperature. The DCXRD spectra of these samples are shown in Figure 4.15. Tensile strain is evident for all samples with higher strains evident as the implant temperature is decreased. Lower implant temperatures yield a significantly higher strain maxima due to a higher excess vacancy concentration, as consistent with decreased dynamic annealing.

After O implantation to a higher dose of 1×10^{18} cm^{-2}, dislocation formation is evident in certain samples. Figure 4.16 shows the RBS/C spectra for O-implanted Si at implant temperatures of 150-450°C. An increase in the width of the amorphous layer (as compared to the lower dose samples shown in Figure 4.14) is observed at all implant temperatures, while dechanneling within the Si overlayer is only apparent for samples implanted at 300 and 450°C. The depth over which dechanneling is observed is temperature dependent with dechanneling apparent at 0.6 and 0.4 μm in the 300 and 450°C samples, respectively. Samples implanted at temperatures of 150 and 225°C

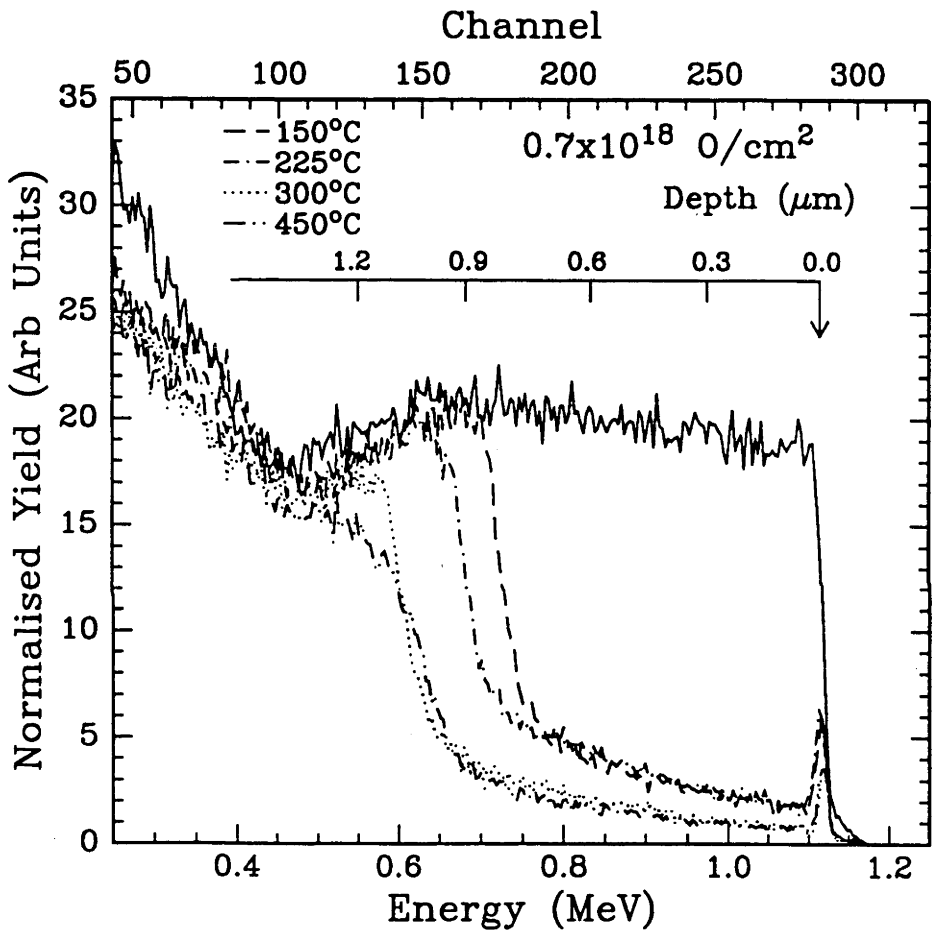

Figure 4.14: RBS/C spectra (obtained using 2 MeV He^+ ions) of O-implanted Si (1.0 MeV, 0.7x10^{18} cm^{-2}, 150-450°C).

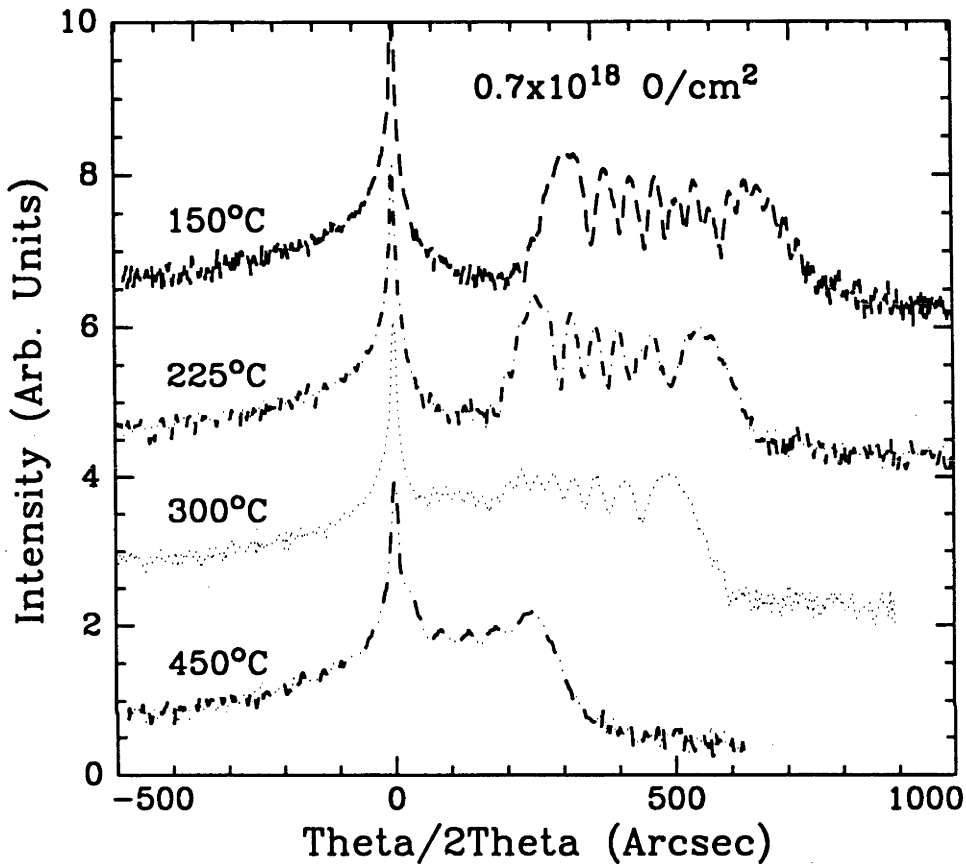

Figure 4.15: DCXRD spectra of O-implanted Si (1.0 MeV, 0.7x10^{18} cm^{-2}, 150-450°C).

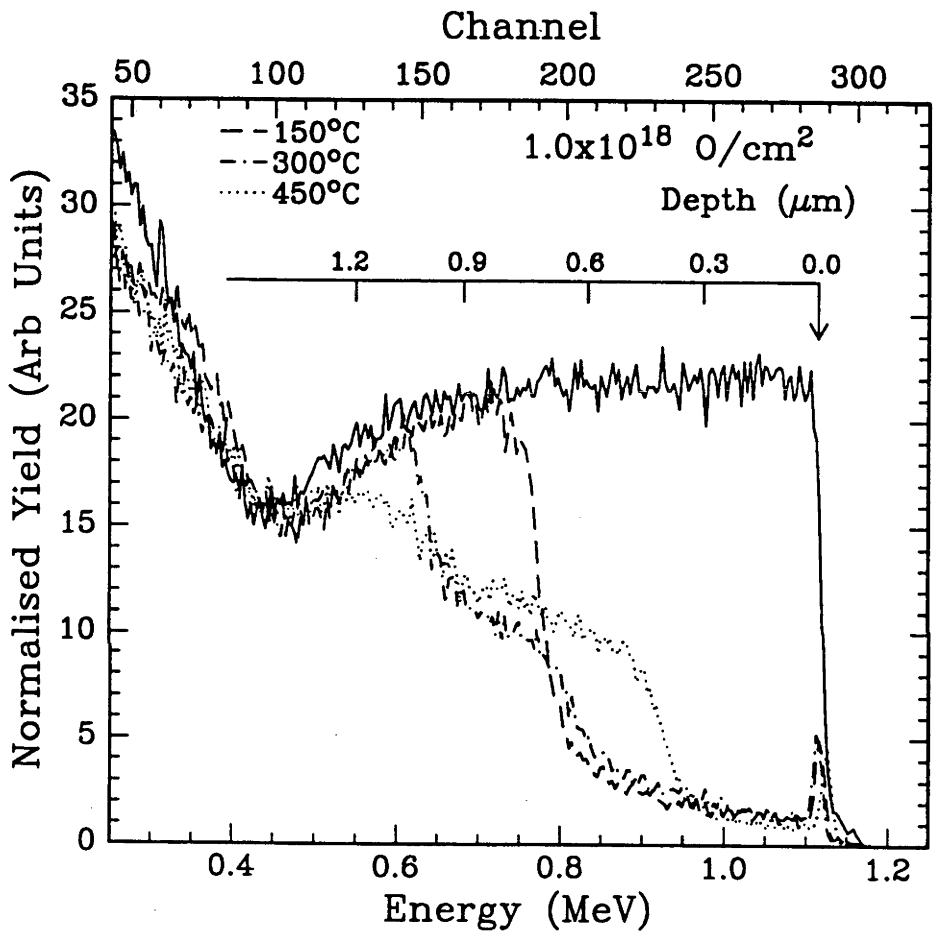

Figure 4.16: RBS/C spectra (obtained using 2 MeV He^+ ions) of O-implanted Si (1.0 MeV, 1.0x10^{18} cm^{-2}, 150-450°C).

(the latter not shown) exhibit a dislocation free Si overlayer for doses <$1.3x10^{18}$ O/cm^2.

The DCXRD spectra for these samples are shown in Figure 4.17. The broad "peak" evident to the right of the substrate peak for the sample implanted at 450°C is consistent with Huang scattering, i.e. scattering due to extended defects.[55,59] A similar although more structured RC is apparent for the 300°C sample. Again, the high background signal is consistent with Huang scattering, yet the RC peaks at ~150 and 320 arcsec indicate tensile strain is still present. However, the strain maximum is reduced relative to the sample implanted to a lower dose ($0.7x10^{18}$ cm^{-2}) as shown in Figure 4.15. This is consistent with the RBS/C measurements wherein dislocation formation within the Si overlayer was observed. In contrast to high temperature implantation, samples implanted at 150 and 225°C (the latter not shown) exhibit a further increase in the strain after implantation to $1x10^{18}$ cm^{-2} and no increase in the background signal is evident.

4.2.2 Discussion

The data presented in the last section demonstrates that implant temperature has an effect on both the strain magnitude and dislocation formation in O-implanted Si. This is more clearly shown in Figure 4.18(a) where the strain maximum after implantation to a dose of $0.7x10^{18}$ O/cm^2 is plotted as a function of implant temperature. For a given O dose, higher implant temperatures result in lower strain. The recombination of Frenkel pairs created during implantation will be greater at higher temperatures as there is more thermal energy available for such processes to occur. Because strain is due to the vacancy excess that results from implantation, lower strains are expected in samples with lower excess vacancy concentrations, i.e. in high implant temperature samples. In addition, the measured strain will also depend on the structure of the vacancy excess. For example, the potential for vacancy clustering (cavity formation) increases as implant temperature increases; as demonstrated in section 4.1.1, cavities result in less strain than singular vacancies. Consequently, high implant temperatures would be tend to result in less tensile strain. (The lower strain associated with vacancy clustering has been used to produce low defect density SIMOX material.[35,36])

Figure 4.18(b) shows the strain maximum before relaxation/dislocation formation within the Si overlayer and the critical dose as a function of implant temperature. There are two convoluted effects that influence the slope of these curves. First, the strain maximum before yield is temperature dependent because Si yield strength is

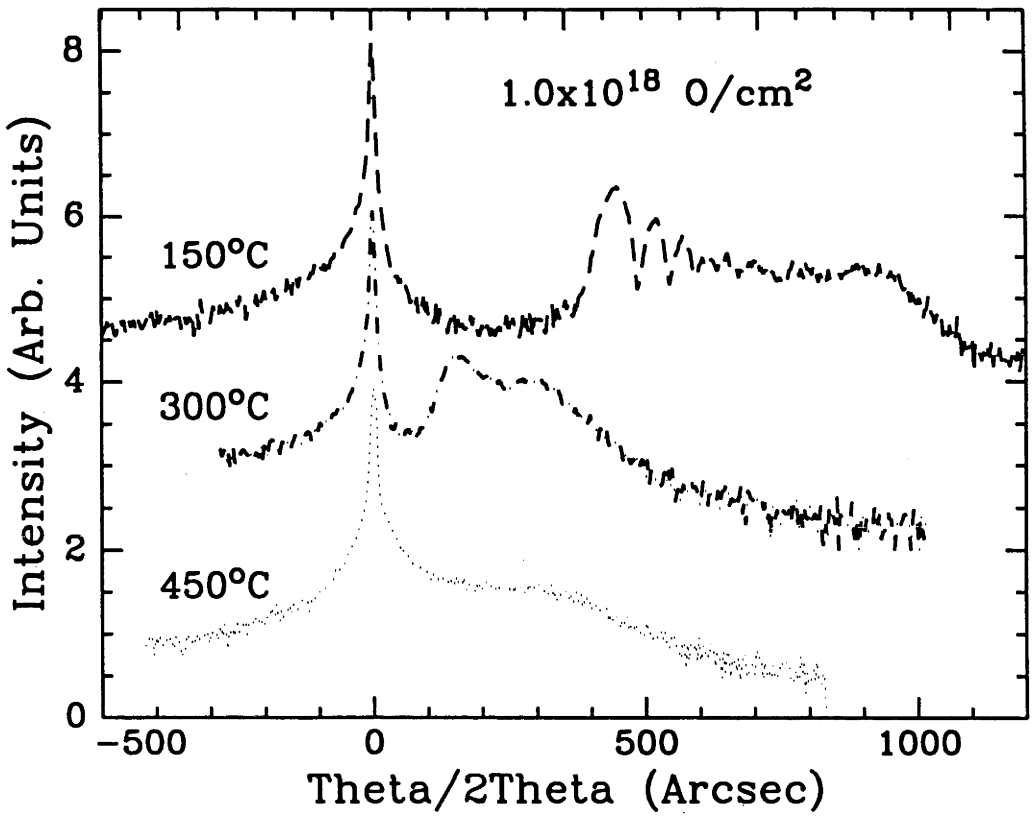

Figure 4.17: DCXRD spectra of O-implanted Si (1.0 MeV, 1.0x10^{18} cm^{-2}, 150-450°C).

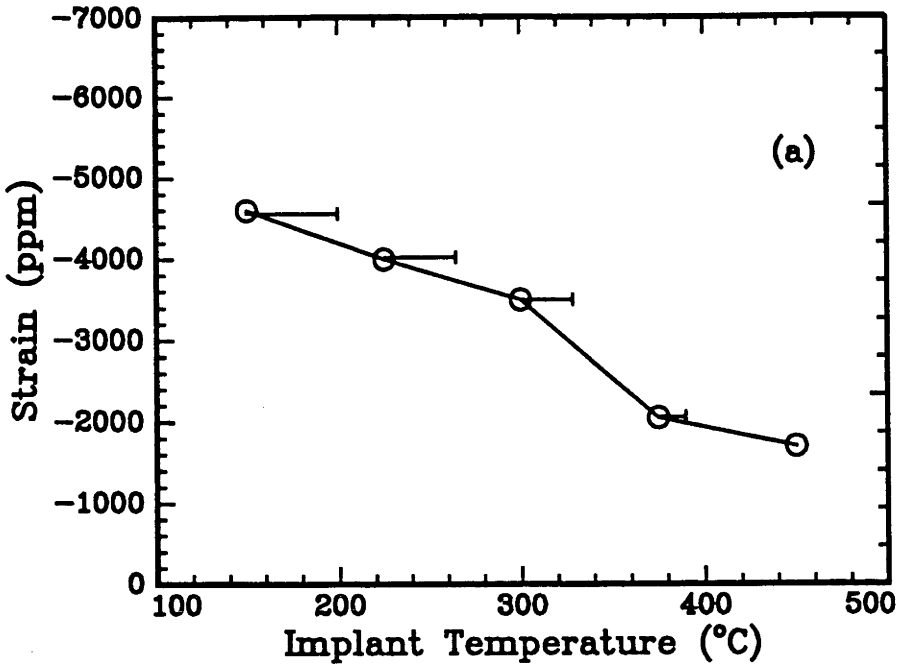

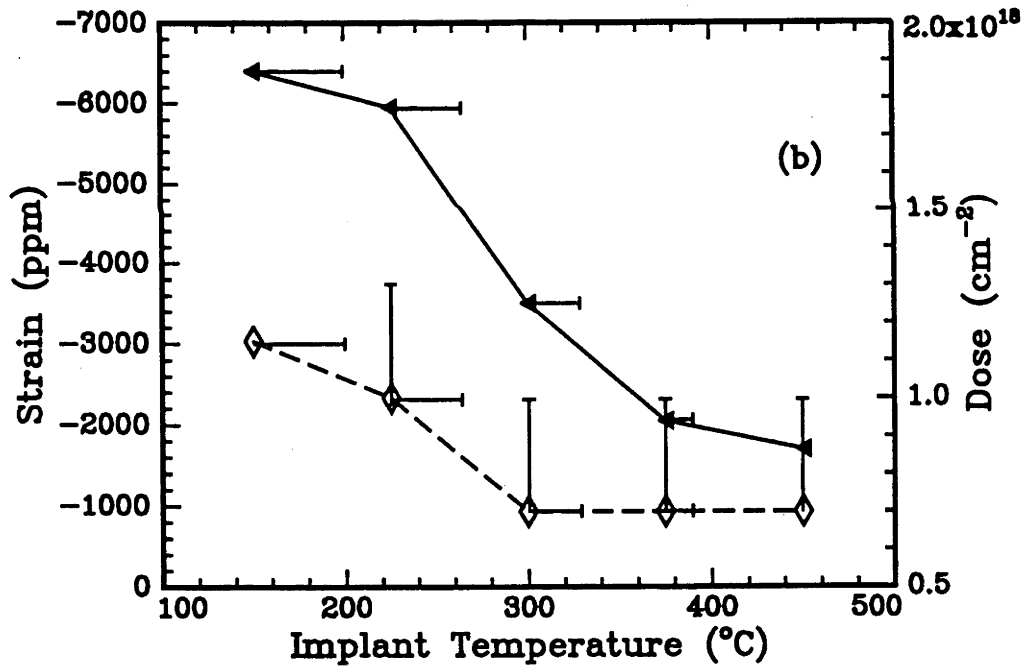

Figure 4.18: (a) The strain maximum after implantation to a dose of $0.7x10^{18}$ O/cm^2 plotted as a function of implant temperature and (b) the strain maximum before strain relaxation (——) and the critical dose (-----) plotted as a function of implant temperature.

temperature dependent. This effect is independent of the implantation process. Second, the implantation-induced strain is also implant temperature dependent. Increased dynamic annealing at higher implant temperatures means a higher dose is necessary to produce a given strain. In addition, accumulation of strain is dependent on the implantation conditions. Consequently, it is a combination of strain accumulation as controlled by the implantation process and the inherent temperature dependence of the Si yield strength which will determine the critical dose for dislocation formation within the Si overlayer of O-implanted Si. When the yield strength of the Si lattice is exceeded, strain relaxation through dislocation formation results.

Little data on the yield behaviour of Si below 400°C is available. At 400°C, a strain of 2000 ppm at the yield point in single crystal Si has been reported. [105,106] This is comparable to the strain at yield (1800 ppm) in Si implanted with 1 MeV O ions at 450°C. The flow stress at yield can be calculated by:[107]

$$\sigma = 2G\varepsilon_x \frac{(1+\upsilon)}{(1-\upsilon)} \qquad (4.1)$$

where G = shear modulus of Si ($6x10^4$ MPa)
υ = Poisson's ratio (0.278)
ε_x = strain at yield as measured by DCXRD.

This equation is valid if the stress state in the surface layer is biaxial, i.e. out of plane stresses are negligible. The strain parallel to the surface can be measured using DCXRD in asymmetric geometries such as the (044) reflection at glancing angle incidence. Previous measurements in O-implanted Si show that strain is accommodated by a tetragonal distortion of the lattice, such that the average strain parallel to the surface is negligible.[39,108,109]

Figure 4.19 shows the flow stress of Si as a function of temperature. This figure is from Castaing, et al[106] with the addition of data for ion-implanted samples from various sources including this thesis. In ion-implanted material, the horizontal axis represents the implant temperature. For unimplanted Si, the flow stress is influenced by the strain rate during deformation since the yield behaviour is controlled by the number and velocity of dislocations generated at early stages of the deformation process. Fig. 4.19 shows that the relationship between flow stress and temperature is similar for implanted and unimplanted Si, further indicating that strain relaxation/dislocation nucleation in ion-implanted samples results when the Si yield strength is exceeded. Consequently, the strain maximum attainable at a given O dose decreases as the implant

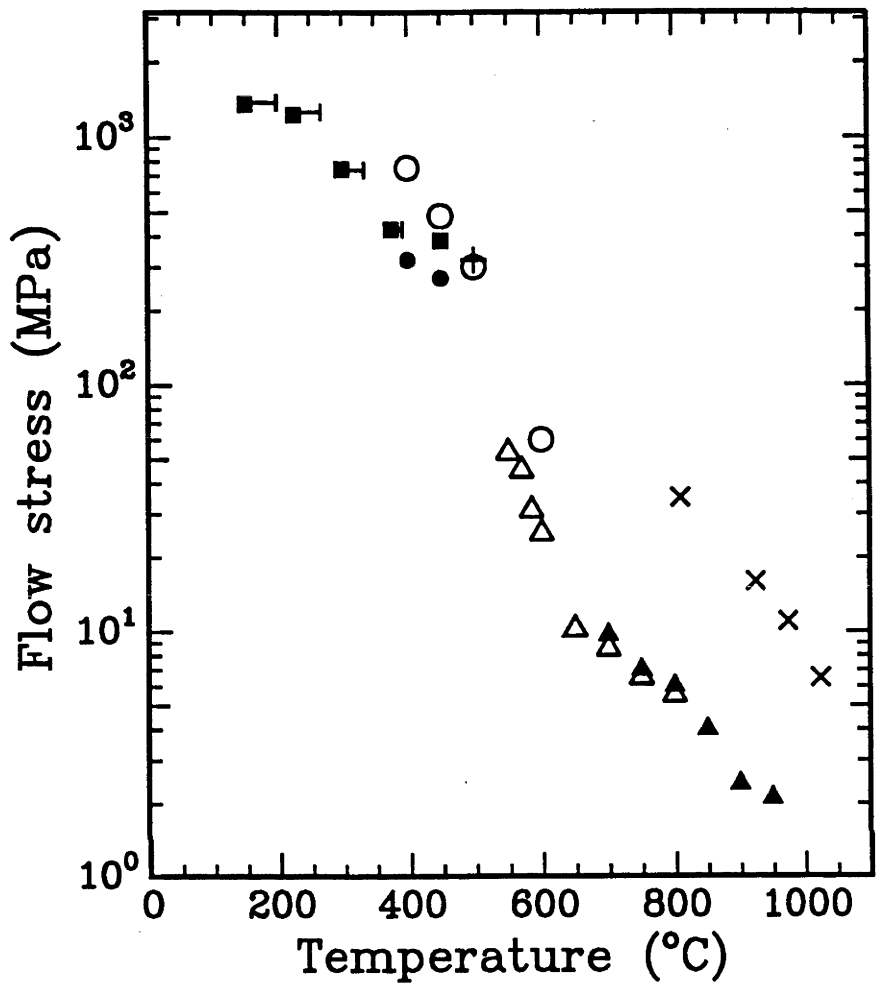

Figure 4.19: Flow stress of Si as a function of temperature. In ion-implanted material, the horizontal axis represents the implant temperature.

(○) Castaing[106] where $\dot{\varepsilon} = 5x10^{-6}\ sec^{-1}$.

(●) Castaing[106] where $\dot{\varepsilon} = 5x10^{-5}\ sec^{-1}$.

(Δ) Omri[110] where sample was pre-strained ($\dot{\varepsilon} \sim 2x10^{-5}\ sec^{-1}$*).*

(▲) Omri[110] where sample was unstrained.

(x) Patel[105] where $\dot{\varepsilon} \sim 8x10^{-5}\ sec^{-1}$.

(+) Venables[39] for ion-implanted Si.

(■) This work.

temperature increases. Equivalently, although the yield strength, and hence strain maximum before relaxation is dependent on implant temperature, the accumulation of strain (which is mediated by the number and mobility of point defects) is also implant temperature dependent. Thus, the strain at yield will be fixed by the implant temperature, but the strain accumulation may vary with other implant conditions such as impurity concentration and implanted ion energy, mass and dose rate. Consequently, the critical ion dose for yield will also be a function of implant parameters and cannot be explicitly known without knowledge of the dependency of strain accumulation on the implant parameters. This explains why the results presented herein contradict those of Holland et al[41] for O-implanted Si (450 keV, various doses, 450°C) and (500 keV, various doses, 320°C) wherein the higher implant temperature resulted in dislocation formation within the Si overlayer at a higher dose.

4.3 Conclusions

The results presented in this chapter have contributed to the basic understanding of the role of point defects in damage formation in high-dose ion-implanted Si. Damage accumulation/ dislocation formation near the ion end-of-range and at depths < R_p, were observed to be separate and distinct from each other. In the dose range studied, the end-of-range damage appears to increase with dose whereas within the Si overlayer, a sudden onset of damage appears above a critical dose. Strain measurements at doses below the critical dose showed the presence of tensile strain within the Si overlayer, indicating a lattice contraction. This tensile strain was shown to increase with dose, until a critical dose was reached whereupon strain relaxation was evident. The critical dose for strain relaxation and dislocation formation is equivalent, indicating the two phenomena are correlated. That is, at sufficiently high values of strain, the strain drives the formation of dislocations. Simulations placed the tensile strain maximum within the Si overlayer at the same depth where dislocation formation first occurs. Studies performed in both O- and Si-implanted Si indicated that it was the implantation-induced vacancy excess within the Si overlayer that determines strain and consequently the critical dose for dislocation formation is such material.

The tensile strain within high-dose ion-implanted Si is the result of the spatial separation of Frenkel pairs created during implantation. A component of the forward momentum of the primary ion-atom interaction is non-zero which leads to the development of local excesses of point defects along the ion path. A local excess of

interstitials is located at ~R_p whereas a vacancy excess is evident at depths less than R_p. The vacancy excess is the cause of the tensile strain within the Si overlayer. Indeed, when ion-implanted strained Si is annealed, the strain is decreased as the result of vacancy clustering.

Studies of strain relaxation and dislocation formation at various implant temperatures further explained the correlation between strain relaxation and dislocation formation. The strain at yield increased as the implant temperature decreased and such behaviour followed that of the flow stress in bulk Si as a function of temperature. Hence, the mechanism for yield in ion-implanted Si is simply strain accumulation until the yield strength of Si is exceeded. In ion-implanted material, the accumulation of strain is strongly process dependent. Several process parameters such as impurity concentration, implanted ion energy, mass, dose, dose rate and implant temperature will affect the strain in the material after implantation.

To the author's knowledge, this is the first report of Si yield strength data at temperatures below 400°C. In the past, such studies were made by pulling on two ends of a bulk Si sample and consequently brittle failure occurred before flow stress was reached. If the accumulation of strain during implantation is controlled so the yield strain at a given implant temperature is never reached, the post-anneal defect density in the Si overlayer should be low. In addition, by reducing the implant temperature, the yield strain increases. As a consequence, the conventional three stage sequential implant and anneal process is potentially reducible to a two-step procedure through a reduction in implant temperature. This would aid in significantly reducing the cost of SIMOX material.

Chapter 5

Damage Reduction in Strained and Strain-Relaxed O-implanted Si by a Secondary Si Implant

5.0 Introduction

From the experiments presented in the previous chapter, a greater understanding of the origin of strain and its correlation to dislocation formation in ion-implanted Si has been achieved. Such knowledge gives better direction to the search for the most timely and economical fabrication of SIMOX material. As a result, new methods for producing low-defect density SIMOX material are suggested. One such technique would be to delay the onset of dislocation formation within the Si overlayer by reducing the strain that accumulates during O implantation. Through manipulation of the point defect concentrations which result from the implantation process, strain can be reduced. Such a technique would allow higher O doses before the onset of dislocation formation and could reduce the required number of sequential implant and anneal steps.

Similarly, damage reduction in strain-relaxed O-implanted Si by high-energy Si irradiation is also explored in this chapter. If the damage which results from a single high-dose implant could be reduced, the need for sequential implantation and annealing to produce low-defect density SIMOX material could be eliminated. The use of a secondary Si-ion implant for damage reduction is derived from the "ion-beam-defect-engineering" studies of Lu et al[111] and Wang, et al.[112] In these reports, a pre-anneal,

secondary Si-ion implant resulted in a significant reduction to the post-anneal, extended defect concentration. The reduction in defect density was attributed to the gettering of Si interstitials, generated by the primary dopant-ion implant, to disorder associated with the secondary Si-ion implant. The use of a secondary Si-ion implant for damage reduction is schematically depicted in Figure 5.1. A pre-anneal, secondary Si-ion implant with a projected range (R_2) either less than or greater than that of a primary, dopant-ion implant (R_1) was shown to result in a significant reduction of the post-anneal, extended defect concentration at R_1. A similar technique is presented in this chapter for application to SIMOX material with the aim of reducing post-anneal disorder at the Si/SiO_2 interfaces.

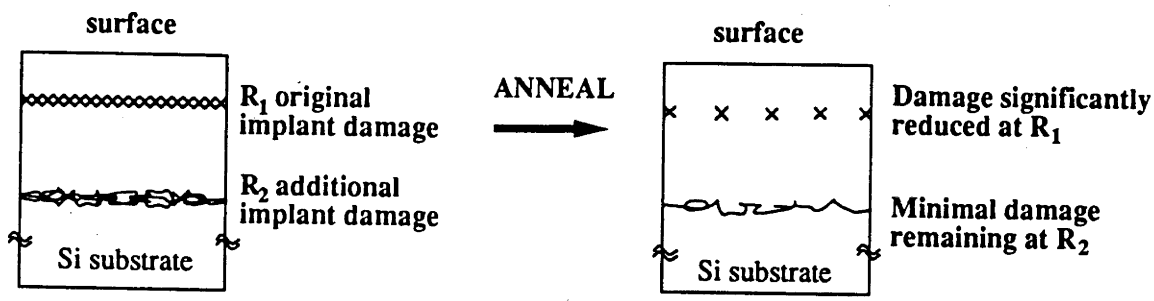

Figure 5.1: Schematic drawing illustrating the concept of ion-beam-defect-engineering

5.1 Si implantation into Strained O-implanted Si

5.1.1 Strain Reduction by Si Implantation to Various Depths

The role of strain in dislocation formation in high-dose ion-implanted Si was established in Chapter 4. In this section, the effect of a secondary Si implant on strain in O-implanted Si is studied. Si (100) p-type wafers were implanted at 150°C with 1.0 MeV O^+ ions to doses of (1-2.1)x10^{18} cm^{-2} at a current density of 12-20 $\mu A/cm^2$. Samples were subsequently implanted at 150°C with Si ions at energies, doses and current densities of 0.1 or 4.2 MeV, 3x10^{15} or 6x10^{16} cm^{-2} and 1 or 2 $\mu A/cm^2$, respectively. These Si implant energies have an R_p of 0.15 and 3.0 μm, respectively. (The temperature control during implantation is assumed to be very good due to the low current density during implantation.) Under such conditions, the high-energy Si implant (4.2 MeV, 6x10^{16} cm^{-2}, 150°C) will add to the vacancy excess in the Si overlayer, i.e. over the strained region. The low-energy Si implant (0.1 MeV, 3x10^{15} cm^{-2}, 150°C) will add to the vacancy excess over depths of 0-0.1 μm and will add excess interstitials at greater depths, i.e. at ~0.15 μm (Si R_p). As well, the implanted Si ions will contribute to the excess interstitial concentration.

Figure 5.2 shows DCXRD and RBS/C spectra for O-implanted Si (1 MeV, 1.15x10^{18} cm^2, 150°C) subsequently implanted with high- or low-energy Si ions. The presence of tensile strain is apparent in samples with no additional Si implantation (Fig. 5.2(a)) and the low χ_{min} value over depths of 0-0.9 μm in the channeled RBS spectra of Fig. 5.2(b) indicates a dislocation-free Si overlayer. (At such implant temperatures, dislocation formation occurred between doses of 1.15-1.3x10^{18} cm^{-2}.)

Following high-energy Si implantation (4.2 MeV, 6x10^{16} cm^{-2}, 150°C) where the Si-ion R_p is several times greater than the depth of the buried SiO_2 layer, strain relaxation is evident from DCXRD analysis. In Fig 5.2(c), the strain maximum of the RC has moved to ~500 arcsec from the ~750 arcsec seen in the samples prior to Si irradiation (Fig. 5.2(a)). As expected, in the RBS/C spectra of Fig. 5.2(d), an increased χ_{min} value within the Si overlayer is evident and indicates dislocation formation.

Following low-energy Si implantation (0.1 MeV, 3x10^{15} cm^{-2}, 150°C), where the Si R_p falls within the Si overlayer, strain reduction in the near-surface region is evident. The strain peak height at ~300 arcsec in the sample prior to Si irradiation has decreased (see Figure 5.1(e)) and a new strain peak at ~125 arcsec is observed. RADS simulations of the sample prior to Si irradiation indicate that the RC peak at ~300 arcsec is the result of strain located in the first 0.4 μm of the sample. (For reference, Fig. 4.3(a) shows the

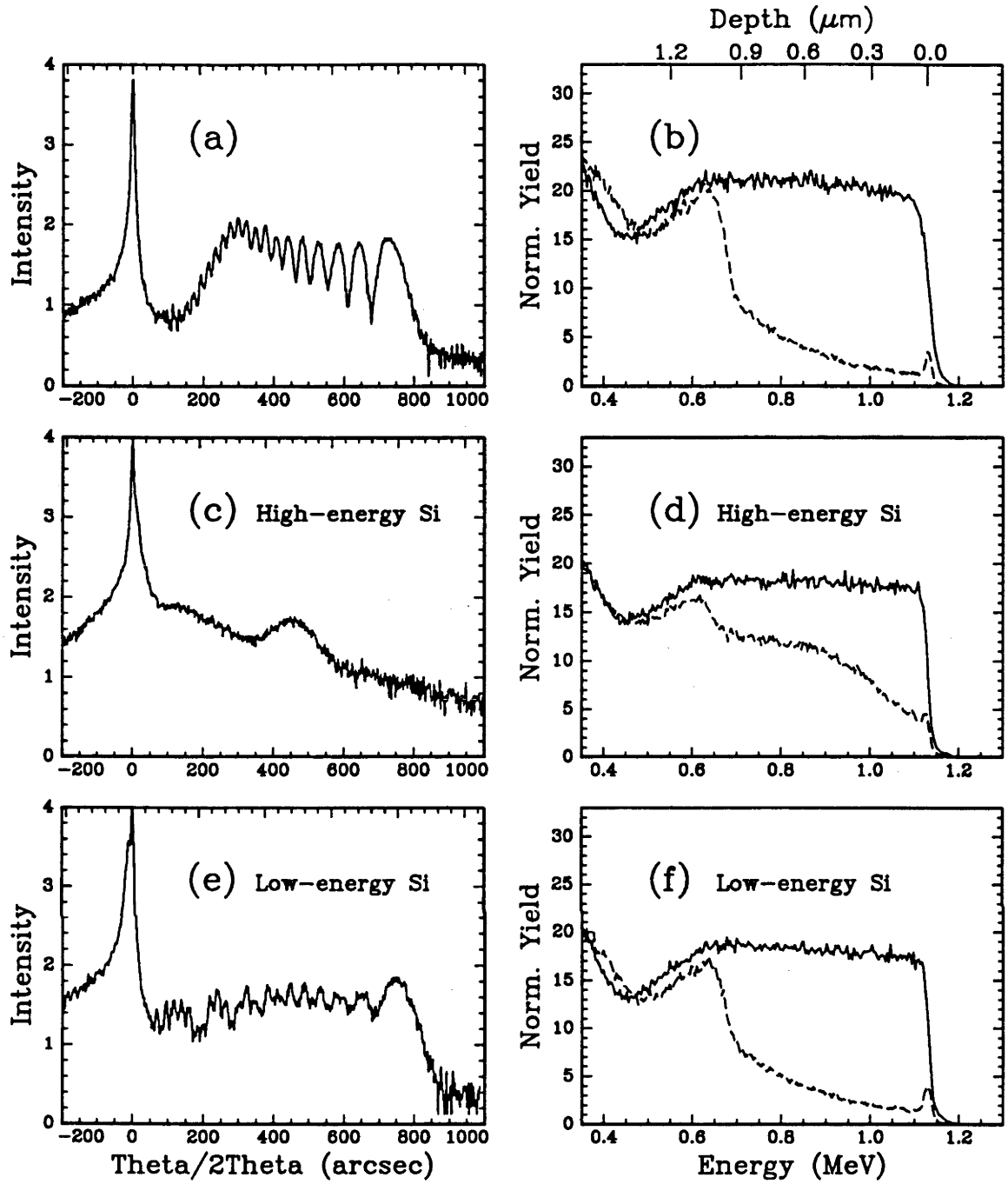

Figure 5.2: DCXRD and RBS/C spectra, respectively, of O-implanted Si (1 MeV, 1.15x10^{18} cm^{-2}, 150°C) with:
(a),(b) no additional implant,
(c),(d) an additional Si implant (4.2 MeV, 4x10^{16} cm^{-2}, 150°C),
(e),(f) an additional Si implant (100 keV, 3x10^{15} cm^{-2}, 150°C).
The RBS/C spectra were obtained 2 MeV He^{+} ions.
(———) Random (-------) Channeled

experimental and simulated RC for a similar sample of O-implanted Si (1 MeV, $1x10^{18}$ cm^{-2}, 150°C).) After low-energy Si implantation, the reduced height of the peak at 300 arcsec in conjunction with the new peak at ~125 arcsec suggest strain reduction within the first ~0.4 μm of the sample. As expected, the maximum tensile strain (~750 arcsec) is not influenced by the low-energy Si implant since this strain is located at depths > Si-ion R_p. Slight damage from the low-energy Si implantation is evident in the RBS/C spectra (Figure 5.2(f)) by a small peak in the channeled RBS spectra at ~0.15 μm. Otherwise, no increase in the χ_{min} value over the extent of the Si overlayer (0-0.9 μm) is observed indicating there was no dislocation formation after the low-energy Si implant.

5.1.2 Dependence of Strain Reduction on Si Dose and Implant Temperature

To further explore the mechanisms of strain reduction with low-energy Si implantation, O-implanted Si was subsequently implanted with 100 keV Si ions at various implant temperatures and doses. Figure 5.3 shows the RBS/C spectra of O-implanted Si (1 MeV, $1.1x10^{18}$ cm^{-2}, 150°C) which was subsequently implanted with 100 keV Si ions at 150°C to doses between $0.9\text{-}13x10^{15}$ cm^{-2}. Damage in the near-surface region is evident by the increased surface peak area of the channeled spectra after Si implantation to a dose of $9x10^{14}$ cm^{-2}. As the dose is increased to $4x10^{15}$ cm^{-2}, there is still no damage evident near the Si R_p but the surface peak area is further increased. At a dose of $1.3x10^{16}$ cm^{-2}, a direct scatter peak at ~0.8 Si R_p is apparent in the channeled spectrum with a much increased χ_{min} value evident at greater depths due to dechanneling.

Figure 5.4 shows the DCXRD spectra for these samples. As previously explained, the peak at ~350 arcsec prior to Si irradiation is due to strain located in the first ~0.4 μm. The extent of strain reduction at such depths increases with Si dose up to a dose of $1.3x10^{16}$ cm^{-2}. Implantation to higher doses (not shown) does not reduce the strain any further. Thus, strain relaxation due to low-energy Si implantation increases (and eventually saturates) with dose. It is important to note that after low-dose Si implantation (100 keV, $4x10^{15}$ cm^{-2}, 150°C), strain reduction is apparent without dislocation formation. In contrast, after high-dose Si implantation (100 keV, $1.3x10^{16}$ cm^{-2}, 150°C), dislocation formation as evident in the RBS/C spectra by a direct scatter peak at ~ 0.2 μm appears to be the cause of further strain relaxation.

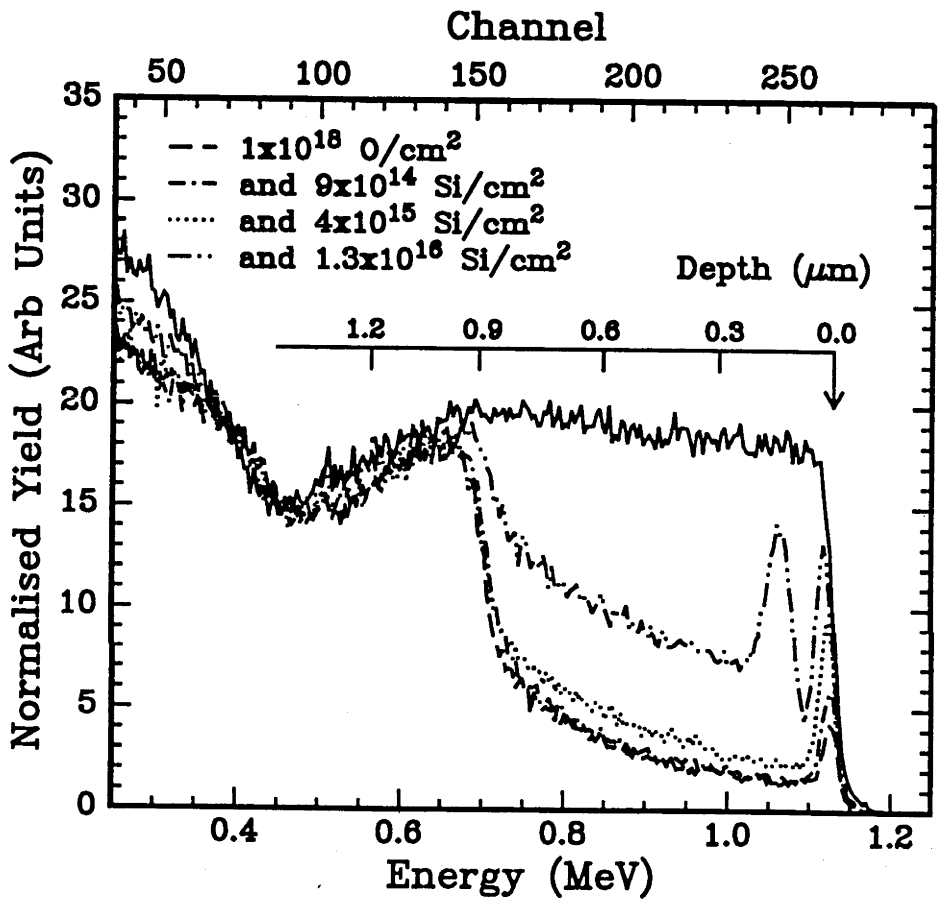

Figure 5.3: RBS/C spectra (obtained with 2 MeV He^+ ions) of O-implanted Si (1 MeV, 1.1x10^{18} cm^{-2}, 150°C) with an additional Si implant (100 keV, 0.9-13x10^{15} cm^{-2}, 150°C).

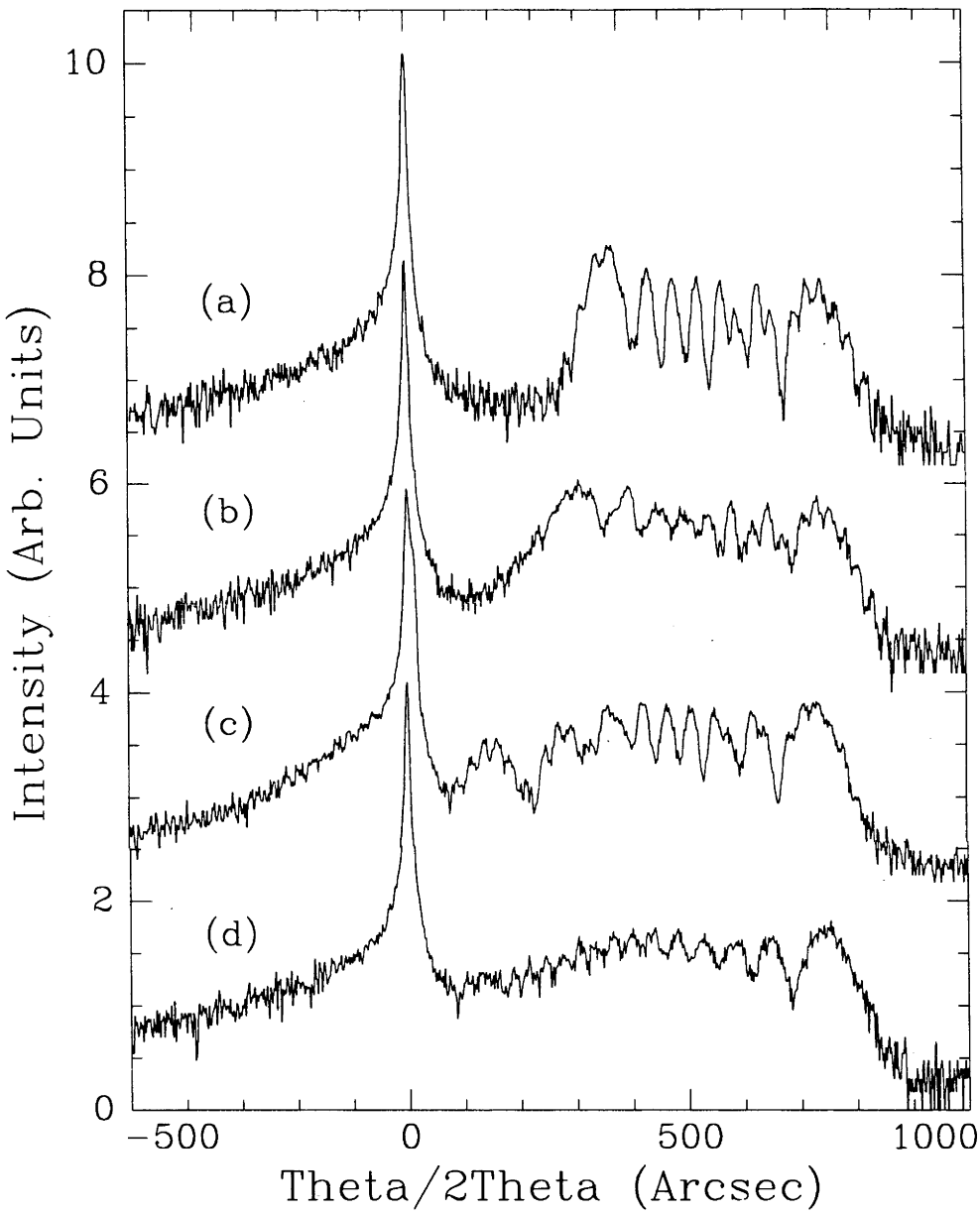

Figure 5.4: DCXRD spectra of O-implanted Si (1 MeV, 1.1x10^{18} cm^{-2}, 150°C) with : (a) no additional Si implant, (b) an additional Si implant (100 keV, 9x10^{14} cm^{-2}, 150°C), (c) an additional Si implant (100 keV, 4x10^{15} cm^{-2}, 150°C), (d) an additional Si implant (100 keV, 1.3x10^{16} cm^{-2}, 150°C).

The damage and strain relaxation in these samples is also a function of Si implant temperature. Figure 5.5 shows the RBS/C spectra of O-implanted Si (1 MeV, $1.1x10^{18}$ cm^{-2}, 150°C) following an additional 100 keV Si implant to a dose of $4x10^{15}$ cm^{-2} at various Si implant temperatures. Amorphous layer formation over 0-0.15 μm is evident for implant temperatures of -150 (not shown) and 30°C. Dynamic annealing at higher implant temperatures inhibited amorphous layer formation. An increase in the surface peak area is apparent for Si implantation performed at 150°C, while for the 300°C implant, no significant changes to the RBS/C spectra are evident.

Figure 5.6 shows the DCXRD spectra of these samples. At the low implant temperature of 30°C, a slight reduction in the peak height at ~350 arcsec is evident. For elevated temperature implantation (150 and 300°C) a more significant reduction in peak height is evident and a new peak has appeared at ~150 arcsec, indicating strain reduction in the near-surface region. Increased implant temperatures allow defect migration to areas of greater strain and relaxation is enhanced. O-implanted Si (1 MeV, $1.1x10^{18}$ cm^{-2}, 150°C) which was annealed at 300°C for 30 minutes did not show any reduction in strain indicating that it is ion-atom interactions during the secondary Si implant rather than annealing during implantation which is responsible for the observed changes to the strain profiles in the Si-implanted samples.

5.1.3 Discussion

Si implantation into strained O-implanted Si can contribute to changes in strain within the Si overlayer through either increasing (high-energy Si ions) or decreasing (low-energy Si ions) the local vacancy excess. In samples implanted with O only, the increase in O dose from 1.15 to $1.3x10^{18}$ cm^{-2} resulted in strain relaxation/dislocation formation within the Si overlayer due to the greater excess vacancy concentration and consequent higher strain which results at the higher dose. When the yield stress is exceeded, dislocation loops form to relieve the strain. As expected, an increased χ_{min} value within the Si overlayer is evident after high-energy Si implantation in all O-implanted Si samples (1 MeV, $1\text{-}21x10^{17}$ cm^{-2}, 150°C) studied. The vacancy excess was increased throughout the Si overlayer (i.e. $<R_p$) resulting in increased strain and consequent dislocation formation. (With high-energy Si implantation, a negligible amount of the implanted atoms come to rest at depths within the Si overlayer.) The most pronounced effect was apparent in O-implanted Si (1 MeV, $1.15x10^{18}$ cm^{-2}, 150°C) because it was the most highly strained.

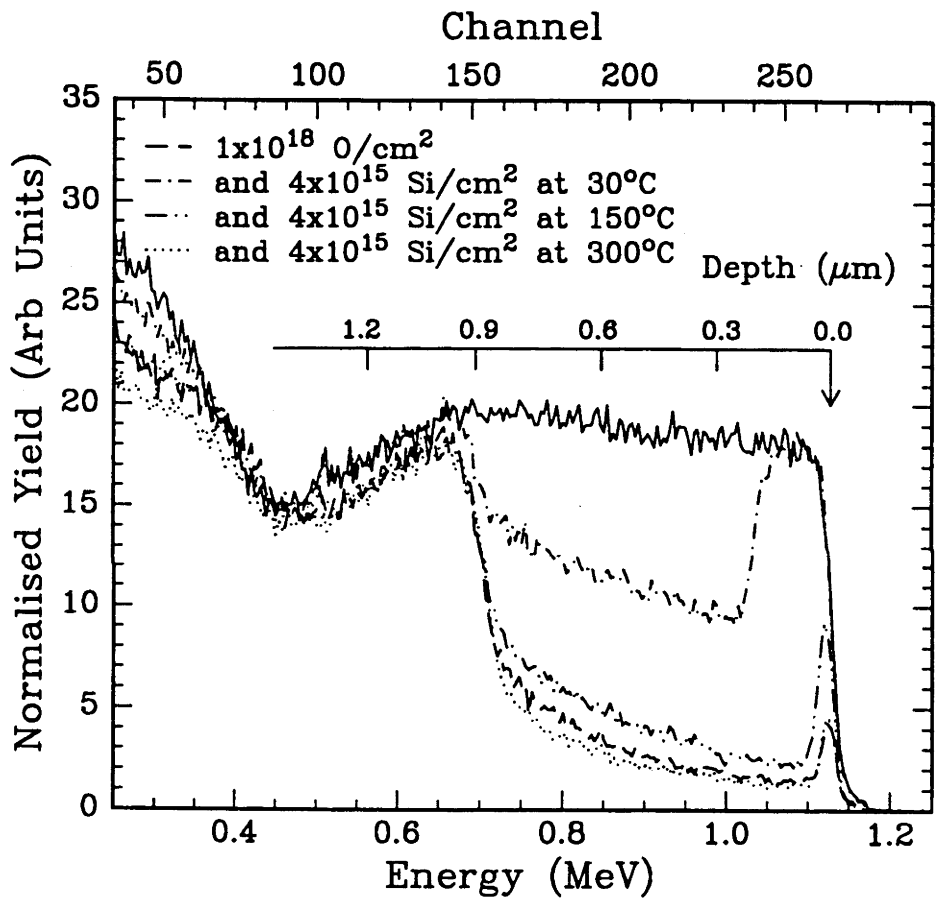

Figure 5.5: RBS/C spectra (obtained with 2 MeV He^+ ions) of O-implanted Si (1 MeV, $1.1x10^{18}$ cm^{-2}, 150°C) with an additional Si implant (100 keV, $4x10^{15}$ cm^{-2}, 30-300°C).

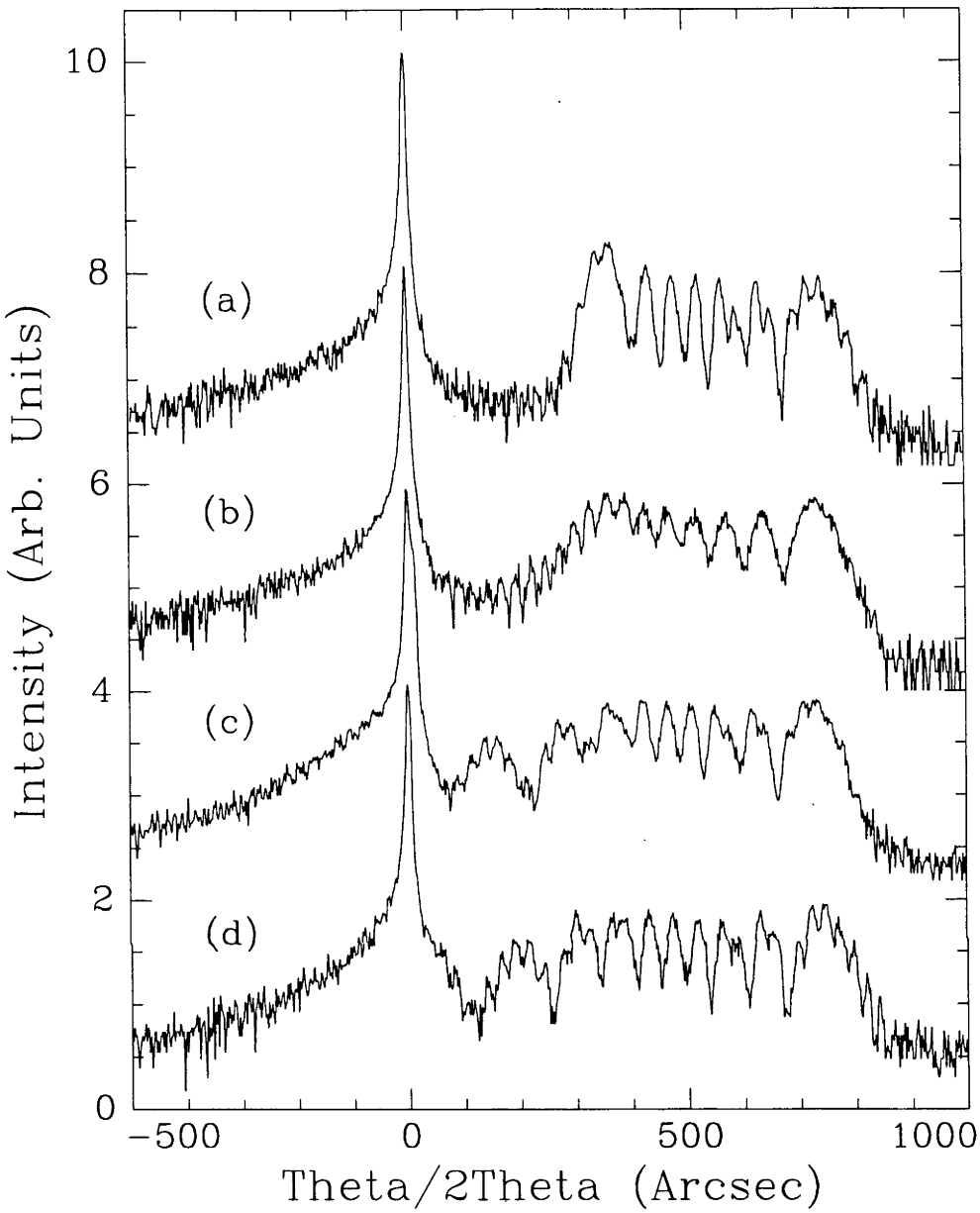

Figure 5.6: DCXRD spectra of O-implanted Si (1 MeV, 1.1x10^{18} cm^{-2}, 150°C) with : (a) no additional Si implant, (b) an additional Si implant (100 keV, 4x10^{15} cm^{-2}, 30°C), (c) an additional Si implant (100 keV, 4x10^{15} cm^{-2}, 150°C), (d) an additional Si implant (100 keV, 4x10^{15} cm^{-2}, 300°C).

In contrast to high-energy Si implantation, low-energy Si implantation in O-implanted Si introduces excess interstitials into the Si overlayer since R_p=0.15 μm. In the near-surface region, implanted Si atoms and excess interstitials compensate the O implantation-induced vacancy excess at this depth. The nature of the disorder following low-energy Si implantation compared with high-energy O implantation may also contribute to the observed strain reduction. No change in χ_{min} was evident (other than the slight increase in the channeled yield near the Si R_p) for any low-energy Si implantation to doses 0.9-13x10^{15} Si/cm^2 and strain within the near-surface region was reduced in all O-implanted Si samples.

Additional studies of low-energy Si implantation at various doses and implant temperatures indicate that both the number of interstitials and the migration of these defects to strained regions affect strain reduction. The athermal number of interstitials produced during implantation increases with dose. Since compensation of the vacancy excess by such interstitials (and the implanted atoms) is responsible for the observed strain reduction, an increase in strain reduction with dose is expected and is consistent with observation. The saturation of this effect is the result of dislocation formation at doses $\geq$ 1.3x10^{16} cm^{-2} due to end-of-range damage from the Si implantation.

Interstitial migration to strained regions is evident from Si implant temperature studies. At low implant temperatures, increased damage over the depths of Si implantation was the dominant effect and minimal strain reduction was detected. Strain relaxation at depths away from the implanted atom/interstitial excess (at depths greater than ~ R_p+2*straggle), therefore, requires the migration of interstitials to such regions. The observed strain reduction for Si-implanted samples at high implant temperatures (150 and 300°C) is consistent with such migration and is the result of increased point defect mobility at higher temperatures. However, the strain reduction is still quite localised, presumably because the finite number of Si interstitials created from the secondary Si implant find recombination sites (vacancies) spatially close to where they are produced.

In order to decrease the strain in these samples even further, excess interstitials must be created throughout depths of strain in the Si overlayer. Hence, higher Si implant energies would be required to span the Si overlayer, and the dose scaled to produce an excess interstitial and implanted atom concentration that would compensate for the O implantation-induced strain. In recent experiments, Holland[113] studied the effect of the dose of a secondary Si implant (150 keV, various doses, 450°C) in both virgin Si and Si pre-damaged with O implantation (500 keV, 0.8x10^{18} cm^{-2}, 530°C). RBS/C measurements indicated *less* damage after a secondary Si implant in

O-implanted substrates as compared to virgin Si. As the dose of the secondary Si implant was increased, the extent of damage reduction decreased presumably since the interstitial concentration resulting from the Si implant was greater than necessary to compensate the vacancy excess from the O implant.

5.2 Si-Implantation into Strain-Relaxed O-implanted Si

As demonstrated in the previous section, strain within the Si overlayer of O-implanted Si can be reduced with a secondary Si implant performed under appropriate conditions. However, in single-implant and anneal material, at the dose required for a thick buried SiO_2 layer, strain relaxation has already occurred. If the damage within the Si overlayer of such material could be reduced to yield acceptable defect densities upon annealing, both the time and cost of SIMOX material fabrication could be minimised. Consequently, high-energy Si irradiation of unannealed high-dose O-implanted Si was studied with the aim of reducing post-anneal disorder.

High-energy Si ions (with Si R_p > O R_p) were implanted in unannealed, strain-relaxed O-implanted Si and the microstructure before and after Si implantation was examined. The starting material for this experiment was O-implanted Si (1 MeV, 2.18×10^{18} cm^{-2}, 150°C) fabricated with a current density of 9 $\mu A/cm^2$. During O implantation, the sample was clamped to the target holder and no Ag paint was used. Hence, the actual implant temperature is estimated to be between 225 and 300°C. A second implantation of 4.2 MeV Si ions (R_p~3.2 μm) was subsequently performed at 150°C to doses of 5×10^{15}, 1×10^{16}, 5×10^{16} and 1×10^{17} cm^{-2}. The current density for Si implantation was 6.25 $\mu A/cm^2$.

5.2.1 Dependence of Damage Microstructure on Si Dose

5.2.1a Pre-anneal Microstructure

Figure 5.7 shows the RBS/C spectra of O-implanted Si which has been subsequently implanted with 4.2 MeV Si ions at 150°C to various doses (5×10^{15}-1×10^{17} cm^{-2}). It is apparent that the extent of damage in the Si overlayer (as

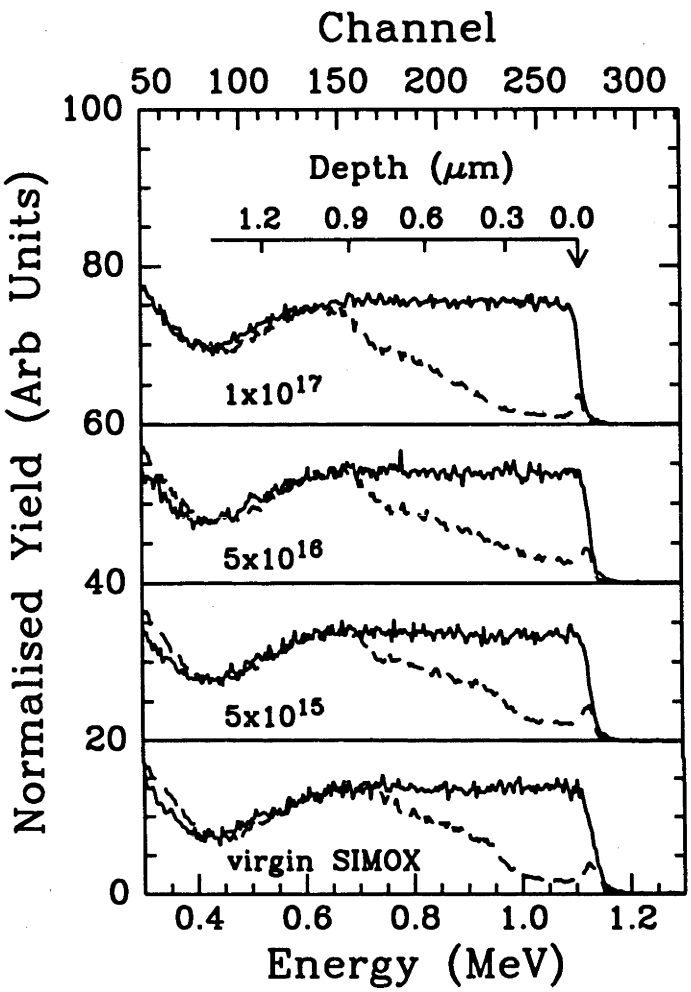

Figure 5.7: RBS/C spectra (obtained with 2 MeV He^+ ions) of O-implanted Si (1 MeV, 2.18x10^{18} cm^{-2}, 150°C) implanted additionally with Si ions (4.2 MeV, 5x10^{15} - 1x10^{17} cm^{-2}, 150°C). Si doses (cm^{-2}) are indicated below the spectra. (——) Random (-----) Channeled.

measured by χ_{min}) is dose dependent. A rapid dechanneling at ~0.35 μm in the RBS/C spectrum of the virgin SIMOX sample (i.e. no additional Si implantation) indicates damage formation and strain-relaxation. At ~0.95 μm, amorphous layer formation is apparent. For the lowest doses of $5x10^{15}$ and $1x10^{16}$ Si/cm^2 (not shown), the onset of dechanneling begins at ~0.3 and ~0.2 μm, respectively, indicating more extensive damage formation and further strain relaxation as the Si dose is increased. For doses $\geq 5x10^{15}$ cm^{-2}, the amorphous layer width decreases with increasing Si dose indicating ion beam annealing (IBA) has occurred.

For a dose of $5x10^{15}$ Si/cm^2, the implantation time was 160 seconds. As previously noted, the equilibrium temperature during implantation is reached within 45 seconds. Thus, even for the lowest dose, the majority of implant time was spent at or near the equilibrium temperature. Consequently, the change in damage with dose is not due to temperature increases which may have occurred during implantation.

5.2.1b Post-anneal Microstructure

Following implantation, samples were capped with ~0.5 μm of plasma-deposited SiO_2 then annealed at 1300°C for 2 hours in an Ar+3%O atmosphere. The SiO_2 cap was removed after annealing and before characterisation. Figure 5.8 shows RBS/C spectra of Si-implanted SIMOX material after annealing for various Si doses. The influence of dose on the secondary defect structure is evident. In RBS/C measurements, this influence manifests itself in the height and slope of the damage peak at the front SiO_2/Si interface (~0.8 μm). In the virgin SIMOX material, the presence of randomly oriented polySi (as verified by XTEM) is evidenced by a damage peak (with a yield equal to that of randomly oriented Si) in the channeling spectrum bordering the front Si/SiO_2 interface. In comparison, all Si-implanted SIMOX samples have lower damage peak heights at this depth. In these samples, reduced χ_{min} values throughout the Si overlayer are also apparent with the highest Si doses having χ_{min} values equal to that of virgin Si. The apparent reduction in the direct scattering contribution to the damage peak height at the front Si/SiO_2 interface is consistent with a reduction in the polySi volume fraction[114] (as shown in the XTEM micrographs in Fig. 5.9).

XTEM was performed on selected annealed samples. Figure 5.9 shows micrographs of annealed (a) virgin SIMOX material and (b) Si-implanted SIMOX material (4.2 MeV, $5x10^{16}$ Si/cm^2, 150°C). The difference between the two damage structures is clearly evident. The virgin SIMOX material has a thin layer of microtwins separating the Si overlayer and the polySi. The high contrast in the polySi is due to the

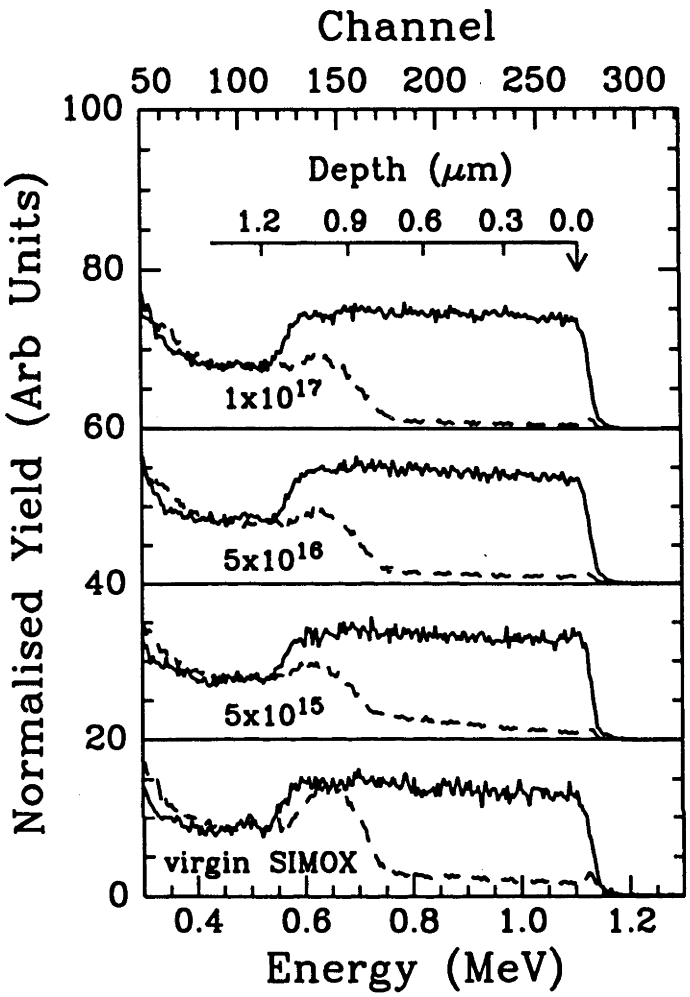

Figure 5.8: RBS/C spectra (obtained with 2 MeV He^+ ions) of O-implanted Si (1 MeV, 2.18x10^{18} cm^{-2}, 150°C) implanted additionally with Si ions (4.2 MeV, 5x10^{15} - 1x10^{17} cm^{-2}, 150°C). These samples have been annealed at 1300°C for 2 hours. The Si dose (cm^{-2}) is denoted beneath the spectra. (——) Random (-----) Channeled.

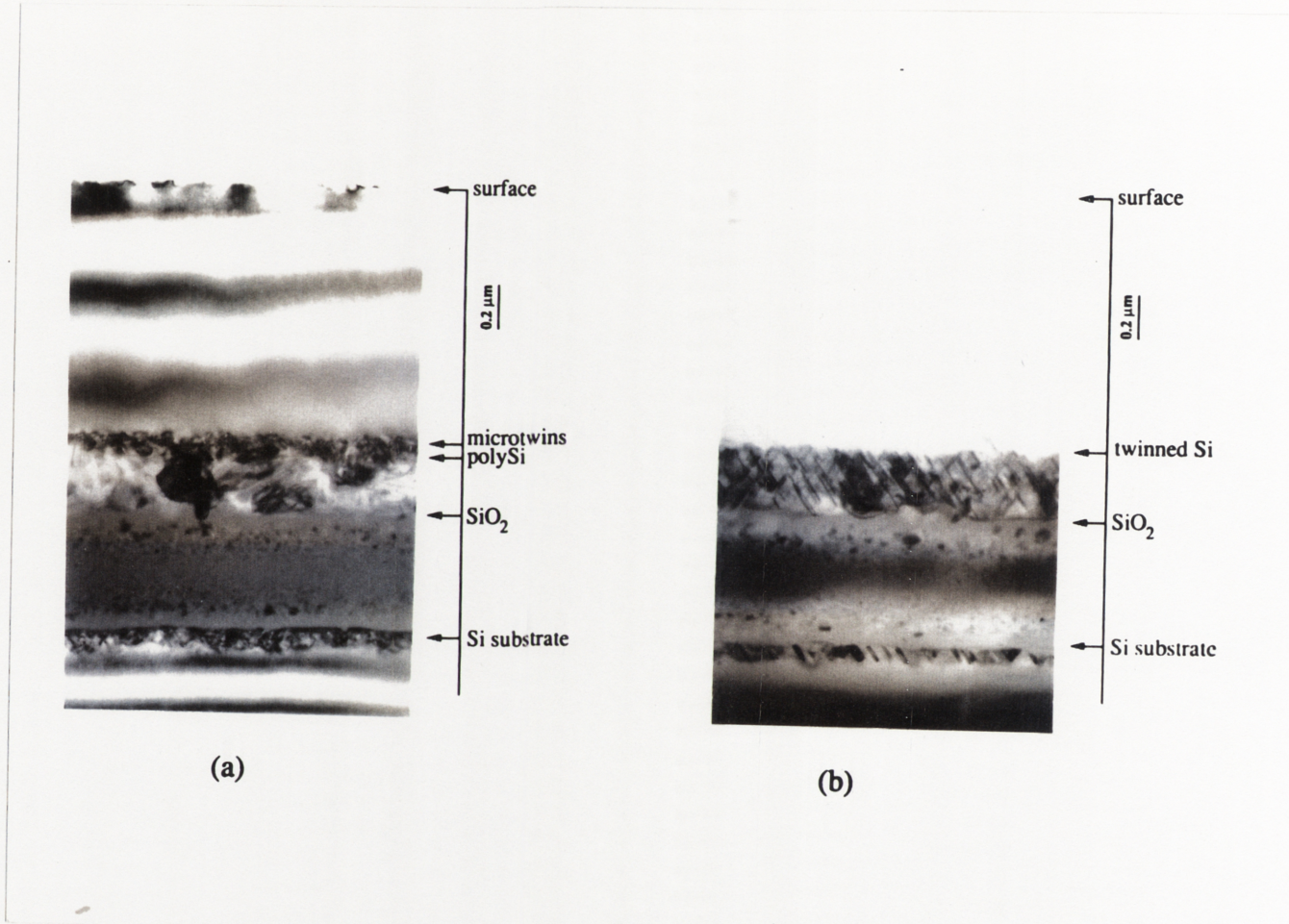

Figure 5.9: XTEM micrographs of annealed (1300°C, 2 hours) (a) virgin SIMOX material (b) virgin SIMOX after an additional Si implantation (4.2 MeV, $5x10^{16}$ cm^{-2}, 150°C). The samples were oriented 2° off the [110] orientation during XTEM analysis.

random orientations of the grains. Bands evident in the polySi indicate twinning within individual grains. The buried SiO_2 layer contains several small, twinned Si inclusions and a thin layer of microtwins borders the back Si/SiO_2 interface. The Si-implanted SIMOX sample shown is representative of all annealed material examined by XTEM wherein twinning at the front Si/SiO_2 interface is the dominant defect.

Selected area diffraction analysis (shown in Figure 5.10) near the front Si/SiO_2 interface further indicates that in virgin SIMOX, the front Si/SiO_2 interface is bordered by randomly oriented polySi while in the Si-implanted SIMOX, (111) type twinning borders this interface. For the other Si-implanted SIMOX samples analysed by XTEM, the polySi volume fraction was similar to the Si-implanted SIMOX material (4.2 MeV, $5x10^{16}$ Si/cm^2, 150°C) and was much smaller than the polySi volume fraction in virgin SIMOX material. The SiO_2 layer and the back Si/SiO_2 interface have not been noticeably affected by the Si implant.

5.2.2 Dependence of Damage Microstructure on Si Implant Energy

To clarify whether the microstructural changes in annealed Si-implanted SIMOX are due to long- or short-range effects, Si implantation was performed at two different energies. The same virgin SIMOX material was implanted with Si at (1 MeV, $3x10^{15}$ cm^{-2}, 150°C) and (4.2 MeV, $5x10^{16}$ cm^{-2}, 150°C). The Si and O ion energy, range, dose and dose rates are shown in Table II. The dose rates for (b) and (c) are dissimilar purely as a result of experimental expediency.

Sample	Ion and Energy	Ion Range (μm)	Dose (cm^{-2})	Dose Rate (cm^{-2}/sec)
(a)	1.0 MeV O	1.31	$2.18x10^{18}$	$6.2x10^{13}$
(b)	1.0 MeV Si	1.31	$3x10^{15}$	$1.3x10^{13}$
(c)	4.2 MeV Si	3.24	$5x10^{16}$	$3.9x10^{13}$

Table II: Si and O ion energy, range, dose and dose rates.

(a)

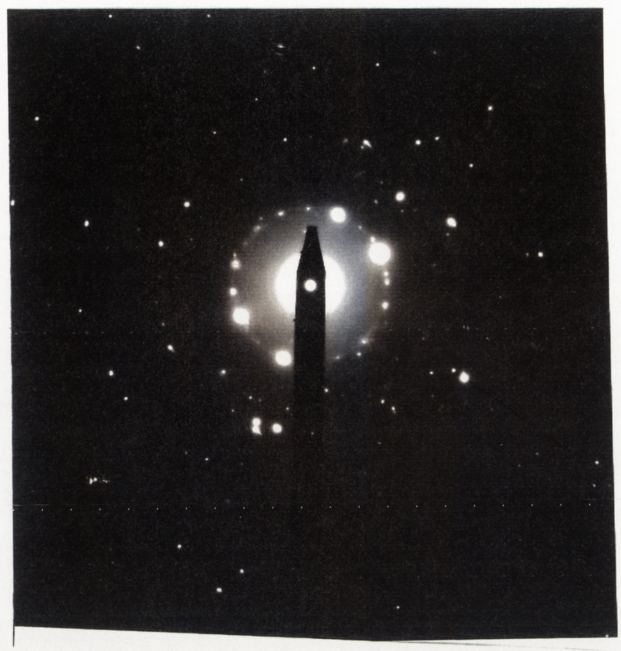

(b)

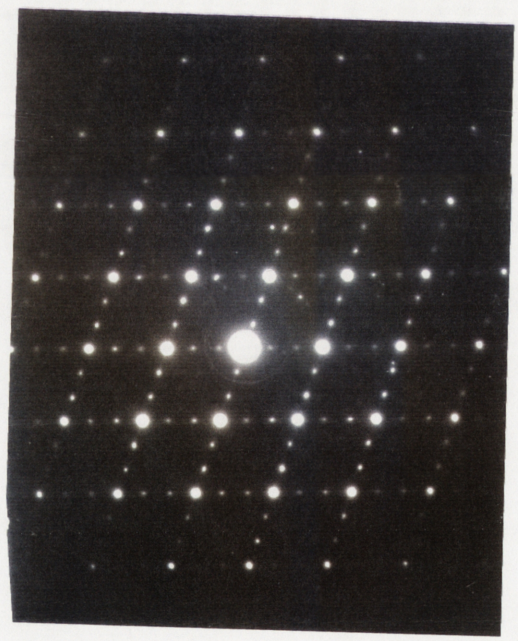

Figure 5.10: Diffraction patterns of annealed (1300°C/2 hours): (a) virgin SIMOX material, (b) virgin SIMOX after an additional Si implantation (4.2 MeV, $5x10^{16}$ Si/cm^2, 150°C). The samples were oriented in the [110] orientation during XTEM analysis.

Figure 5.11 shows the RBS/C spectra of virgin SIMOX material that was implanted with: (a) no additional Si implant, (b) Si ions (1 MeV, $3x10^{15}$ cm^{-2}, 150°C) and (c) Si ions (4.2 MeV, $5x10^{16}$ cm^{-2}, 150°C). As expected, the extent of dislocation formation (and hence strain relaxation) evident by dechanneling in the RBS/C spectra of SIMOX material is greater in Si-irradiated material. IBA at the a/c interface is evident in both Si-irradiated samples, with the sample (1 MeV, $3x10^{15}$ cm^{-2}, 150°C) exhibiting the greatest degree of IBA. Since the high-energy Si implantation most likely resulted in a higher actual implant temperature, it might be expected that the rate of IBA would be higher in this sample. However, the dose rate for this implant was ~ 3 times higher than the 1.0 MeV Si implant. It has been shown that increased dose rates increase the reversal temperature (T_R). The value ($T_{implantation}$-T_R) indicates the recrystallisation or amorphisation rate.[115] (When $T>T_R$, recrystallisation occurs and when $T<T_R$, amorphisation occurs.)

Figure 5.12 is the RBS/C spectra of annealed (1300°C/2 hours) SIMOX material which was implanted with: (a) no additional Si implant, (b) Si ions (1 MeV, $3x10^{15}$ cm^{-2}, 150°C) and (c) Si ions (4.2 MeV, $5x10^{16}$ cm^{-2}, 150°C). The height of the residual damage peak near the front Si/SiO_2 interface varies widely from sample to sample. As previously demonstrated, lower peak heights indicate a higher fraction of twinned material while higher peak heights indicate a higher fraction of polySi. While the damage peak height has decreased in both Si-irradiated samples, the biggest reduction in polySi volume formation was evident in the high-energy Si-implanted SIMOX material (4.2 MeV, $5x10^{16}$ cm^{-2}, 150°C).

5.2.3 Discussion

The study of microstructural improvements to SIMOX material after Si implantation and subsequent annealing at various energies indicated the change was not the result of the gettering of point defects to damage at the Si R_p as previously demonstrated in with B- and As-implanted Si.[111,112] In particular, once the buried SiO_2 layer has formed, interstitial Si within the Si overlayer cannot be readily gettered by the deep Si damage due to the extremely low diffusivity of Si in SiO_2.[116] As well, Si interstitials are far more likely to be consumed by the dislocations that have already formed due to strain relaxation. The possibility that residual crystallites within the amorphous layer are facilitating polySi formation over twinned Si has been discounted since polySi formation upon annealing is not suppressed by further amorphisation of the

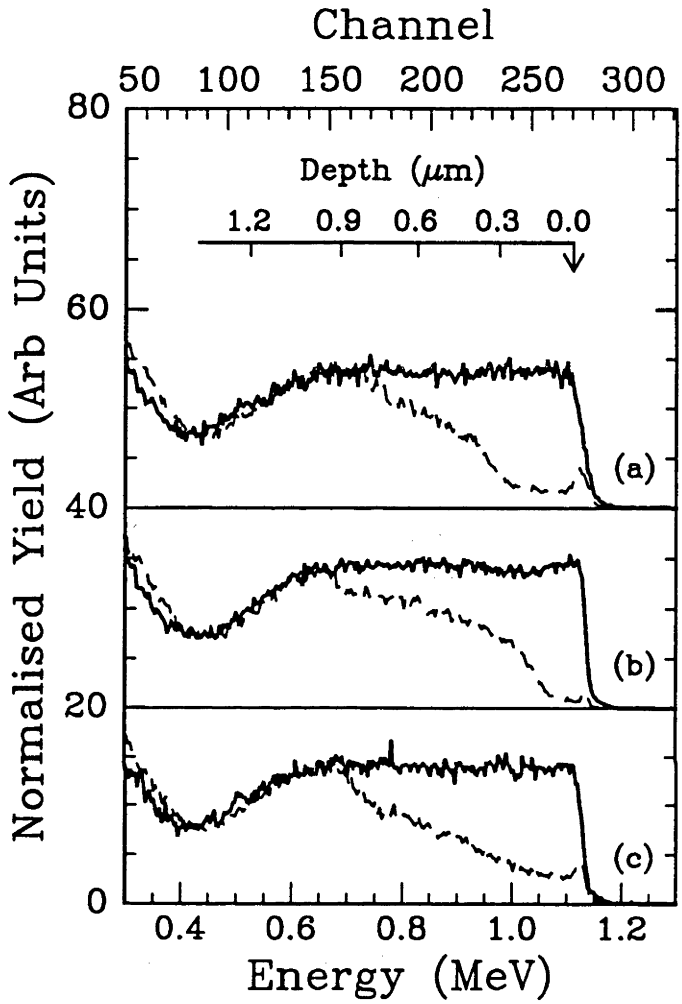

Figure 5.11: RBS/C spectra of unannealed virgin SIMOX implanted with (a) no additional Si implant, (b) Si ions (1 MeV, $3x10^{15}$ cm^{-2}, 150°C) and (c) Si ions (4.2 MeV, $5x10^{16}$ cm^{-2}, 150°C).
(——) Random (-----) Channeled.

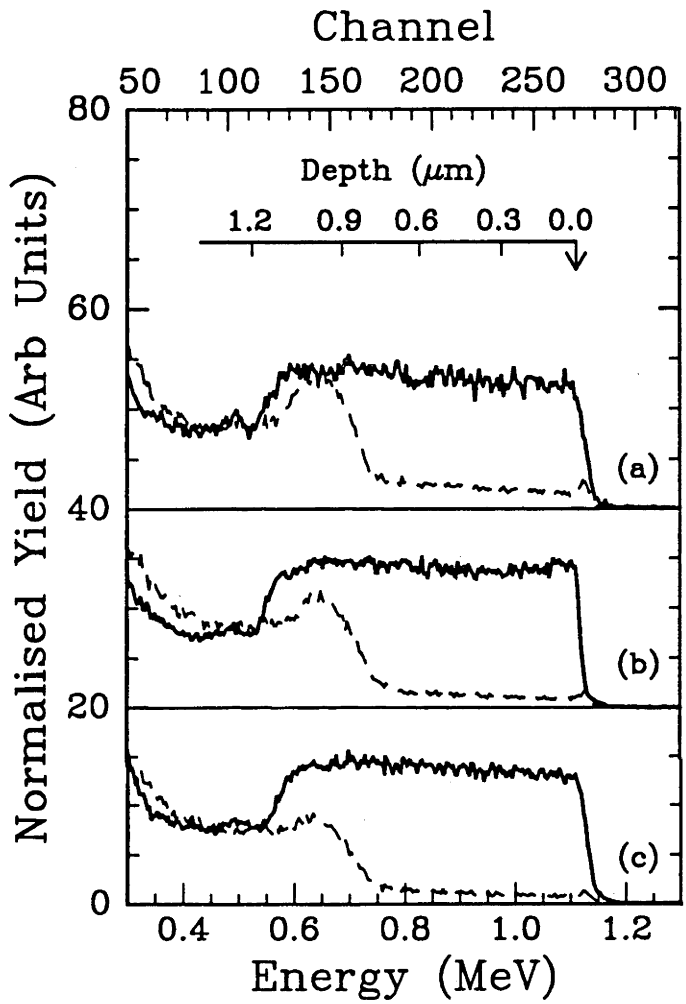

Figure 5.12: RBS/C spectra of annealed (1300°C/2 hours) virgin SIMOX implanted with (a) no additional Si implant, (b) Si ions (1 MeV, $3x10^{15}$ cm^{-2}, 150°C) and (c) Si ions (4.2 MeV, $5x10^{16}$ cm^{-2}, 150°C).
(——) Random (-----) Channeled.

Si overlayer. Consequently, it appears that the effects of IBA during Si irradiation are responsible for the microstructural improvement.

As previously described in section 3.1.4, competition between RNG and SPE determines the final microstructure bordering the SiO_2 layer. The SPE process was presumed completed before high annealing temperatures were reached, i.e. before RNG mechanisms began to dominate. The Si ion beam must therefore affect the damage in unannealed Si-implanted SIMOX samples in a way that promotes SPE. For example, ion-atom interactions that assist in the bond-breaking process necessary for epitaxy to proceed would have such an effect. Also, increased a/c interface planarity provides a better seed for recrystallisation and hence promotes SPE. An increase in the planarity of the a/c interface after IBA was previously reported.[117]

A more likely explanation comes from earlier reports where it was shown that IBA of O-containing a-Si was more successful at suppressing polySi formation than thermal annealing.[118] During thermal annealing the formation of polySi has been observed in a-Si when large O concentrations were present. In contrast, IBA causes "snow plowing" of O ahead of the a/c interface and hence minimises the effect of O in facilitating polySi formation during IBA. However, such "snow-plowing" would result in the pile-up of O at the a/c interface and consequently promote RNG during thermal annealing. However, IBA was also shown to promote O diffusion in a-Si.[118] Si irradiation at elevated temperatures may also enhance the breakup of any $Si\text{-}O_x$ clusters that have formed, resulting in increased O mobility in the a-Si. These effects would aid epitaxial recrystallisation and suppress polySi formation upon thermal annealing. Further experiments are necessary to determine which mechanisms predominate.

5.3 Conclusions

The use of point defects to alter strain and hence dislocation formation in strained O-implanted Si was investigated. By varying the Si-ion energy, the depth of the resulting implanted-atom excess vacancy and interstitial concentrations can be altered and consequently the strain in the Si overlayer increased or decreased accordingly. Low-energy Si-ion implantation (Si R_p < O R_p) was shown to reduce strain where interstitials are introduced by the secondary implant; the compensation of the vacancy excess by such interstitials is responsible for the observed strain reduction. Conversely, high-energy Si-ion implantation (Si R_p > O R_p) was shown to result in

dislocation formation through increased strain and subsequent strain relaxation over the extent of the Si overlayer (i.e. over regions of increased excess vacancies). Such results support the idea that strain results from a vacancy excess within the Si overlayer.

The effect of the secondary Si implant temperature and dose was further investigated with the aim of finding the most favourable conditions for engineering point defect concentrations and hence reducing strain. Both the number of interstitials and the migration of these defects to strained regions were shown to affect strain reduction. For a given implant temperature, higher doses resulted in a higher concentration of interstitials and consequently greater strain reduction. The migration of interstitials generated by the Si implant to strained regions was also shown to be important since the higher point defect mobility at increased implant temperatures further promoted strain reduction.

The related study of secondary Si-ion implantation in strain-relaxed O-implanted Si demonstrated that such an implant can be used to improve the crystallinity of the Si adjacent to the front Si/SiO_2 interface in annealed samples. Si irradiation in unannealed O-implanted Si (where Si R_p> O R_p and also where Si R_p= O R_p) was shown to promote epitaxial regrowth at the front a/c interface under implant conditions where IBA was observed. The several mechanisms which may be operating include a "snow-plowing" of any O present ahead of the a/c interface during IBA, increased O mobility in the a-Si and the break up of any Si-O_x complexes which have formed during O implantation. Since O impedes SPE, the movement of O away from regions of epitaxial regrowth allows more uniform recrystallisation to proceed. Consequently, the latter two mechanisms are more likely to inhibit RNG and thus reduce the polySi volume fraction at the front a/c interface. The increased a/c interface planarity which potentially results from IBA has also been shown to promote SPE. Further experiments are necessary to determine which mechanism is primarily responsible for the improved microstructure after Si-ion implantation.

Chapter 6

Summary and Conclusions

6.0 Summary and Conclusions

The formation of SIMOX material by MeV O-ion implantation has been reported. Studies of the post anneal microstructure at various implant temperatures showed that SIMOX material formed at high implant temperatures (300 and 450°C) resulted in a microstructure similar to that of SIMOX material fabricated at conventional (~200 keV) energies. Significant concentrations of Si and SiO_2 precipitates in the buried SiO_2 layer and Si overlayer, respectively, were evident. In contrast, low temperature implantation (150°C) resulted in no SiO_2 precipitation within the Si overlayer, twinned regions at the front Si/SiO_2 interface, and a more homogeneous buried SiO_2 layer. Most importantly, it was demonstrated that implant temperatures as low as 150°C can be used for SIMOX fabrication without total amorphisation of the Si overlayer.

The ability to fabricate SIMOX material by MeV implantation with lower nuclear energy deposition density throughout the Si overlayer and an extended implant temperature range lends itself to a single implant and anneal process whereby low defect-density SIMOX material can be produced. As well, the thicker Si overlayer that results from high-energy implantation may be useful for novel device designs such as 3D circuits.

The O dose utilised for MeV implantation in Si is also an important parameter in SIMOX production. A significant increase in damage within the Si overlayer with dose (over a dose range specific to each implant temperature studied) was evident. At doses above or below this range, a minimal increase in damage with dose was observed. In contrast, damage at the O-ion end-of-range is shown to continually increase with dose (over 0.3-2.18x10^{18} O/cm^2) for implant temperatures between 150 and 450°C, indicating two different mechanisms of damage formation near R_p and at depths < R_p.

The origin of the sudden onset of damage within the Si overlayer at a critical dose was attributed to strain relaxation within the Si overlayer. Strain measurements at doses below the critical dose showed the presence of tensile strain within the Si overlayer. This tensile strain was shown to increase with dose, until a critical dose was reached whereupon strain relaxation was observed. This tensile strain was shown to be the result of point defects, specifically vacancies, which result from the implantation process. Frenkel pairs created during implantation can become spatially separated (a component of the forward momentum of the primary ion-atom interaction is non-zero) and can lead to the development of local excesses of point defects over depths of implantation. Consequently, a local excess of interstitials is located at ~R_p whereas a vacancy excess is evident at depths less than R_p, i.e within the Si overlayer.

This is one of the first reports of an implantation-induced vacancy excess as detected by DCXRD measurements. The tensile strain at depths shallower than the R_p is not generally observed since ~0.01% of ion-atom and atom-atom contribute to the vacancy excess. Hence, implantation to high doses as well as implant conditions that inhibit dynamic annealing (low implant temperatures, for example) are necessary to observe this phenomenon. It should be noted that such phenomena was also evident in high-dose Si-implanted Si under implant conditions which resulted in the same vacancy production (as modeled by TRIM) within the Si overlayer as that of O-implanted Si. The relaxation of tensile strain was apparent for Si and O implantation at two different doses. However, the Si critical dose and the O critical dose produced the same athermal vacancy concentration within the Si overlayer, indicating chemical effects are minimal. It was further shown that in addition to atomic displacements, the presence of the high O concentration in the SIMOX process contributes to amorphous layer formation at R_p. However, within the Si overlayer the type and depth of defect formation were quite similar in O- and Si-implanted Si over the implant temperature range studied (150-450°C), again indicating that defect formation at depths <R_p is essentially independent of impurity concentration.

In both O- and Si-implanted Si, strain simulations show a tensile strain maximum at the same depth where dislocation formation occurred. As previously stated, the tensile strain increased with dose until strain relief through dislocation

formation. Studies of strain relaxation and dislocation formation at various implant temperatures provided further insight into the cause of these processes. In ion-implanted material, the strain at yield increased as the implant temperature decreased; this behaviour follows that of the flow stress in bulk Si as a function of temperature. Hence, the mechanism for yield in ion-implanted Si is simply strain accumulation until the yield strength of Si is exceeded. Strain accumulation in ion-implanted Si is dependent on implant conditions such as implant temperature, ion energy, dose rate, etc.

By utilising MeV implant energies, the yield strength of Si at temperatures below 400°C was characterised. This is the first report of Si yield strength at such temperatures. In the past, such studies were made by pulling on two ends of a bulk Si sample and consequently brittle failure occurred before flow stress was reached. As observed at temperatures of 400-1000°C, the yield strain increases as the temperature is decreased to 150°C. If strain accumulation is maintained at a minimum during implantation by using the appropriate implant conditions, lower implant temperatures should allow implantation to higher doses before strain relaxation occurs. As a consequence, the conventional three stage sequential implant and anneal process is potentially reducible to a two-step procedure through a reduction in implant temperature. This would aid in significantly reducing the cost of SIMOX material.

In ion-implanted material, the accumulation of strain is strongly process dependent. Several process parameters such as impurity concentration, implanted ion energy, mass, dose, dose rate and implant temperature will influence the strain in the material after implantation. If the accumulation of strain during implantation is controlled so the yield strain at a given implant temperature is never reached and dislocations are not formed, the post-anneal defect density in the Si overlayer will be low. Consequently, the management of strain through a secondary Si-ion implant in strained O-implanted Si was demonstrated. The introduction of vacancy or interstitial-type point defects at various depths in O-implanted Si was accomplished by varying the energy of the secondary Si implant. The strain in the Si overlayer was increased or decreased accordingly. Low-energy Si-ion implantation reduced strain at depths (~0.8 Si R_p) where interstitials were introduced by the secondary implant; the compensation of the vacancy excess by such interstitials is responsible for the observed strain reduction. Conversely, high-energy Si-ion implantation resulted in strain relaxation through dislocation formation over the extent of the Si overlayer (i.e. over regions of increased excess vacancy concentration.).

Strain reduction by low-energy Si implantation was further quantified by exploring the effect of Si implant temperature and dose on strain. The conditions that most efficiently reduced strains were high Si doses and high implant temperatures. The

increased dose creates a higher number of interstitials and the high implant temperature aids migration of these defects to regions of greater strain.

Finally, it was shown that a secondary Si-ion implant in strain-relaxed Si can be used to improve the crystallinity of the Si adjacent to the front Si/SiO_2 interface. Si irradiation in unannealed O-implanted Si (where Si R_p> O R_p and also where Si R_p= O R_p) was shown to promote epitaxial regrowth at the front a/c interface by IBA. The secondary Si implant promotes epitaxy at this interface through a combination of effects. Since O impedes solid phase epitaxy, by moving O away from regions of epitaxial regrowth, such regrowth can proceed more efficiently. IBA has been shown to enhance O mobility in a-Si. As well, the break up of $Si-O_x$ complexes by atom-ion interactions should free O for migration towards R_p, i.e. away from the a/c interface. Finally, increased a/c interface planarity, as potentially results from IBA, may also promote twinning over polySi formation. Further experiments are necessary to conclusively determine which mechanism is primarily responsible for the improved microstructure after Si-ion implantation. Specifically, the redistribution and mobility of O due to IBA should be further studied.

The results presented in this thesis have demonstrated the advantages of studying defect formation in SIMOX material formed by MeV implantation. The extended temperature range available for implantation allows the study of temperatures as low as 150°C which produce SIMOX material remarkably different than that fabricated at high implant temperatures. The increased range inherent to MeV energies also more clearly delineates the two different regions of damage, end-of-range damage and damage within the Si overlayer. The work presented in this thesis contributes to the understanding of damage formation in SIMOX material and suggests several novel methods for producing low defect density SIMOX material. Further studies are warranted in which the range of the secondary Si implantation in O-implanted Si is varied to achieve strain relaxation over the entire Si overlayer. As well, implantation of a specie other than Si would elucidate any contributions to strain reduction from chemical effects.

REFERENCES

1) G.K. Celler, "Silicon-on-Insulator Films by Oxygen Implantation and Lamp Annealing," *Solid State Tech.* **30**, no. 3, 93 (1987).

2) J-P. Colinge, Silicon-on-Insulator Technology: Materials to VLSI (Kluwer Academic Publishers, Boston, 1991) p. 9.

3) A. Gupta and P.K. Vasudev, "Recent Advances in Hetero-Epitaxial Si-on-Insulator Technology, Part II," *Solid State Tech.* **26**, no.6, 129 (1983).

4) A. Gupta and P.K. Vasudev, ", "Recent Advances in Hetero-Epitaxial Si-on-Insulator Technology, Part I," *Solid. State Tech.* **26**, no. 2, 104 (1983) .

5) K. Imai, "A New Dielectric Isolation Method Using Porous Silicon," *Solid State Electron.* **24**, 159 (1981).

6) J-P. Colinge, H.K. Hu and S. Peng, "Fabrication of Thin Silicon-on-Insulator Films Using Laser Recrystallisation," *Electron. Lett.* **21**, 1102 (1985).

7) R.C. McMahon, *Microelectron. Eng.* **8**, 255 (1988).

8) J.C.C. Fan, M.W. Geis and B.Y. Tsaur, "Lateral Epitaxy by Seeded Solidification for Growth of Single-Crystal Si Films on Insulators," *Appl. Phys. Lett.* **38**, 365 (1981).

9) W.P. Maszara, G. Goetz, A. Caviglia and J.B. McKitterick, "Bonding of Si Wafers for Silicon-on-Insulator," *J. Appl. Phys.* **64**, 4943 (1988).

10) W.P. Maszara, "Silicon-On-Insulator by Wafer Bonding: A Review", *J. Electrochem. Soc.* **138**, 341 (1991).

11) W.P. Maszara, P.P. Pronko and A.W. McCormick, "Epi-less Bond-and-Etch-Back Si-on-Insulator by MeV Ion Implantation," *Appl. Phys. Lett.* **58**, 2779 (1991).

12) D.J. Godbey, M.E. Twigg, H.L. Hughes, L.J. Palkuti, P. Leonov and J.J. Wong, "Fabrication of Bond and Etch-Back Silicon on Insulator Using a Strained $Si_{0.7}Ge_{0.3}$ Layer as an Etch Stop," *J. Electrochem. Soc.* **137**, 3219 (1990).

13) M. Watanabe and A. Tooi, "Formation of SiO_2 Films by Oxygen-Ion Bombardment," *Japan. J. Appl. Phys.* **5**, 737 (1966).

14) K. Izumi, M. Doken and H. Ariyoshi, "CMOS Devices Fabricated on Buried SiO_2 Layers Formed by O-implantation into Si," *Electron. Lett.* **14**, 593 (1978).

15) K. Izumi, Y. Omura, M. Ishikawa and E. Sano, "SIMOX Technology for CMOS/LSIs," *Tech. Digest of the Symp. on VLSI Tech.* 10 (1982).

16) J. Stoemenos, C. Jassaud, M. Bruel and J. Margail, "New Conditions for Synthesizing Si-on-Insulator Structures by High Dose O Implantation'" *J. Cryst. Growth* **73**, 546 (1985).

17) G.K. Cellar, P.L.F. Hemment, K.W. West and J.M. Gibson, "High Quality Si-on-SiO_2 Films by Large Dose O-implantation and Lamp Annealing," *Appl. Phys. Lett.* **48**, 532 (1986).

18) D. Hill, P. Fraundorf and G. Fraundorf, "The Reduction of Dislocations in O-implanted Si-on-Insulator Layers by Sequential Implantation and Annealing," *J. Appl. Phys.* **63**, 4933 (1988).

19) T.F. Cheek and D. Chen, "Dislocation Reduction on SIMOX Substrates by Using Multiple Implants," *Mater. Res. Soc. Symp. Proc.* **107**, 53 (1988).

20) A.J. Armani and S.N. Bunker, " Compound Formation Effects in Computing Implantation Profiles," *Mater. Sci. Eng.* **A114**, 67 (1989).

21) P.L.F. Hemment, "Silicon On Insulator Formed by O^+ or N^+ Ion Implantation," *Mater. Res. Soc. Symp. Proc.* **53**, 207 (1986).

22) M.I. Current in Ion Implantation Technology , edited by J.F. Zeigler (North-Holland, Amsterdam, 1992), p. 390.

23) J. Margail, J. Stoemenos, C. Jassaud and M. Bruel, "Reduced Defect Density in Silicon-on-Insulator Structures Formed by Oxygen Implantation in Two Steps," *Appl. Phys. Lett.* **54**, 526 (1989).

24) E.F. Kennedy, L. Csepregi, J.W. Mayer and T.W. Sigmon, "Influence of ^{16}O, ^{12}C, ^{14}N and Noble Gases on the Crystallisation of Amorphous Si Layers," *J. Appl. Phys.* **48**, 4241 (1977).

25) A.B. Danilin, A.A. Malinin, V.N. Mordkovich, V.V. Saraikin and O.I. Vyletalina, "Spatial Localisation of the Buried Ion-Beam Synthesized Layer of SiO_2 Inclusions in Si," *Nucl. Instrum. Meth.* **B82**, 431 (1993).

26) G. Brebec, R. Seguin, C. Sella, J. Bevenot and J.C. Martin, " Diffusion Du Silicium Dans la Silice Amorphe," *Acta. Metall.* **28**, 327 (1980).

27) S. Ellingboe, M.C. Ridgway and P.J. Schultz, "Buried SiO_2 Layer Formation in Si with an MeV O Ion Beam," *J. Appl. Phys.* **73**, 1133 (1993).

28) C. Jassaud, J. Margail, J. Stoemenos and M. Bruel, "High Temperature Annealing of SIMOX Layers: Physical Mechanisms of O Segregation," *Mater. Res. Symp. Proc.* **107**, 17 (1988).

29) C. Jassaud, J. Stoemenos, J. Margail, D. Dupuy, B. Blanchard and M. Bruel, "Microstructure of Si-implanted With High Dose Oxygen Ions," *Appl. Phys. Lett.* **46**, 1046 (1985).

30) A.H. van Ommen, "Low Dislocation SOI by Oxygen Implantation," *Mater. Res. Soc. Symp. Proc.* **107**, 43 (1988).

31) A. Mogro-Campero, N. Lewis. and S.A. Al-Marayati, "Macroscopic Defects in Epitaxial Si on SIMOX and in Annealed SIMOX," *Mater. Res. Soc. Symp. Proc.* **107**, 123 (1988).

32) K. Izumi, Y. Omura and T. Sakai, "SIMOX Technology and Its Application to CMOS LSIs," *J. Elec. Mater.* **12**, 845 (1983).

33) J-P. Colinge, K. Hashimoto, T. Kamins, S.Y. Chiang, E-D. Liu, S. Peng and P. Rissman, "High-Speed, Low-Power, Implanted-Buried-Oxide CMOS Circuits," *IEEE Electron. Dev. Lett.* **EDL-7**, 279 (1986).

34) A. Yoshino, *Proc. of Symp. on Silicon-on-Insulator Tech. and Dev.*, **13** (1992) 321.

35) M.K. El-Ghor, S.J. Pennycook, F. Namavar and N.H. Karam, "Formation of Low Dislocation Density Si-on-Insulator by a Single Implantation and Annealing," *Appl. Phys. Lett.* **57**, 156 (1990).

36) M.K. El-Ghor, S.J. Pennycook, T.P. Sjoreen, C.W. White and J. Narayan, "Cavity Formation in SIMOX Structures," *Mater. Res. Soc. Symp. Proc.* **107**, 79 (1988).

37) S. Visitergtrakul, C.O. Jung, S.J. Krause and B.F. Cordts, "Structure and Defect Development During Implantation of SIMOX Material," *Proc. of Symp. on Silicon-on-Insulator Tech. and Dev.*, 106 (1990).

38) F. Namavar, E. Cortesi, R.F. Pinizzotto and H. Yang, "Effect of O Implantation Conditions on Buried SiO_2 layer Formation Using a Multiple Step Process," *Mater. Res. Soc. Symp. Proc.* **157**, 179 (1990).

39) D. Venables, K.S. Jones and F. Namavar, "Low Dislocation Density Si-on-Insulator Material Produced by Sequential Oxygen Implantation and Low-Temperature Annealing," *Appl. Phys. Lett.* **60**, 3147 (1992).

40) D. Venables, K.S. Jones, F. Namavar and J.M. Manke, "Strain Relief and Defect Formation in High Dose Oxygen Implanted Si," *Mater. Res. Soc. Symp. Proc.* **235**, 103 (1992).

41) O.W. Holland, D.S. Zhou and D.K. Thomas, "Damage Accumulation During High-Dose, O^+ Implantation in Si," *Appl. Phys. Lett.* **63**, 896 (1993).

42) Y. Homma, M. Oshima and T. Hayashi, "An Investigation of the Properties of an Epitaxial Si Layer on a Substrate with a Buried SiO_2 Layer Formed by Oxygen-Ion Implantation," *Jpn. J. Appl. Phys.* **21**, 890 (1982).

43) F. Namavar, E. Cortesi and P. Sioshansi, "Low-Defect, High-Quality SIMOX Produced by Multiple O Implantation with Substoichiometric Total Dose," *Mater. Res. Soc. Symp. Proc.* **128**, 623 (1989).

44) Y. Ishikawa and N. Shibata, "Preparation of Thin Si-on-Insulator Films by Low-Energy Oxygen Ion Implantation," *Jpn. J. Appl. Phys.* **30**, 2427 (1991).

45) F. Namavar, E. Cortesi, B. Buchanan, J.M. Manke and N.M. Kalkhoran, "Ultrathin SOI Structures by Low Energy Oxygen Implantation," *Mater. Res. Soc. Symp. Proc.* **235**, 109 (1992).

46) A. Nejim, Y. Li, C.D. Marsh, P.L.F. Hemment, R.J. Chater, J.A. Kilner and G.R. Booker, "Direct Formation of Device Worthy Thin Film SIMOX Structures by Low Energy O-Implantation," *Nucl. Instrum. Meth.* **B80/81**, 822 (1993).

47) A. Nakashima and K. Izumi, "Surface Morphology of O-implanted Wafers," *J. Mater. Res.* **5**, 1918 (1990).

48) J. Rosenblatt, Particle Acceleration (Methuen & Co. Ltd., London, 1968) 34.

49) D. Venables, PhD. Thesis, University of Florida, 1992.

50) A.E. White, K.T. Short, J.L. Batstone, D.C. Jacobson, J.M. Poate and K.W. West, "Mechanisms of Buried Oxide Formation by Ion Implantation," *Appl. Phys. Lett.* **50**, 19 (1987).

51) F.W. Smith and G. Ghidini, "Reaction of Oxygen with Si(111) and (100): Critical Conditions for the Growth of SiO_2," *J. Electrochem. Soc.* **129** (1982) 1300.

52) P.B. Hirsch, A. Howie, R.B. Nicholson, D.W. Pashley and M.J. Whelan, Electron Microscopy of Thin Crystals (Krieger Publishing Co., London, 1965).

53) C.R. Wie, "High Resolution X-Ray Diffraction Characterization of Semiconductor Structures," *Mater. Sci. and Eng.* **R13**, 13 (1994).

54) X-Ray diffraction short course by Bede, Munich, 1991.

55) B.K. Tanner and D.K. Bowen, "Advanced X-Ray Scattering Techniques for the Characterization of Semiconductor Materials," *J. Cryst. Growth* **126**, 1 (1993).

56) Y.H. Lee, N.N. Gerasimenko and J.W. Corbett, "EPR Study of Neutron-Irradiated Silicon: A Positive Charge State of the <100> Split Di-Interstitial," *Phys. Rev. B* **14**, 4506 (1976).

57) A. Pesek, P. Kastler, K. Lischka and L. Palmetshofer, "Distribution of Strain in Ge Ion Implanted Silicon Measured by High Resolution X-Ray Diffraction," *Nucl. Instrum. Meth.* **B80/81**, 569 (1983).

58) J.G.E. Klappe and P.F. Fewster, "Fitting of Rocking Curves from Ion-Implanted Semiconductors," *J. Appl. Cryst.* **27**, 103 (1994).

59) M. Servidori, "Characterization of Lattice Damage in Ion Implanted Silicon by Multiple Crystal X-Ray Diffraction," *Nucl. Instrum. Meth.* **B19/20**, 443 (1987).

60) O.W. Holland and C.W. White, "Ion-Induced Damage and Amorphization in Si," *Nucl. Instrum. Meth.* **B59/60**, 353 (1991).

61) R. Fabbri, F. Cembali, M. Servidori and A. Zani, "Analysis of Thin-Film Solid Solutions on Single-Crystal Silicon by Simulation of X-Ray Rocking Curves: B-Si and Ge-Si binary Alloys," *J. Appl Phys.* **74**, 2359 (1993).

62) B.E. MacNeal and V.S. Speriosu, "Modeling Strain Distributions in Ion-Implanted Magnetic Bubble Materials," *J. Appl. Phys.* **52**, 3935 (1981).

63) B.M. Paine, N.N. Hurvitz and V.S. Speriosu, "Strain in GaAs by Low-Dose Ion Implantation," *J. Appl. Phys.* **61**, 1335 (1987).

64) B.M. Paine and V.S. Speriosu, "Non-Linear Strain Effects in Ion-Implanted GaAs," *J. Appl. Phys.* **62**, 1704 (1987).

65) L. Hart and J. Matsui, "X-Ray Characterization of Ion-Implanted and Rapid Thermal Annealed Silicon," *Semi. Sci. Tech.* **7**, 291 (1991).

66) M. Berti, G. Brusatin, A. Carnera, A. Gasparotto and R. Fabbri, "Channeling Effects in High Energy Ion Implantation: Si(N)," *Nucl. Instrum. Meth.* **B80/81**, 58 (1993).

67) G. Bai and M.-A. Nicolet, "Defect Production and Annealing in Self-Implanted Si," *J. Appl. Phys.* **70**, 649 (1991).

68) This thesis, Chapter 4.

69) D.S. Zhou, O.W. Holland and J.D. Budai, "Strain Relief Mechanism for Damage Growth During High-Dose O^+ Implantation of Si," *Appl. Phys. Lett.* **63**, 3580 (1993).

70) Available from Bede Scientific Instruments Ltd., Lensey Park, Bowburn, Durham, DH65PF, UK.

71) S. Takagi, "Dynamical Theory of Diffraction Applicable to Crystals with any Kind of Small Distortion," *Acta. Cryst.*, **15** (1962) 1311.

72) D. Taupin, *Bull. Soc. Franc. Mineral. Crist.*, "The Dynamic Theory of the Diffraction of X-rays by Deformed Crystals," **87** (1964) 469.

73) J.F. Ziegler, J.P. Biersack and U. Littmark, The Stopping and Range of Ions in Solids (Pergamon, Oxford, 1985), Vol. I.

74) F. Cembali, M. Servidori, E. Gabilli and R. Lotti, "Effect of Diffuse Scattering in the Strain Profile Determination by Double Crystal X-Ray Diffraction," *Phys. Status Solidi (a)* **87**, 225 (1985).

75) P.J. Schultz, G.R. Massoumi and W.N. Lennard, "Positron and Electron Solid Interactions," *Nucl. Instrum. Meth.* **B90**, 567 (1994).

76) P. Hautojärvi, Ed., Positrons in Solids: Topics in Current Physics, No. 12 (Springer, Berlin, 1979).

77) B. Nielsen, O.W. Holland, T.C. Leung and K.G. Lynn, "Defects in MeV Si-implanted Si Probed with Positrons," *J. Appl. Phys.* **74**, 1636 (1993).

78) P.J. Simpson, M. Vos, I.V. Mitchell, C. Wu and P.J. Schultz, "Ion-Beam-Induced Damage in Silicon Studied Using Variable Energy Positrons, Rutherford Backscattering, and Infrared Absorption," *Phys. Rev. D* **44**, 12180 (1991).

79) P.J. Schultz and K.G. Lynn, "Interaction of Positron Beams with Surfaces, Thin Films, and Interfaces," *Rev. Mod. Phys.* **60**, 701 (1988).

80) O.W. Holland, L. Xie, B. Nielsen and D.S. Zhou, "Implantation of Si Under Extreme Conditions: the Effects of High Temperature and Dose on Damage Accumulation," *to be published in J. Electron. Mater.*

81) T.C. Leung, P. Asoka-Kumar, B. Nielsen and K.G. Lynn, "Study of SiO_2-Si and Metal-Oxide-Semiconductor Structures Using Positrons," *J. Appl. Phys.* **73**, 168 (1993).

82) C.W. Nieh, F. Xoing, C.C. Ahn, Z. Zhou, D.N. Jamieson, T. Vreeland Jr., B. Fultz and T.A. Tombrello, "Formation of Buried Oxide in MeV O-implanted Si," *Mater. Res. Soc. Symp. Proc.* **107**, 73 (1988).

83) A. Grob, J.J. Grob, P. Thevenin and P. Siffert, "A Dechanneling Investigation of MeV O-implanted Si," *Nucl. Instrum. Meth.* **B58**, 236 (1991).

84) J.J. Grob, A. Grob, P. Thevenin, P. Siffert, A. Golanski and C. d'Anterroches, "A Silicon-on-Insulator Structure Formed By Implantation of MeV O," *Mater. Sci. and Eng.* **B2**, 123 (1989).

85) K. Touhouche, Y. Tao and A. Yelon, "Formation of SIMOX Layers by MeV Implantation," *Can. J. Phys.* **69**, 307 (1991).

86) A.B. Danilin, "Ion-Beam Synthesis of New Phases in Si Interpreted as the Decay of a Supersaturated Solid Solution," *Mater. Sci. Eng.* **B12**, 17 (1992).

87) W.P. Maszara, "Oxygen Bubbles Along Individual Ion Tracks in O^+ Implanted Si," *J. Appl. Phys.* **64**, 123 (1988).

88) C.D. Marsh, A. Nejim, Y. Li, G.R. Booker, P.L.F. Hemment, R.J. Chater and J.A. Kilner, "Control of the Buried SiO_2 Layer Thickness and Si Defect Density in SIMOX Substrates - Structural Investigation and Process Optimisation," *Nucl. Instrum. Meth.* **B74**, 197 (1993).

89) G.C. Aers, in Positron Beams for Solids and Surfaces, ed. P.J. Schultz, G.R. Massoumi and P.J. Simpson (AIP Press, New York, 1990) 162.

90) J. Stomenos, C. Jassaud, M. Bruel and J. Margail, "New Conditions for Synthesizing SOI Structures by High Dose Oxygen Implantation," *J. Cryst. Growth* **73**, 546 (1985).

91) C. Jassaud, J. Margail, J. Stoemenos and M. Bruel, "High Temperature Annealing of SIMOX Layers: Physical Mechanisms of Oxygen Segregation," *Mater. Res. Soc. Symp. Proc.* **107**, 17 (1988).

92) S. Cristoloveanu, J.H. Lee, J. Pumfrey, J.R. Davis, R.P. Arrowsmith and P.L.F. Hemment, "Profiling of Inhomogeneous Carrier Transport Properties with the Influence of Temperature in Silicon-on-Insulator Films Formed by O Implantation," *J. Appl. Phys.* **60**, 3199 (1986).

93) S. Cristoloveanu, "A Review of the Electrical Properties of SIMOX Substrates and Their Impact on Device Performance," *J. Electrochem. Soc.* **138**, 3131 (1991).

94) S. Cristoloveanu, S. Gardner, C. Jassaud, J. Margail, A.J. Auberton-Herve and M. Bruel, "Silicon-on-Insulator Material Formed by O Implantation and High-Temperature Annealing: Carrier Transport, Oxygen Activity and Interface Properties," *J. Appl. Phys.* **62**, 2793 (1987).

95) S.M. Hu, "Oxygen Precipitation in Silicon," *Mater. Res. Soc. Symp. Proc.* **59**, 249 (1985).

96) S. Maillet, R. Stuck. J.J. Grob, A. Golanski, R. Pantel and A. Perio, "High Temperature O-Implantation in Si: SOI Structure Formation Characteristics," *Nucl. Instrum. Meth.* **B19/20**, 294 (1987).

97) C.L. Olson and J.A. Roth, "Kinetics of Solid Phase Crystallisation in Amorphous Silicon," *Mater. Sci. Rep.* **3**, 1 (1988).

98) H. Alexander and H. Teichler, in Materials Science and Technology, eds. R.W. Cahn, P. Haasen and E.J. Kramer (VCH, New York, 1991) 249.

99) R. Goldberg, PhD. thesis, Melbourne University, 1995.

100) T. Lohner, M.A. El-Sherbiny, N.Q. Khánh, M. Fried, H. Wormeester and J. Gyulai, "Anomalous surface damage production during high energy implantation analyzed by ellipsometry and RBS," in press (1995) Proceedings of IBMM.

101) M.K. El-Ghor, S.J. Pennycook, T.P. Sjoreen and J. Narayan, "Characterization and Evolution of Microstructures Formed by High-Dose Oxygen Implantation of Silicon," *Mater. Res. Soc. Symp. Proc.* **74**, 591 (1987).

102) J. Wong-Leung, E. Nygren, J.S. Williams, *Appl. Phys. Lett.* **67**, 17 (1995).

103) D. Venables and K.S. Jones, "Defect Formation in High-Dose O-implanted Si," *Nucl. Instrum. Meth.* **B74**, 65 (1993).

104) A. Mazzone, "Defect Distribution in Ion-Implanted Si," *Phys. Stat Sol. (a)* **95**, 149 (1986).

105) J.R. Patel and A.R. Chaudhuri, "Macroscopic Plastic Properties of Dislocation-Free Germanium and Other Semiconductor Crystals. I. Yield Behavior," *J. Appl. Phys.* **34**, 2788 (1963).

106) J. Castaing, P. Veyssière, L.P. Kubin and J. Rabier, "The Plastic Deformation of Silicon Between 300°C and 600°C," *Phil. Mag.* **44A**, 1407 (1981).

107) D. Hull and D.J. Bacon, Introduction to Dislocations, (Pergamon Press, Oxford, 1984).

108) B.C. Larson, C.W. White and B.R. Appleton, "Unidirectional Contraction in Boron-Implanted Laser-Annealed Silicon," *Appl. Phys. Lett.* **32**, 801 (1978).

109) C.J. Tsai, A. Dommann, M.A. Nicolet and T. Vreeland, Jr., "Self-Consistent Determination of the Perpendicular Strain Profile of Implanted Si by Analysis of X-Ray Rocking Curves," *J. Appl. Phys.* **69**, 2076 (1991).

110) Omri, 1981 Thesis, INPL, Nancy.

111) W.X. Lu, Y.H. Qian, R.H. Tian, Z.L. Wang, R.J. Schreutelkamp, J.R. Liefting, and F.W. Saris, "Reduction of Secondary Defects Formation in MeV B^+ Ion-Implanted Si (100)," *Appl. Phys. Lett.*, **55**, 1838 (1989).

112) Zhong-lie Wang, Bo-xu Zhang, Qing-tai Zhao, Qi Li, L.R. Liefting, R.J. Schreutelkamp, and F.W. Saris, "Reduction of Secondary Defects in MeV Ion-Implanted Silicon by Means of Ion Beam Defect Engineering," *J. Appl. Phys.*, **71**, 3780 (1992).

113) O.W. Holland, D.K. Thomas, D.S. Zhou, "Technique to Suppress Dislocation Formation During High-Dose Oxygen Implantation of Si," *Appl. Phys. Lett.* **66**, 1892 (1995).

114) W.-K. Chu, J.W. Mayer and M.-A. Nicolet, Backscattering Spectrometry (Academic Press, New York, 1978).

115) J. Linnros, R.G. Elliman, W.L. Brown, "Divacancy Control of the Balance Between Ion-Beam-Induced-Epitaxial Crystallization and Amorphization in Silicon," *J. Mater. Res.* **3**, 1208 (1988).

116) J. Stoemenos, J. Margail, M. Dupuy, and C. Jassaud, "Self-Interstitial Migration in Si Implanted With O," *Physica Scripta* **35**, 42 (1987).

117) R.G. Elliman, J.S. Williams, W. L. Brown, A. Leiberich, D. M. Maher and R.V. Knoell, "Ion-Beam Induced Crystallization and Amorphization of Silicon," *Nucl. Instrum. Meth.* **B19/20**, 435 (1987).

118) F. Priolo and E. Rimini, "Ion-Beam-Induced Epitaxial Crystallisation and Amorphisation in Silicon," *Mater. Sci. Rep.* **5**, 319 (1990).

Addendum:

1. The aid the reader, the following is a list of acronyms and abbreviations used in this thesis:

ACAR	Angular correlation of the annihilation radiation technique
ANU	Australian National University
CMOS	Complementary metal-oxide semiconductor
DCXRD	Double crystal x-ray diffraction
ELO	Epitaxial lateral overgrowth
FIPOS	Full isolation by porous oxidised Si
IBA	Ion beam annealing
LSPE	Lateral solid phase epitaxy
MCA	Multi-channel analyser
PECVD	Plasma enhanced chemical vapour deposition
polySi	Polysilicon
RADS	Rocking curve analysis by dynamical simulation
RBS	Rutherford backscattering
RBS/C	Rutherford backscattering in combination with channeling
RC	Double crystal x-ray diffraction rocking curve
RNG	Random nucleation and growth
SIMOX	Separation by implantation of oxygen
SNICS	Source of negative ions by cesium sputtering
SOG	Spin-on-glass
SOI	Silicon on insulator
SOS	Silicon on sapphire
SPE	Solid phase epitaxy
SRAM	Static random access memory
TEM	Transmission electron microscopy
VEP	Variable energy positron annihilation spectroscopy
XTEM	Cross-sectional transmission electron microscopy
ZMR	Zone melt recrystallisation

e-beam	electron beam
O_I	interstitial oxygen atom
R_p	ion projected range
S parameter	characterisation of the positron annihilation lineshape sharpness
S_I	interstitial silicon atom
T	temperature
T_R	reversal temperature
V	vacancy
W parameter	characterisation of the positron annihilation lineshape width

χ_{MIN}	Minimum channeling yield
$\dot{\varepsilon}$	strain rate
Φ_c	critical dose for dislocation formation
Φ	implantation dose

2. There are two separate descriptions of the morphology of O-implanted Si resulting from high temperature implantation. These descriptions differ because they are of samples implanted at two different energies; 200 keV and 1 MeV. On p. 13, line 7, the description of morphology corresponds to O-implanted Si performed at an implant temperature and energy of $\geq$500°C and 200 keV, respectively, as reported by A.E. White[1]. On p. 49, line 30, the description of morphology corresponds to O-implanted Si performed at an implant temperature and energy of 450°C and 1 MeV, respectively.

1) A.E. White, *Mater. Res. Soc. Symp. Proc.*, **74** (1987) 585.

3. On p. 17, the point is made that "the additional Si overlayer thickness is not compatible with the requirements for fully-depleted circuits." The advantages of fully-depleted devices include a reduction of floating body effects, an improved subthreshold slope and better punch-through behaviour. A more complete explanation of the importance of fully and partially depleted devices can be found in the following references:

1) R.S. Muller and T.I. Kamins, Device Electronics for Integrated Circuits (John Wiley & Sons, New York, 1977).
2) R. Sundaresan and C.-E. D. Chen, "SIMOX Devices and Circuits," *Proc. of Symp. on Silicon-on-Insulator Tech. and Dev.*, **13** (1992) 437.

4. In section 1.3.5, it is stated that the advantages of low-dose, low-energy SIMOX fabrication "include lower implant times (reduced fabrication costs), high quality Si device layers (the lower dose yields less damage during implantation), and an abrupt Si/SiO_2 interface due to the decreased straggling of the implanted ions." The abrupt interface is the direct result of the decreased energy of the implanted ions or equivalently, a decreased number of implanted ion-substrate atom interactions. As explained in more detail in this thesis, section 1.2.4 (p.14), the coalescence of the buried SiO_2 layer during high temperature annealing occurs by the diffusion of O atoms towards regions of higher O concentrations. Also, excess Si interstitials diffuse away from such regions. The decreased straggle inherent to low-energy implantation means the O atoms and excess Si have less distance over which such diffusion occurs and consequently, the Si/SiO_2 interface is more abrupt after high temperature annealing.

5. The results presented in section 5.2 for O-implanted material fabricated with an implant temperature of 150°C showed the beneficial effects of a secondary Si implant for defect reduction. Such studies were also performed with O-implanted material fabricated at a higher implant temperature of 300 and 450°C. However, the secondary Si implant was shown to have little affect on the material formed at higher implant temperatures. The effect of the secondary Si beam on the electrical integrity or the microstructure of the buried oxide layer was not investigated.

Corrections:

1. On p. 13, the last sentence should be changed to: "Due to the extremely low diffusivity of Si in SiO_2 ($\sim 10^{-20}$ cm^2/sec at 1000°C)[26] it is likely that these SiO_2 precipitates impede the flow of Si interstitials to the Si surface. The accommodation of trapped Si interstitials within the Si overlayer would result in an increased defect concentration as has been experimentally observed by El-Ghor[1].

1) M.K. El-Ghor, S.J. Pennycook, F. Namavar, N.H. Karam, *Appl Phys. Lett.*, **57** (1990) 156.

2. On p. 31, para.2, Figure 2.6 should read Figure 2.5.

3. On p. 49, line 9, the sentence: "Tracks" of damage with an orientation corresponding to the angle of ion implantation are evident within the crystalline region." should be replaced with: "The crystalline region at 0.2-0.45 μm exhibits damage with a obvious structure to it.".

4. To clarify the information presented in section 1.2.4, the following is a rework of this section:

1.2.4 High-Temperature Annealing

Post-implantation annealing is essential to form low-defect-density, device-grade SIMOX material. Figure 1.10 shows the evolution of the defect microstructure of SIMOX material with increasing anneal temperature and time. High anneal temperatures are required to induce O segregation from depths with an O concentration

below 67 atomic % and to dissolve SiO_2 precipitates which have formed at such depths. A critical precipitate radius (r_c), below which SiO_2 precipitates will dissolve, can be defined as:

$$r_C = \frac{2\sigma}{\Delta H_V}\frac{T_E}{(T_E - T)} \qquad (1.3)$$

there ΔH_v is the enthalpy of formation of the SiO_2 phase per unit volume, σ is the Si/SiO_2 interfacial energy, T is the anneal temperature and T_E is the equilibrium temperature. The equilibrium temperature is the temperature at which the implanted O concentration *would be* in equilibrium with the surrounding lattice. Because ion implantation is a non-equilibrium process, the O concentration is typically in supersaturation with the surrounding lattice and hence, $T_E > T$. The critical radius depends on both T and (T_E-T), the latter of which is an expression of the interstitial O supersaturation. If $r < r_c$, the precipitate is unstable and dissolves. If $r > r_c$, the precipitate is stable and grows. At high temperatures the critical radius approaches infinity and a buried oxide layer (essentially a precipitate of infinite radius) is the only stable precipitate.

The growth and dissolution of SiO_2 precipitates is the result of Ostwald ripening. During high temperature annealing the surface energy of the precipitate becomes the dominant energy term. Consequently, the number of precipitates decreases since smaller precipitates are dissolved in favour of the larger ones. This process requires the diffusion of solute from regions with smaller SiO_2 precipitates to regions with larger SiO_2 precipitates. In other words, high temperature annealing promotes the diffusion of O towards the buried SiO_2 layer.

While high-temperature annealing is essential to produce device-grade SIMOX material, defects which have formed within the Si overlayer before post-implantation annealing, such as threading dislocations and stacking faults, can not be totally eliminated by such annealing.

5. On pg. 49 and in Figure 3.5, results are presented of O-implanted Si with a 450°C implant temperature. The claim is made that the material near the O end-of-range is amorphous. Electron beam diffraction was utilised to make this determination. However, detailed experimentation to distinguish between amorphous SiO_2 and vitreous oxide was not performed. High resolution electron microscopy in combination with electron diffraction would be necessary to better distinguish the SiO_2 phase.